Capacity Design Optimization of Steel Building Frameworks Using Nonlinear Time-History Analysis

by

Yusong Xue

A thesis
presented to the University of Waterloo
in fulfillment of the
thesis requirement for the degree of
Doctor of Philosophy
in
Civil Engineering

Waterloo, Ontario, Canada, 2012

AUTHOR'S DECLARATION

I hereby declare that I am the sole author of this thesis. This is a true copy of the thesis, including any required final revisions, as accepted by my examiners.

I understand that my thesis may be made electronically available to the public.

Abstract

This study proposes a seismic design optimization method for steel building frameworks following the capacity design principle. Currently, when a structural design employs an elastic analysis to evaluate structural demands, the analysis results can be used only for the design of fuse members, and the inelastic demands on non-fuse members have to be obtained by hand calculations. Also, the elastic-analysis-based design method is unable to warrant a fully valid seismic design since the evaluation tool cannot always capture the true inelastic behaviour of a structure. The proposed method is to overcome these shortcomings by adopting the most sophisticated nonlinear dynamic procedure, i.e., Nonlinear Time- (or Response-) History Analysis as the evaluation tool for seismic demands.

The proposed optimal design formulation includes three objectives: the minimum weight or cost of the seismic force resisting system, the minimum seismic input energy or potential earthquake damage and the maximum hysteretic energy ratio of fuse members. The explicit design constraints include the plastic rotation limits on individual frame members and the inter-story drift limits on the overall performance of the structure. Strength designs of each member are treated as implicit constraints through considering both geometric and material nonlinearities of the structure in the nonlinear dynamic analysis procedure. A multi-objective Genetic Algorithm is employed to search for the Pareto-optimal solutions.

The study provides design examples for moment resisting frames and eccentrically braced frames. In the examples some numerical strategies, such as integrating load and resistance factors in analysis, grouping design variables of a link and the beams outside the link, rounding-off the objective function values, are introduced. The design examples confirm that the proposed optimization formulation is able to conduct automated capacity design of steel frames. In particular, the third objective, to maximize the hysteretic energy ratio of fuse members, drives the optimization algorithm to search for design solutions with favorable plastic mechanisms, which is the essence of the capacity design principle.

For the proposed inelastic-analysis-based design method, the seismic performance factors (i.e., ductility- and overstrength-related force reduction factors) are no longer needed. Furthermore,

problem-dependent capacity design requirements, such as strong-column-weak-beam for moment resisting frames, are not included in the design formulation. Thus, the proposed design method is general and applicable to various types of building frames.

Acknowledgements

I would like to express my most sincere appreciation to my research supervisors, Professor Yanglin Gong and Professor Lei Xu, for their valuable guidance, support and engagement in completing this research.

Special thanks are also due to late Professor Donald E. Grierson who taught me structural optimization theory and contributed his constructive criticism and praise during my graduate program.

I greatly appreciate the other members of the examining committee Professor Elizabeth Weckman, Professor Mahesh Pandey and Professor Wei-Chau Xie. Special thanks to Professor Christopher M. Foley for serving as the external examiner.

The assistance of Professor Finley A. Charney, Professor Pierre Leger, and Professor Andre Filiatrault is gratefully appreciated.

I would like to acknowledge the financial support through postgraduate scholarships provided by the Natural Sciences and Engineering Research Council of Canada, the University of Waterloo Graduate Scholarships, QEII-Graduate Scholarship in Science and Technology, and the Teaching Assistantships granted by the Department of Civil and Environmental Engineering.

Finally, I dedicate this thesis to my wife Jiaoying and daughter Diana for their tremendous patience, encouragement and love. I am also very grateful to our parents for their love and support.

Dedication

To my family

Table of Contents

List of Figures

List of Tables

List of Notations

α_i	load factors
β_j , $\hat{\beta}$	hysteretic energy dissipation ratio of fuse members and mean value, respectively
β and γ	parameters of the Newmark method
γ	plastic rotation of link
δ	generalized deformation
δ_0	allowable value for inter-story drift
$\hat{\delta}_s$	mean value of the s^{th} inter-story drift
ζ	damping ratio
$\hat{\theta}_l$	mean value of plastic deformation demand for the l^{th} fuse member
$\theta_{l,0}$	allowable plastic deformation limit for the l^{th} fuse member
θ_p	plastic inter-story drift ratio
θ_y	yield rotation of steel frame member
μ	ductility factor
ρ	mass density of material
Φ	resistance factor
$\hat{\varphi}_m$	mean value of plastic deformation of the m^{th} non-fuse member
$\varphi_{m,0}$	allowable plastic deformation limit of the m^{th} non-fuse member
$\Delta\varphi_{t,k}$	increment of end rotation of the k^{th} structural element from time (t-Δt) to time t

ω_p and ω_q	the p^{th} and q^{th} natural frequencies, respectively
ξ_m and ω_m	location and associated weight of integration points of Gauss numerical method
A_k	cross-sectional area of member k
a_m	mass-proportional damping constant
$\boldsymbol{a}(x)$	force interpolation matrix
$\boldsymbol{a}$ and $\boldsymbol{a}_g$	displacement-deformation compatibility matrix
$\boldsymbol{a}_r$ and $\boldsymbol{b}_r$	rotation transformation matrix
b_t, b_i and b_c	stiffness-proportional damping constants
$\boldsymbol{b}$ and $\boldsymbol{b}_e$	equilibrium transformation matrix
$\boldsymbol{b}_u$, $\boldsymbol{b}_s$, $\boldsymbol{b}_{p\Delta}$	equilibrium transformation matrix using deformed frame element formation
$[C]$	global viscous damping matrix
$[C]_t$	tangent damping matrix
$\boldsymbol{C_j}$	a set of discrete steel cross-sections
$\boldsymbol{D}$	section deformation vector
d_b	beam depth
d_c	column depth
d_{ex}	distance between extreme Pareto-optimal solutions
d_i	crowding distance of Pareto-optimal solution i
E	Young's modulus of material

E_a	absorbed energy
E_d	damping energy
E_h	irrecoverable hysteretic energy
$E_{h,k}$	hysteretic energy dissipation of the k^{th} structural member
E_{h_fuse}	hysteretic energy of fuse members
E_i	relative seismic input energy
$E_{i,m}(t)$	seismic input energy of the m^{th} degree-of-freedom at time t
$\hat{E}_i$	mean value of seismic input energies for n_g ground motions
E_k	kinetic energy
E_s	elastic strain energy
e	link length
$F^i_{t,m}$	inertial force vector of the m^{th} degree-of-freedom at time t
$\{F_r(t)\}$	global nonlinear restoring force vector at time t
$\boldsymbol{F}$	element flexibility matrix
$\boldsymbol{F}_e$	elastic element flexibility matrix
$\boldsymbol{f}_s$	section flexibility matrix
f_1, f_2, f_3	normalized objective functions
f_y	yield force of seismic force resisting system
F_{yc}	yield strength of column steel

F_{ye}	expected steel yield stress
$g_l(\bullet)$	function of the l^{th} constraint
g_l^U	upper bound for the l^{th} constraint
I	moment of inertia of frame member
I_{pD}	moment of inertia of fictitious column
I_G	moment of inertia of one typical gravity column
$[K]_c$	the last converged stiffness matrix of the current iteration
$[K]_i$	initial elastic stiffness matrix
$[K]_T$	tangent stiffness matrix
$[K]_t$	tangent stiffness matrix of the current iteration
$\overline{\boldsymbol{k}_g}$	geometric transformation stiffness matrix
$\overline{\boldsymbol{k}_m}$	material transformation stiffness matrix
$\overline{\boldsymbol{k}_{p\Delta}}$	geometric stiffness matrix using p-Δ transformation matrix
$\boldsymbol{k}_s(x)$	section stiffness matrix
$\boldsymbol{k}_t^{el}$	tangent stiffness matrix of frame element under deformed equilibrium equations
$\boldsymbol{k}_t^{\boldsymbol{m}}$	tangent stiffness of frame element in the basic system
$\overline{\boldsymbol{k}_t}$	tangent stiffness matrix in local system
L	length of un-deformed frame element
L_k	length of the k^{th} member

L_n	length of deformed frame element
$[M]$	global mass matrix
M_{fc}	moment demand of columns
M_m	mass value of the m^{th} degree-of-freedom
M_{pb}	nominal plastic moment resistance of beams
M_{pc}	nominal plastic moment resistance of columns
M_{rc}	moment capacity of columns
$M_{t,k}$	internal bending moment of the k^{th} frame element at time t
N_p	number of integration points of Gauss numerical method
n_0	number of objectives
n_c	number of design constraints
n_e	number of structural members
n_f	number of fuse members
n_g	number of ground motions
n_m	number of degrees-of-freedom
n_{nf}	number of non-fuse members
n_{int}	number of interior Pareto-optimal solutions
n_s	number of stories
n_x	number of design variables

$\mathbf{OBJ}$	objective function vector
OBJ_1	weight objective function
OBJ_2	seismic input energy objective function
OBJ_3	hysteretic energy dissipation objective function
P, P_n	axial compressive force and the corresponding nominal strength, respectively
P_1, P_2, P_3	gravity loads of interior frames
$P_{t,k}$	internal axial force of the k^{th} structural element at time t
P_{ye}	expected axial yield force
$\overline{\boldsymbol{p}}$	force vector in local coordinate system
$\boldsymbol{p}$	force vector in global coordinate system
Q	generalized force
Q_1, Q_2, Q_3	gravity loads directly applied to the frame members of EBFs
R_o	overstrength-related modification factor
R_d	ductility-related modification factor
R_n	nominal resistance
R_y	factor to estimate the probable yield stress of steel material
$\{r\}$	support influence vector
r_m	moment ratio at a typical interior beam-to-column intersection
$\boldsymbol{S}$	section force vector

S_i	load effects
s_p	spread of Pareto-optimal solutions
$\{\ddot{u}(t)\}$	response vector of acceleration
$\{\dot{u}(t)\}$	response vector of velocity
$\{u(t)\}$	response vector of displacement
u_m	peak deformation of seismic force resisting system
u_y	yield deformation of seismic force resisting system
$\boldsymbol{u}$	displacement vector in global coordinate system
$\overline{\boldsymbol{u}}$	displacement vector in local coordinate system
$\Delta u_{t,m}$	displacement increments of the m^{th} degree-of-freedom at time t
$\Delta u_{t-\Delta t,m}$	displacement increments of the m^{th} degree-of-freedom at time $(t-\Delta t)$
$\Delta\overline{u}_x$, $\Delta\overline{u}_y$	increment displacements in local system
$\boldsymbol{\delta u}$	virtual displacement vector in global coordinate system
V_h	shear force acting at the beam plastic hinge location
$V_{t,k}$	internal shear force of the k^{th} structural element at time t
$\boldsymbol{V}$	element deformation vector
$\boldsymbol{v}$	basic deformation vector of frame element
$\boldsymbol{\delta v}$	virtual deformation vector of frame element
$\boldsymbol{W}$	element force vector

$W_{Moment,k}$	work done by the bending moment of the k^{th} member
$W_{Axial,k}$	work done by the axial force of the k^{th} member
$W_{Shear,k}$	work done by the shear force of the k^{th} member
$\boldsymbol{w}$	basic force vector of frame element
$\boldsymbol{X}$	vector of design variables
$\boldsymbol{X}_j$	vector of a specified set of discrete values for design variable x_j
x_j^l , x_j^u	lower and upper bounds for design variable x_j, respectively
x_j	the j^{th} design variable
$\ddot{x_g}(t)$, $\ddot{x}_{g,t}$	ground acceleration at time t
$\Delta x_{t,k}$	increment of axial deformation of the k^{th} element from time (t-Δt) to time t
$\Delta y_{t,k}$	increment of shear deformation of the k^{th} element from time (t-Δt) to time t
Z	plastic modulus
Z_b	plastic modulus of beam section
Z_c	plastic modulus of column section

Chapter 1
Introduction

In North America, ground motions with a probability of exceedance of 2% in 50 years have been chosen as the seismic hazard level for structural design. It is generally uneconomical (and often impractical) to design and construct building structures that will remain elastic during such a strong earthquake ground motion (NRCC 2006). In seismic design, a certain amount of damage is acceptable as long as the primary objectives, life safety and collapse prevention, are assured. Thus, a Seismic Force Resisting System (SFRS) is supposed to be able to tolerate deformations beyond its elastic limit without collapse during a strong earthquake.

Modern seismic provisions (AISC 2005a; CSA 2009) generally employ a force reduction factor to account for the ductility of steel frames. The advantage of using a reduced force is that it is suitable for use with an elastic structural analysis procedure for evaluating seismic demands. However, this elastic-analysis-based design procedure is unable to capture the true strength of the structure at its ultimate limit state. Since inelastic displacements cannot be obtained from an elastic analysis, as an approximation, seismic provisions usually allow prediction of inelastic displacements through multiplying elastic displacements by an amplification factor. However, the values of the force reduction and displacement amplification factors used by seismic provisions are often far from realistic.

Although the inelastic characteristic of structural performance can be often estimated by using a nonlinear static procedure, the changes in dynamic response and the higher mode effects cannot be accurately considered through a static analysis. To overcome the limitations of static analysis, the nonlinear dynamic procedure, called Nonlinear Time- (or Response-) History Analysis, should be employed. This procedure directly traces the seismic inelastic responses of a structure through a step-by-step numerical integration algorithm estimating the sequence of yielding and the corresponding distribution of inelastic deformation among members from the time history of a ground motion. The analysis procedure can explicitly account for the effects of structural member yielding, destabilizing effects of gravitational loads, and dynamic characteristics of the earthquake loading. The merits of a Nonlinear Time-History Analysis to investigate the realistic

structural performance, either within the elastic region or beyond the elastic limit, make such analysis appropriate for all building structures.

Based on lessons learned from past earthquakes, SFRSs are preferably designed to confine inelastic deformations to suitable and appropriately detailed regions in order to achieve desirable seismic response performance. Such design philosophy, the so-called Capacity Design Principle, has been widely adopted in modern seismic provisions (e.g., Clause 27 in CSA-S16-09 (CSA 2009)). Capacity Design coupled with an elastic analysis is the prevailing design method for current engineering practice.

However, the elastic-analysis-based capacity design approach has a major shortcoming: it is mainly implemented by hand calculations instead of by computers because the corresponding elastic analysis, which is conducted under a code specified lateral earthquake base shear, can only obtain design forces for fuse members. The design forces for non-fuse members need to be computed by considering the ultimate expected strength of the fuse members. This shortcoming can only be possibly overcome by employing an inelastic-analysis-based design method. Thus, an inelastic-analysis-based design tool specially developed for the capacity design of building frameworks is desirable. Such a design tool will help engineers eliminate arduous hand calculations and will be able to integrate an optimization technique into the design process to obtain efficient and economical design solutions.

The optimal solution for a specific seismic design task cannot generally be achieved through intuition and experience only. The traditional trial-and-error design method, if used with a nonlinear time-history analysis as the evaluation tool, would be extremely difficult to implement due to the daunting computational demands. An optimization method is needed to help structural engineers to evaluate alternatives and to achieve an optimum design.

Seismic design approaches based on inelastic dynamic analyses are greatly needed for the further development of modern seismic provisions. This is reflected by the adoption of nonlinear time-history analysis by ASCE/SEI 41-06 (ASCE 2007), NEHRP (FEMA 2004a) and NBCC (NRCC 2010) as an efficient tool to evaluate seismic demands for the rehabilitation of existing structures and for the design of new building structures. In this research, a unified capacity design

optimization methodology using a nonlinear time-history analysis is proposed to improve the estimation of structural seismic response under strong earthquakes, to facilitate the arduous computation work of Capacity Design, and to integrate an optimization technique into the design process to obtain an optimum design solution.

1.1 Current Practice of Seismic Design

As it is recommended in the National Building Code of Canada (NBCC) 2010, the primary objective of seismic design provisions is to provide an acceptable probability of attaining life safety performance under the design level earthquake ground motions. In accordance with the limit state design philosophy, a well-designed building structure is expected to have a very small probability of exceeding the corresponding limit states. In structural design practice, the satisfactory failure probability requirements are implicitly expressed everywhere from the defining of loads and material properties to the criteria of design calculation.

Seismic loading is deemed as a rare load in comparison with sustained or frequently occurring loads (such as dead and live loads), since earthquake actions last for a short time only. In the past editions of National Building Code of Canada, seismic hazard was defined at a 10% probability of exceedance in 50 years (return period of approximately 500 years). However, it has been discovered that designing structures under that level of ground motion did not provide a uniform probability against collapse (NRCC 2006; FEMA 2004b). In order to provide a uniform margin of failure for structures under earthquake loading, a level of earthquake ground motion with a 2% in 50 years probability of exceedance (return period of approximately 2500 years) has been chosen for seismic hazard values in NBCC 2005 and 2010.

For the 2% in 50 years Design Ground Motions (DGMs), the earthquake level is too high to design building structures to respond within elastic range of response. On the other hand, it has been accepted that lack of strength (in comparison with an equivalent elastic system) does not necessarily result in failure (Paulay and Priestly 1992; FEMA 2004b; NRCC 2006). A structure could actually survive an earthquake, if its inelastic structural deformations resulted from the lack of strength did not significantly further degrade the original structural strength.

Therefore, the paramount issue of conceptual seismic design is to separate the undesirable inelastic deformation modes with subsequent severe strength reduction from the desirable ductile limit states with little strength reduction, and to ensure the ductile structural response is achieved. Indeed, such seismic design philosophy has been explicitly included in governing codes, such as NBCC. However, it is customary in the structural design profession to use elastic-analysis-based methods to proportion structural members and to estimate structural deformation response. The current design methods usually employ a reduced lateral seismic base shear force to proportion a SFRS while the expected ductile response is enforced by the corresponding detailing requirements.

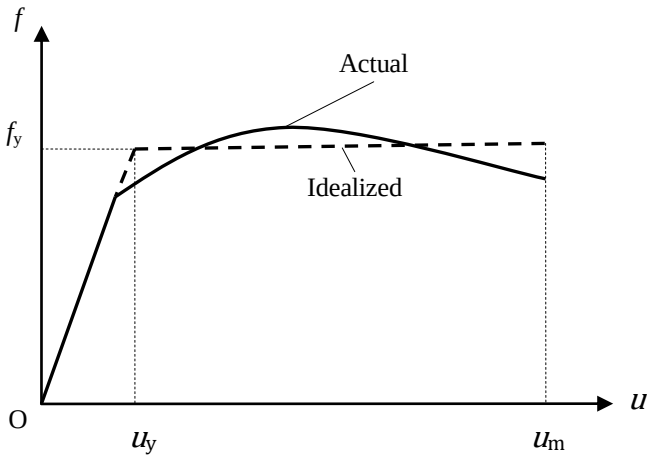

Figure 1-1 Force-deformation curve

The rationale to employ an elastic analysis method with a reduced base shear force to estimate inelastic seismic response can be derived from the investigation of the ductility property of a building structure. The ductility, which represents the essential attribute of sustaining inelastic deformations without significant loss of strength, has been quantitatively defined to explore the structural seismic performance. For systems deforming into the inelastic range, as shown by the force-deformation curve in Figure 1-1, the ratio of the peak deformation of the system, u_m, to the yield deformation of the system, u_y, is called ductility factor, μ.

$$\mu = \frac{u_m}{u_y} \qquad (1 - 1)$$

Theoretically, the earthquake loadings are earthquake-induced displacements acting on the building structures rather than the traditional loads. For an elastic linear system, the strength demands on the SFRS are proportional to the induced displacements. However, as shown in Figure 1-1, the strength demand on a ductile SFRS can be significantly reduced to a lower value neighbouring the yield strength of the system. In some sense, the ductility factor for a SFRS represents the capacity to reduce the strength demand on the corresponding elastic system as long as the total lateral displacement induced by earthquake ground motions is less than u_m. In other words, it is possible to proportion structural members for a ductility-related reduced force as long as ductility detailing requirements are satisfied. In comparison with the design method which only relies on strength and stiffness to resist the imaginary lateral seismic forces, the ductility-based design method provides an economical alternative to survive the large inelastic displacements induced by a severe earthquake ground motion.

1.1.1 Elastic-Analysis-Based Design Method

The essence of earthquake effects on building structures is the dynamic nature of earthquake loading. Structural responses (such as deformations and stresses) to an earthquake are dynamic phenomena that depend on the dynamic characteristics of the structures and the intensity, duration, and frequency contents of the ground motions. For this reason, elastic dynamic analysis has been strictly required by NBCC 2010 (except for the structures in low seismicity zones or regular structures with a medium-height).

In seismic design, the Modal Response Spectrum Analysis procedure has been widely adopted as the primary dynamic analysis tool to estimate the seismic demands of building structures. Practically, earthquake hazards or design seismic forces are represented as a function of the periods of various structural vibration modes with respect to a design response spectrum. Thus, seismic design can be conducted in the same manner as the analysis of the structure for static loads.

The response spectrum method provides a practical approach to apply the knowledge of structural dynamics to the development of lateral force requirements in building codes (Chopra 2007; Paz 1991). The elastic response obtained from a linear dynamic analysis is adjusted by

performance factors, such as ductility-related modification factor, R_d and overstrength-related factor R_o, to determine the design values.

Design Response Spectrum

In general, response spectra are prepared by calculating the responses of single-degree-of-freedom (SDOF) systems to a specified excitation with various amount of damping. The largest values of a response for all frequencies of interest are recorded and plotted. For a direct response spectrum analysis, the maximum displacement and/or acceleration responses are readily obtained from the plot with respect to the natural period and damping ratio of the system. Then, the strain and stress states are determined using the obtained spectral coordinates. Since no two earthquakes are alike, the consequent response spectra and the computed strain and stress states are different.

Different from the response spectrum for a specific earthquake ground motion, a Design Response Spectrum incorporates the spectra of several earthquakes and represents the probability characteristics of the ground motions. In practice, the base shear of a SFRS with a specific vibration mode and damping ratio is determined in proportion to its spectral acceleration with respect to the corresponding natural vibration period.

Modal Response Spectrum Method

In a Modal Response Spectrum Method, the maximum base shear of each participating vibration mode of a multi-degree-of-freedom (MDOF) system is determined from the Design Response Spectrum with respect to the corresponding natural period of the mode. Next, a force distribution consistent with each modal shape is employed to estimate the modal structural response. Then, to incorporate all the considered vibration modes of the SFRS, a specific combination rule is used to approximate the maximum values of seismic responses. For building framework design, the Square Root of the Sum of Squares of the modal contributions (SRSS method) is the most widely adopted combination rule (Note that the modal maximum values generally do not occur simultaneously).

Although the maximum structural response values can be obtained through a Modal Response Spectrum Analysis, the phases of response quantities with respect to the considered vibration modes are lost. Furthermore, tracing the sequence of yielding and the corresponding distribution of inelastic deformation among structural members cannot be provided in the response spectrum analysis. There is still a gap between the response spectrum analysis and the representation of the actual seismic demands. In order to fully capture the process of yielding formulation and to better understand the mechanism of nonlinear distribution within the building structure subjected to a severe earthquake ground motion, a rigorous seismic design methodology must employ Nonlinear Time-History Analysis to overcome the shortcomings of the response spectrum analysis.

Ductility-Related Force Modification Factor (R_d)

In seismic provisions, ductile seismic response is deemed as the desirable and functional performance of a SFRS. As shown in Figure 1-1, such a ductile response exhibits a high level of inelastic deformation capacity. From the viewpoint of energy, it can be seen that an energy dissipation mechanism for the seismic input energy can be functionally achieved by reducing the force term (i.e. the strength demand) and increasing the displacement term (i.e. the capacity of the inelastic deformation) simultaneously.

In NBCC 2010, the ductility-related force modification factor, R_d, is employed to determine the required full-yield strength of a SFRS, f_y in Figure 1-1 (i.e., the strength corresponding to the successive plastifications leading to a plastic mechanism).

The force modification factor, R_d, in the denominator of the formula employed for calculating the lateral earthquake force, represents the capability of the structure to dissipate seismic input energy through hysteretic inelastic response. Therefore, a structure which has the ability to undergo inelastic deformations is assigned a value of R_d greater than 1.0. The greater the ductility of a structure is, the higher the assigned value of R_d. The interrelationship between continuity, ductile detailing, and redundancy in a SFRS should be considered carefully to assure the undergoing of nonlinear behaviour without a significant loss in strength and stiffness.

Overstrength-Related Force Modification Factors (R_o)

It was noted that the full-yield strength of a SFRS are generally greater than the prescribed design seismic loading obtained from a design response spectrum. There are several sources which increase the actual yield strength of a SFRS. Among them, the material overstrength may be the first and the most evident one. Second, the limit state design method requires structures be designed such that their factored resistance is equal to or greater than the factored load effect. Specifically, designers may introduce additional overstrength by using larger sections than needed. As a result, many steel structures, particularly those possessing ductile behaviour, can provide a considerable reserve of strength, which is not explicitly accounted for in design. It has been reported (FEMA 2004b) that the strength corresponding to the first actual significant yielding of building structures may not occur until the applied load was 30 to 100 percent higher than the prescribed design seismic force. Therefore, it is reasonable to include the reserve strength in design provided it can be shown to exist (NRCC 2006).

In NBCC 2010, the overstrength-related force modification factor, R_o, in conjunction with the type of SFRS, has been employed to approximate the dependable overstrength that arises from the application of the design and detailing provisions. Same as the ductility-related force factors, the determination of overstrength-related force factor, R_o, is based on the comparative results of various SFRSs and engineering judgements (FEMA 2009). However, in order to account for the realistic structural overstrength, a direct inelastic-analysis-based method rather than the predefined SFRS-related factors is needed.

1.1.2 Capacity Design

In general, the earthquake impacts on building structures can be deemed as a large amount of seismic energy acting on building structures in the form of displacements resulted from base vibrations. The seismic energy is dissipated through the movements and deformations of the building structures. It has been found that the dynamic inelastic deformation responses could be effectively used to dissipate energy as long as the integrity of the system is assured (Housner 1956). Thus, structural seismic design has been encouraged to employ those inelastic deformations (corresponding to a stable energy dissipation mechanism) to functionally survive

strong earthquakes. In concept, a systematic design tool is required to ensure a reliable energy dissipation mechanism can be achieved under the Design Ground Motion. Such seismic design philosophy leads to the Capacity Design principle being widely adopted in seismic provisions.

Capacity Design principle is an approach to design a structure such that it will respond to a strong earthquake in the way required. Following Capacity Design, inelastic deformations are confined to specific regions or members (called fuse members) where such pre-located inelastic response can be developed without significant loss of strength during the cyclic seismic loading. In consequence, a large amount of seismic energy can be dissipated through the stable inelastic deformation response. Importantly, those inelastic action regions must be detailed to prevent premature undesirable failure modes, such as local buckling and member instability. For non-fuse members, it is required that they undergo only elastic response (or some non-detrimental plastic deformation) for the duration of the Design Ground Motions. Hence, non-fuse members have to be designed with respect to the possible maximum forces transmitted from fuse members rather than the forces corresponding to the prescribed seismic design forces. As a result, the likelihood of inelastic action or failure among non-fuse members can be effectively eliminated.

Clearly, the capacity design philosophy is deeply rooted in plastic analysis and design (Bruneau et al 1998). In theory, once a fully plastic state has been reached, no additional force can be imparted to either the fuse members or the whole structure, and as a result, non-fuse members are protected against the effects of additional loading. To achieve such performance in a SFRS, the ductile energy dissipating members or fuses must be clearly identified and detailed, and a proper strength hierarchy must be provided to constrain inelastic behaviour to these fuse members.

In practice, capacity design approach requires re-assessment of structural demands subject to the capacity of fuse members because the estimation of actual inelastic behaviours of fuse members and the corresponding force responses cannot be provided by using an elastic analysis. The accuracy of the assessment is dependent on a number of issues, including the acknowledgement of the statistical variability of material properties (i.e., the expected yielding and ultimate strengths), possible development of strain hardening in fuse members, and the characteristics and impacts of the dynamic-loading. Thus, the facilitation and reliability of Capacity Design in practice may be still questionable unless an inelastic analysis-based design method is employed.

1.2 Structural Optimization

Structural design is a process to design structural members to function as a whole structural system. Driven by the motivation to maximize output or profit with respect to the limited resources, the pursuit of the best design solutions becomes destined to prevail in the structural design profession. Through taking advantage of the significant progress which has been made in computer methods for analysis and design, structural designers are encouraged to employ optimization techniques to design the best system.

Literally, design optimization is concerned with achieving the best outcome of a given performance while satisfying certain restrictions. Mathematically, an optimization problem can be stated in the form of a set of objective functions subject to the constraints which are formulated in terms of design variables (Arora 2007). The constraints imposed on a design will affect the final design and force the objective functions to assume higher or lower values than they would take without the constraints. By employing an appropriate optimization algorithm with regard to the characteristics of a mathematical model, the optimization problem is solved to find the set of design variables corresponding to the best outcome of objective functions. In general, optimization algorithms are numerical search techniques which start from an initial trial and proceed in small steps to improve the values of the objective functions, or the degree of compliance with the constraints, or both. The optimum is achieved when no progress can be made in improving the objective functions without violating the constraints. For structural optimization problems, weight, displacements, stresses, vibration frequencies, buckling loads and cost or any combination of these can be used to construct the optimization objective functions or constraints (Burns 2002). In this way, structural optimization can be viewed as a conceptual framework for facilitation of the real-life structural design.

The development of the field of structural optimization may be traced back to the eighteenth century. Although the maxima and minima in an optimization problem can be obtained through ordinary Differential Calculus, Calculus of Variation, and method of Lagrange Multipliers, it has been shown that such classical optimization techniques have limited value for the solution of practical structural design problems except for very simple designs where the optimization problems can be formulated in functional forms and solved analytically (Grierson 2009; Haftka

1992). On the other side, most structural design problems are simulated and analyzed by using a discretized finite element model of the structure. The structural behaviours and/or response are solved numerically with respect to the discretized model. Therefore, a numerical optimization method has to be employed to solve majority of structural optimization problems. Among mathematical programming methods, Linear Programming (LP) and Sequential Linear Programming (SLP) have been known for many years as useful in structural optimization profession. Specifically, the exact global optimum can be reached in a finite number of steps when a structural optimization problem can be formulated in the form of a Linear Programming problem. However, very few real-life structural optimization problems can be posed directly as Linear Programming without involving a degree of appropriate simplification. Occasionally, if an optimization problem in structural analysis and design can be linearly approximated with reasonable simplification, then, the problem can be solved through the procedure of Sequential Linear Programming. However, Sequential Linear Programming strategy can encounter difficulties either with an infeasible initial 'trial' or without a proper choice of 'move limits'.

Sometimes it is computationally convenient to employ unconstrained optimization techniques to solve a constrained structural design problem if the problem can be transformed into an equivalent unconstrained optimization problem. The common techniques for solving unconstrained optimization problems can be classified into three distinct categories based on the strategy used to establish numerical search direction. Accordingly, Direct Search Methods, Gradient Methods and Newton Methods employ the values of objective function, the values of objective function and its first derivatives, and the values of objective function and its first and second derivatives, respectively, to reach the optimal design. For constrained optimization problems, the design space is divided into a feasible domain and an infeasible domain based on the violation states of the constraints. By using Lagrange multiplier method, the impact of constraints on the objective function is included to obtain Kuhn-Tucker conditions for extremizing the objective function. In practice, either the Gradient Projection Method (in which the improvement of objective function is following the constraint boundaries) or the Feasible Direction Method (in which the objective function is improved within the feasible domain) can be employed to solve constrained optimization problems.

Over the years, devotion to providing optimization techniques in the design of steel frameworks to achieve economical structures has gained wide acceptance in the academic community. Widely used optimization objectives include minimum cost, minimum compliance, a fully stressed state, desired component/system reliable levels, etc. Constraints can be placed on static and dynamic displacements and stresses, natural frequencies, energy dissipating capacity and member sizes. Approximation concepts based upon first-order Taylor series expansions, sensitivity analysis, virtual load techniques, constraint-deletion and design variable linking may be employed to convert structural design problems into a sequence of optimization problems, which are solved using generalized optimization methods.

Grierson (1984) developed a design method for the minimum weight design of planar frameworks under both service and ultimate loading conditions. Acceptable elastic stresses and displacements were ensured at the service-load level while, simultaneously, adequate safety against plastic collapse was ensured at the ultimate-load level. A computer-automated method for the optimum design of steel frameworks accounting for the behaviour of semi-rigid connections was developed by Xu and Grierson (1993). The method considered connection stiffness and member sizes as continuous-valued and discrete-valued design variables, respectively. A continuous-discrete optimization algorithm was applied to minimize the 'cost' of connections and members of the structure subject to the constraints on stresses and displacements under specified design loads. Chan, Grierson and Sherbourne (1995) presented an automatic resizing technique for the optimal design of tall steel building frameworks. The computer-based method was developed for the minimum weight design of lateral-load-resisting steel frameworks subject to inter-story drift constraints and member strength and sizing constraints in accordance with building code and fabrication requirements. The design optimization problem was solved by an optimality criteria algorithm.

A dual approach for the optimal elastic-plastic design of large-scaled skeletal structures using sensitivity analysis was presented by Mihara et al (1988). The main feature of the method was that the sensitivity coefficients of the elasto-plastic deformation found analytically were employed to efficiently perform the design calculation for large-scaled structures. Saka and Hayalioglu (1990) formulated a structural optimization algorithm for geometrical nonlinear

elasto-plastic frames. The algorithm coupled optimality criteria approach with a large deformation analysis method for elasto-plastic frames. The optimality criteria method was used to develop a recursive relationship for design variables. It was shown that the consideration of geometric and material nonlinearities in the optimum design not only led to a more realistic approach but also lighter frames.

Although excellent approximation concepts have been developed for a wide variety of structural optimization problems, the quality of such approximation depends very much on the nature of the design variables. A common disadvantage of most gradient-based numerical methods is their inability to distinguish local and global minima. Evolution strategies (or genetic-based search algorithm) are very robust and are capable of being applied to an extremely wide range of problem domains where traditional optimization algorithms are not. More recently, Simulated Annealing and Genetic Algorithms (GA) have emerged as tools suited for solution of optimization problems where a global minimum is sought or the design variables are required to take discrete values.

A preliminary conceptual design model which coupled a genetic algorithm with a neural network to generate best-concept design solutions was suggested by Grierson (1996). Park and Grierson (1999) further presented a computational procedure for multi-criteria optimal conceptual design of structural layout of buildings. Two objective criteria, minimization of building cost and the flexibility of floor space usage, were considered for evaluating alternative designs. A multi-criteria genetic algorithm was applied to solve the bi-objective conceptual building layout design problem using Pareto optimization theory.

The minimization problem solved by evolutionary structural optimization (ESO) was examined by Tanskanen (2002). It was noted that the sequential-linear-programming-based approximate optimization method followed by the Simplex Algorithm was equivalent to ESO if a strain energy rejection criterion is utilized. It was concluded that ESO is not just an intuitive method (as it has a very distinct theoretical basis) but also it is very simple to employ in engineering design problems. For this reason, ESO has great potential in developing design tools. Foley (2003) proposed an object-oriented Evolutionary Algorithm (EA) for the automated design of partially restrained and fully restrained steel frames. The design problem was developed using an

objective function which included frame member weight and connection cost/complexity. Constraints related to both service and strength load levels were included. It was suggested that the EA could be a useful methodology upon which to pursue the development of automated performance-based design algorithms.

1.3 Seismic Design Optimization

The seismic design philosophy for building frameworks is usually associated with multi-tiered performance criteria. As published by the Structural Engineers Association of California in its blue book (SEAOC 1975), a properly designed structure should provide the following multi-tiered performance capabilities:

1. Resist minor earthquake shaking without damage
2. Resist moderate earthquake shaking without structural damage but possibly with some damage to non-structural features
3. Resist major levels of earthquake shaking with both structural and non-structural damage, but without endangerment of the lives of occupants

In the past three decades, increased computational power makes accurate analysis techniques (e.g., time-history analysis, nonlinear static analysis, and nonlinear dynamic analysis) available throughout the profession. The significant progress in the development of structural optimization techniques provides robust solution methods to achieve the optimal seismic structural designs for a variety of loading and structure types (Foley 2002).

Balling et al (1983) presented a design method to directly quantify the accepted seismic-resistant philosophy. It might be the first attempt to include dynamic nonlinear analysis within a design process. In their paper, the design procedure was cast into a mathematical programming problem with separated objective functions, including the minimization of structural volume as well as the minimization of response quantities (such as story drifts and inelastically dissipated energy). Quantified structural damage along with serviceability constraints under gravity loads only are imposed on structural behaviour. The feasible direction optimization algorithm was employed to ensure the successive design iterations remain feasible for the separated single-objective optimization problems. It was recognized that further improvement in structural modelling was

needed to achieve a reliable design. Only one single ground motion record was involved during development of the proposed design methodology.

Another early effort (Austin et al 1986, 1987) on seismic optimization was given to the multi-tiered performance criteria and the related acceptable risk. Austin et al suggested a methodology for the optimal probabilistic limit state design of seismic-resistant steel frames. A variety of statistical structural responses under earthquake ground motions as well as designer preference among objectives were used to drive a feasible direction optimization algorithm. The feature of probabilistic satisfaction on constraints was demonstrated through a one-story shear structure subject to moderate lateral loads. However, there were several difficulties in setting the reliability index for each limit state. It was recognized that identifying an acceptable risk level requires experience and engineering judgement.

To improve the estimation on the reliability of a structure under multi-objective seismic performance, Takewaki et al (1991) presented a probabilistic multi-objective optimal design method for concentrically braced steel frames aimed at finding a satisfactory design with the least dissatisfaction level under multiple design conditions. The dissatisfaction level for constraints was computed based on the 84% probability distribution of maximum response obtained from response simulation for 100 artificial ground motions. The min-max problem algorithm was implemented to improve the dissatisfaction level. It was shown that the proposed optimization algorithm could be stopped at any stage within the feasible region depending upon the available computational resources. In addition to the practicality of the approach, the evaluated seismic response, in which only the maximum values of deformation and force were considered, may be argued.

Kramer and Grierson (1987) developed a methodology for the minimum weight design of planar frameworks subjected to dynamic loading. Constraints were placed on dynamic displacements, dynamic stresses, natural frequencies and member sizes. The method could account for combined axial and bending stresses, and could be used in designing minimum weight structures under simultaneous static and dynamic loading. Cheng et al (Cheng 1989; Truman 1989) formulated an optimization algorithm for both two and three dimensional, statically and dynamically loaded steel frames based on an optimality criteria approach. Constraints were

imposed on static and dynamic displacement and stress, and natural frequency. The theoretical work of scaling, sensitivity analyses, optimality criteria, and Lagrange multiplier determination had been presented. The dynamic analyses were based on the procedures of equivalent lateral forces and modal analysis methods. The objective functions of minimum construction and damage costs were considered. Memari (1999) presented a structural optimization problem based on the allowable stress design of two-dimensional braced and unbraced steel frames. Code-defined equivalent static force and response spectrum analysis methods were considered. A nonlinear constrained minimization algorithm was employed to improve the objective function (the minimum weight of structure) subjected to the behaviour constraints which included combined bending and axial stress, shear stress, buckling, slenderness, and drift. Cross-sectional areas were used as design variables. Although the proposed method could provide an efficient tool to conduct design under multiple performance constraints, the research work only considered structures within the range of elastic response.

The performance-based seismic design in which the requirements of structural performance are explicitly stated in probability terms has been developed in the last decade. The optimal performance-based design provides a tractable alternative to design a steel structure performing in a controllable way under various loading conditions. Foley (2002) provided background information needed to begin to develop design algorithms and procedures for the implementation of optimized performance-based engineering. In addition, a vision to the future of optimized Performance Based Design using state-of-the-art optimization and computational techniques was provided.

Liu et al (2003, 2006) presented a multi-objective optimization procedure for designing steel moment resisting frame buildings within a performance-based seismic design framework. The initial material costs, lifetime seismic damage costs and practical design complexity were taken as separate objectives. AISC-LRFD (American Institute of Steel Construction – Load and Resistance Factor Design) seismic provisions and NEHRP (National Earthquake Hazard Reduction Program) provisions were used to check the validity of any design alternative. To simplify the dynamic nonlinear analysis, an equivalent SDOF system obtained through a static pushover analysis of the original MDOF frame building was used to evaluate the seismic

performance. The maximum inter-story drift ratio at each hazard level corresponding to a specific exceedance probability formed a damage cost objective function. A modified standard Genetic Algorithm was implemented with the elastic analysis to search for Pareto optimal designs.

Gong, Xu and Grierson (2005) developed a computer-automated method for the optimum performance-based design of steel frameworks under (equivalent static) seismic loading. Seismic demands of the structures were evaluated using a nonlinear pushover analysis procedure. Explicit forms of the objective function and constraints in terms of member sizing variables were formulated to enable computer solution for the optimization model. Minimizing structural cost (interpreted as structural weight) was taken as one objective. The other objective concerned minimizing earthquake damage which was interpreted as providing a uniform inter-story drift distribution over the height of a building. A generalized optimality criteria algorithm was employed to find the least-weight structure that experiences minimal damage while simultaneously satisfying all performance constraints at all hazard levels. Zou and Chan (2005) proposed an effective computer-based technique that incorporated pushover analysis together with numerical optimization procedures to automate the pushover drift performance design of Reinforced Concrete (RC) buildings. Steel reinforcement ratios were taken as design variables during the design optimization process. The optimality criteria technique was implemented for solving the explicit performance-based seismic design optimization problem for RC buildings. It was noted that the proposed method was confined to pseudo-dynamic analysis.

Foley et al (2007) and Alimoradi et al (2007) cast performance-based design methodology into multiple-objective optimization problems in which reliability-based design was employed to quantify risk associated with designs. To reliably preserve life safety after rare ground motions as well as to minimize damage after more frequent ground motions were taken as the overall objectives. An evolutionary (genetic) algorithm with radial fitness and balanced fitness functions was developed to search for Pareto optimum designs. The application of the automated algorithm to design steel frames with fully restrained and a variety of partially restrained connections was illustrated through numerical examples.

1.4 Energy Method for Seismic Design

Since the energy-based design method (Housner 1956) was first presented, the approach has gained extensive attention (Uang 1990; Fajfar 1994; Zahrah 1984; Leger 1992; Filiatrault 1994; Akbas 2001; Chou 2003).

After Housner (1956) stated that seismic energy imparted to a SDOF system could be related to the velocity response spectrum of the system, a lot of research on the energy concept has been carried out. Zahrah and Hall (1984) used SDOF model to investigate the nonlinear response and damage potential as measured in terms of the amount of energy imparted to a structure and the amount of energy dissipated by inelastic deformation and by damping. The study showed that the degree of structural damage due to strong ground motions is not only dependent upon the maximum response of force or lateral displacement. Furthermore, structural damage does not correlate very well with peak ground acceleration. A good descriptor of the damage potential of an earthquake ground motion might be characterized by the amount of energy imparted to the structure. Tembulkar and Nau (1987) employed single-degree-of-freedom oscillator model to investigate the energy dissipation in inelastic structures. The results suggested that the use of bilinear model should be appropriately qualified in order to reliably predict the seismic energies imparted and dissipated. However, the studies had been limited to SDOF systems.

Cumulative yielding as a result of reversed inelastic deformations may still cause significant damage to a structure. Such cumulative damage resulting from dissipated hysteretic energy should be taken into account. It has been recognized that seismic input energy correlates better with structural damage (Housner 1956; Akbas 2001; Wong 2001; Saatcioglu 2003) as the energy, which serves as an alternative index to response quantities such as force or displacement, includes the duration-related seismic damage effect.

The important research work on the evaluation of seismic energy in structures has been carried out by Uang and Bertero (1990). In their paper, the inelastic input energy spectra for a SDOF system were constructed to predict the input energy to multi-storey buildings under earthquake ground motions. Good correlation was shown from the comparison between analytical prediction and experimental results.

Energy computations on MDOF systems have also been proposed by several researchers (Filiatrault 1994; Leger 1992). Filiatrault et al (1994) discussed using energy balance concept to appreciate plastic behaviour and to access accurate inelastic seismic response. The effects of algorithm damping in a numerical method have been investigated. Leger and Dussault (1992) studied the effects of various mathematical models representing viscous damping in nonlinear seismic analysis of MDOF structures. Damping was generally specified by numerical values of modal damping ratios to represent the inelastic energy dissipation in linear systems. These damping ratios would not be useful in inelastic dynamic analysis because the energy dissipation by yielding was accounted for separately through nonlinear force-deformation relationships. The study showed that the time-dependent Rayleigh damping model using the instantaneous stiffness with the proportionality coefficients computed from elastic properties provides very good agreement with the tangent damping model. Although knowledge on seismic energy of MDOF systems had been significantly advanced, there were still gaps between the sophisticated analyses and practical seismic designs.

Very recently, the design-related issues have been presented by several researchers (Akbas 2001; Chou 2003; Tso 1993). Most of the research concentrated on the methodology of employing inelastic energy spectra to evaluate nonlinear behaviour of building structures under severe earthquake ground motions.

Tso, Zhu, and Heidebrecht (1993) examined the correlation between the seismic energy demands of reinforced concrete ductile moment-resisting frames (DMRFs) and the equivalent single-degree-of freedom systems. It was shown that the concept of equivalent SDOF systems might be used to estimate the input and hysteretic energy demands for low-rise DMRFs. However, since the higher modal effect could not be accounted for, it underestimated the inelastic deformation at the upper floors of frames.

Akbas, Shen, and Hao (2001) suggested that cumulative plastic rotation capacity played an important role in degrading the stiffness of structure. Based on previous experimental studies, an assumed value of cumulative plastic rotation capacity for a welded-flange-bolted-web moment connection was assigned to be between 5 and 10 percent. An energy-based design procedure, in which hysteretic energy was only dissipated at beam ends, was proposed in respect to a pre-

defined energy interaction diagram. The degree of accuracy of the proposed method was highly dependent on the average of cumulative plastic rotation capacity and seismic energy input.

Chou and Uang (2003) developed a procedure to evaluate the absorbed seismic energy in a multistory frame from energy spectra. Since higher vibration modes also contribute to seismic energy dissipation, the actual hysteretic energy demand cannot be predicted either through a static pushover analysis or from an equivalent single-degree-of-freedom system. The proposed method combined static modal pushover analysis with a SDOF system energy spectrum to evaluate the seismic energy demand of frame structures. It showed that the damage distribution of low- to medium-rise frames could be predicted through the combination of first two modes.

As part of the work for this thesis, Gong, Xue, Xu, and Grierson (2012) proposed an energy-based design optimization method for steel building frameworks subjected to seismic loading using a nonlinear response history analysis procedure.

1.5 Thesis Outline

The objective of this research is to develop a general capacity design optimization methodology for various steel building frameworks. Nonlinear time-history analysis is employed to obtain seismic demands of a structure subjected to earthquake ground motions. Hysteretic energy dissipations of structural members as well as the seismic input energy of seismic force resisting systems are used as the quantitative descriptions of seismic response.

The thesis is organized in the following manner:

Chapter 1 provides the background of this research. A literature survey on structural optimization, seismic design optimization, and energy method for seismic design are presented.

Chapter 2 describes the nonlinear dynamic analysis approach for seismic design of steel building frameworks. A method for calculating seismic input energy and hysteretic energy using the structural responses obtained from a nonlinear time-history analysis is proposed.

Chapter 3 presents the formulation of the multi-objective optimization problem. Genetic Algorithm for solving the optimization problem is discussed.

Chapter 4 outlines the design examples of Moment Resisting Frames. The feasibility and practicability of the proposed design optimization methodology is demonstrated through numerical examples.

Chapter 5 discusses the design of Eccentrically Braced Frames.

Chapter 6 summarizes the contributions and conclusions resulting from the study, and gives recommendations for future study.

1.6 Assumptions and Idealizations

The following assumptions and idealizations are adopted in this research:

1) The layout of the building structures is predefined and fixed throughout a design process.
2) All framing members are prismatic and are selected from among commercially available steel section shapes, unless otherwise noted. The cross-section sizes are chosen as design variables.
3) All members are adequately braced such that lateral-torsional buckling can be neglected.
4) Only compact sections are chosen to ensure the members can develop inelastic behaviour.
5) Only fully rigid or ideally pinned connection models are considered in a design process.
6) Except for the shear link model where shear deformation is directly considered, shear deformation is assumed to be negligible.
7) The model for panel zone at column-beam joints is not included.
8) Only two-dimensional plane models for steel frameworks are considered. The contribution of a floor slab to beam stiffness and strength is not considered.

Chapter 2

Nonlinear Dynamic Analysis Approach for Seismic Design

Earthquake response of building structures is a dynamic phenomenon. The deformations and stresses within a structure are created by its dynamic response to the random movement of its base. Steel frameworks are generally expected to experience deformations that impart significant inelastic demand during a strong earthquake motion.

2.1 Energy-Based Dynamic Analysis

The quantitative description of structural demand subjected to strong earthquake ground motions has always been a challenging problem for the seismic design profession. The maximum deformation values or ductility factors induced by a single plastic excursion do not describe cumulative effects of earthquake ground motions. Capturing the time-dependent damage sustained during strong earthquake ground motions is particularly interesting to seismic researchers. Energy, which relates to not only force and deformation but also to the duration of earthquake ground motions, has been proposed to evaluate structural damage or demand levels.

During a strong earthquake ground motion, the seismic energy imparted to a building is dissipated through the movements and deformations of structural members in the forms of kinetic energy, damping energy, elastic strain energy and inelastic hysteretic energy (Uang et al 1990). It is well accepted (Zahrah 1984; Tembulker 1987; Uang 1990; Filiatrault 1994; Leger 1992) that a structure can survive a strong earthquake if its structural energy absorption capacity is greater than the input seismic energy. From a system viewpoint, the potential damage or seismic demand of an earthquake ground motion can be characterized by the amount of energy imparted to a system. Generally, less structural damage can be expected if seismic input energy is effectively reduced.

It has been shown (Housner 1956) that the ability of a structure to absorb seismic energy is critical for the structure to survive a strong earthquake. The input energy for an inelastic system is dissipated by both damping and yielding when the structure comes to rest after an earthquake. In the case that no damper is provided for a structural system (which is the case for this study)

the structural system needs to be designed to have sufficient capacity to dissipate energy by material yielding (i.e., hysteretic energy capacity). Hysteretic energy calculation involves considering the entire history of structural response, thus it reflects the cumulative effects of material yielding (Pires 1994). For a structural member, the estimation serves as a good indicator of the extent of its sustained plastification. The better estimation of distribution of nonlinear response within a SFRS can be obtained through hysteretic energy evaluation.

In this research, hysteretic energy and seismic input energy are employed as primary performance indicators of a SFRS.

2.1.1 Seismic Energy Equation

The equation of motion of a MDOF system is written as

$$[M]\{\ddot{u}(t)\} + [C]\{\dot{u}(t)\} + \{F_r(t)\} = -[M]\{r\}\ddot{x_g}(t) \qquad (2 - 1)$$

where [M] is the global mass matrix; [C] is the global viscous damping matrix; $\{F_r(t)\}$ is the global nonlinear restoring force vector at time t; $\{\ddot{u}(t)\}, \{\dot{u}(t)\}, \{u(t)\}$ are the response vectors of acceleration, velocity, and displacement respectively; $\{r\}$ is the support influence vector; $\ddot{x_g}(t)$ is the ground acceleration at time t.

Energy E is the work done by a force through a distance. It is computed with respect to the time varying force $F(t)$ and the associated displacement $d\{u(t)\}^T$, where superscript T refers to the transpose of a vector.

$$E = \int d\{u(t)\}^T F(t) \qquad (2 - 2)$$

Using the differential relationships between displacement, velocity and acceleration,

$$d\{u(t)\} = \{\dot{u}(t)\}\, dt \qquad (2 - 3)$$

$$d\{\dot{u}\,(t)\} = \{\ddot{u}(t)\}\, dt \qquad (2 - 4)$$

the various energy terms can be defined by transforming Equation (2 - 1) into an energy equation. By pre-multiplying the transpose of displacement increment $d\{u(t)\}^T$ and integrating over displacement domain, Equation (2 - 1) becomes

$$\int_0^t \{\dot{u}\,(t)\}^T[M]\{\ddot{u}(t)\}\,dt + \int_0^t \{\dot{u}\,(t)\}^T[C]\{\dot{u}(t)\}\,dt + \int_0^t \{\dot{u}\,(t)\}^T\{F_r(t)\}\,dt = -\int_0^t \{\dot{u}\,(t)\}^T[M]\{r\}\ddot{x}_g(t)\,dt \quad (2 - 5)$$

Equation (2 - 5) can be replaced in favour of displacement and velocity variables. The energy balance equation is rewritten as

$$E_k(t) + E_d(t) + E_a(t) = E_i(t) \quad (2 - 6)$$

where

$$E_k(t) = \int_0^{\dot{u}} \{\dot{u}(t)\}^T[M]\,d\{\dot{u}(t)\} \quad (2 - 7)$$

$$E_d(t) = \int_0^{u} \{\dot{u}(t)\}^T[C]\,d\{u(t)\} \quad (2 - 8)$$

$$E_a(t) = \int_0^{u} d\{u(t)\}^T\{F_r(t)\} \quad (2 - 9)$$

$$E_i(t) = -\int_0^{u} d\{u(t)\}^T[M]\{r\}\ddot{x}_g(t) \quad (2 - 10)$$

E_k represents kinetic energy and E_d is damping energy. The absorbed energy, E_a, is composed of recoverable elastic strain energy, E_s, and irrecoverable hysteretic energy, E_h. E_i represents relative seismic input energy. From the standpoint of energy balance, Equation (2 - 6) shows that the seismic input energy $E_i(t)$ imparted into a structure is equal to the sum of the kinetic energy $E_k(t)$, the damping energy $E_d(t)$ and the absorbed energy $E_a(t)$.

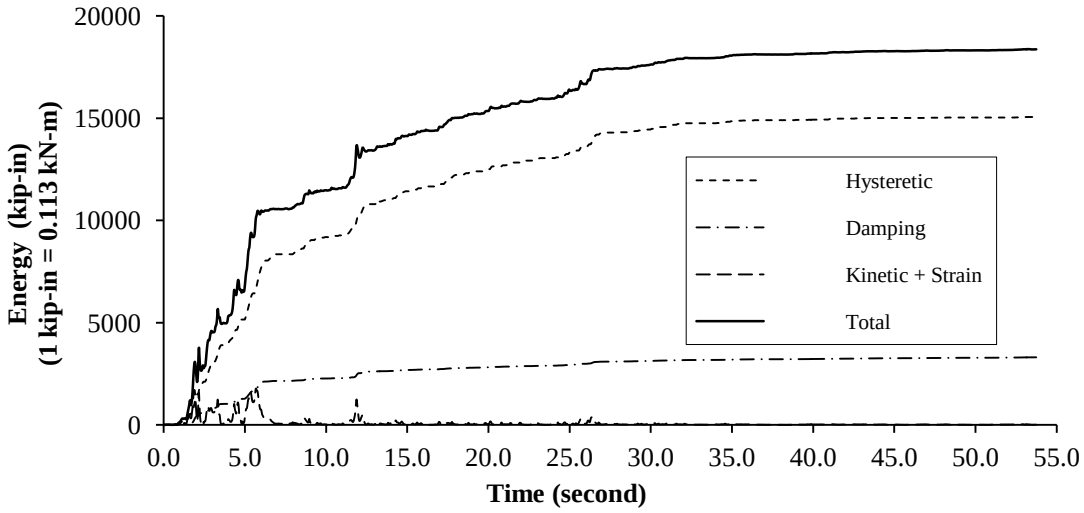

Figure 2-1 Typical energy time history (Charney 2004)

Traditional energy-based design methods usually estimate seismic energy from an equivalent SDOF system (Uang and Bertero 1990; Chou and Uang 2003). Figure 2-1 shows the energy time-histories of an inelastic SDOF system (Charney 2004). It can be seen that the seismic input energy continually increases during the ground motion. The SDOF method is based on the assumption that the vibration shape developed during its motion can be determined by a single-degree-of-freedom system. However, a steel building framework is an assemblage of beams and columns connected at their ends and thus possesses a number of degrees of freedom. The approximations obtained from a SDOF analysis cannot represent well the true dynamic behavior of steel building frameworks. To accurately predict the seismic energy demand as well as the hysteretic energy dissipation of building structures, a MDOF system model has to be included in an analysis procedure. In the following, an approach to obtain seismic energies of a MDOF steel building framework is proposed by making use of the results of an existing nonlinear time-history analysis procedure.

2.1.2 Seismic Energy Computation

Seismic Input Energy

As shown in Equation (2 - 1), earthquake action on a SFRS can be interpreted as the inertial forces resulting from the acceleration of ground motions. The seismic input energy E_i (t) in

Equation (2 - 10), is a system level indicator of potential damage or demand description of a SFRS.

It should be noted that the seismic input energy, E_i (t), represents the energy supplied by $-[M]\{r\}\ddot{x}_g(t)$ instead by base movement, $\ddot{x}_g(t)$; and for this reason, $E_i(t)$ is called a 'relative' seismic input energy. As it was pointed out by Chopra (2007) that it is more meaningful to employ an energy equation expressed in terms of relative motion than the one formulated in terms of absolute velocity and displacement since it is the relative displacements that cause forces in a structure.

For a MDOF system, its seismic input energy can be obtained by the following numerical formulations:

$$E_i(t) = \sum E_{i,m}(t) \quad , \qquad (m = 1,2, \dots n_m) \tag{2 - 11}$$

where n_m is the number of degrees-of-freedom; $E_{i,m}(t)$ is the seismic input energy of the m^{th} degree-of-freedom at time t; and

$$E_{i,m}(t) = E_{i,m}(t - \Delta t) + \frac{1}{2}\left(\Delta u_{t,m} + \Delta u_{t-\Delta t,m}\right) F^{i}{}_{t,m} \tag{2 - 12}$$

where

$$F^{i}{}_{t,m} = -M_m \, \ddot{x}_{g,t} \tag{2 - 13}$$

$F^{i}{}_{t,m}$ is the inertial force vector of the m^{th} degree-of-freedom at time t; M_m is the mass value of the m^{th} degree-of-freedom; $\ddot{x}_{g,t}$ is the ground acceleration at time t; $\Delta u_{t,m}$, $\Delta u_{t-\Delta t,m}$ are the displacement increments of m^{th} degree-of-freedom at time t and t-Δt, respectively.

Hysteretic Energy Dissipation

Compared to an elastic system, it is possible for an inelastic structural system to achieve less kinetic and strain energy demand since its hysteretic energy dissipates part of the input energy.

The performance of a SFRS under a strong earthquake ground motion relies more on its hysteretic energy dissipation capability since the properties of damping do not change significantly.

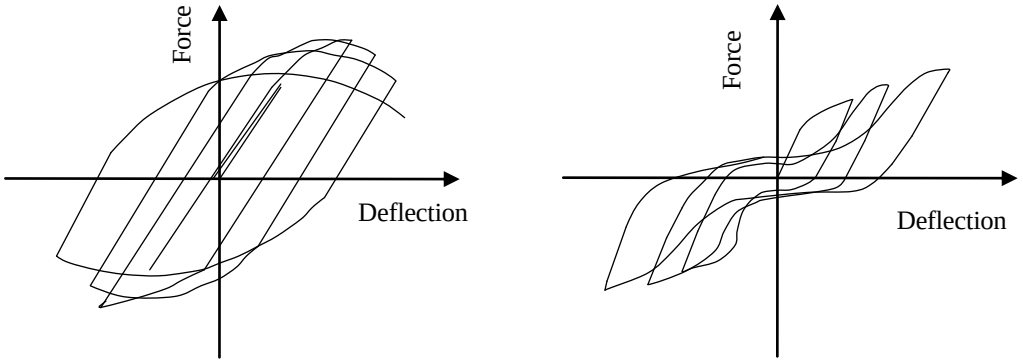

a) Ductile hysteretic loops

b) Pinched hysteretic loops

Figure 2-2 Typical hysteretic curves

At the structural system level, the energy dissipated through hysteretic behaviour can be computed from the area enclosed by the lateral force-deformation curve of the SFRS as the structure undergoes cyclic inelastic deformation. The representative lateral force-deformation curves for two SFRSs are shown in Figure 2-2. Both systems possess the same strength and deformation capacity. Figure 2-2-a shows a hysteretic behaviour in which nearly all of the strength and stiffness of the SFRS can be maintained over a large number of cycles of inelastic deformation. The wide and open force-deformation "loops" indicate that a large amount of energy can be dissipated through hysteretic behaviour. On the other hand, Figure 2-2-b illustrates a pinched hysteretic behaviour in which the SFRS suffers a rapid loss of stiffness under repeated inelastic deformation. It is evident that the hysteretic energy dissipated through the inelastic behaviours of the system shown in Figure 2-2-b is much lower than that of the system shown in Figure 2-2-a. Conceptually, it can be concluded that the system shown in Figure 2-2-a will have a higher level of possibility to survive under a severe earthquake ground motion. As a result, maximizing the hysteretic energy dissipation capacity of a SFRS is usually one of the pursuits of seismic design. Following such a design philosophy, seismic provisions always recommend that a proper seismic design of a SFRS should employ an appropriate hysteretic energy dissipation

mechanism to meet seismic energy demands rather than maintaining elastic structural response under severe earthquake events.

In general, the actual capacity of hysteretic energy dissipation of a building structure depends not only on the ductility of individual structural members but also upon the strength hierarchy and the assemblage formulation among the system, and the dynamic characteristics of the earthquake ground motion. In seismic design practice, it has been shown that various inelastic deformation distributions among a SFRS do not lead to the same hysteretic energy dissipation capacity (Paulay and Priestly 1992). Sometimes the differences are significant. Accordingly, capacity design philosophy is employed to ensure structures dissipate seismic energy in a predictable and stable manner under strong earthquakes. For steel Moment Resisting Frames (MRFs), it is preferred to dissipate (FEMA 2004a; NRCC 2010) a large amount hysteretic energy through formation of plastic hinges at the ends of beams rather than at the ends of columns. Namely, beams are usually chosen as fuse members while columns are designed to deform elastically (except at column bases where plastic hinges are often needed to allow for lateral inelastic drift) to meet strength requirements. For steel Eccentrically Braced Frames (EBFs), shear links, which are detailed to sustain the large inelastic deformations and thus have stable inelastic shear force-deformation loops, are used as fuses to dissipate seismic energy and to protect the remainders of the EBF from yielding.

When a structure is designed following the capacity design principle, the structure is conceptually expected to form a favourable seismic energy dissipation mechanism under earthquake. However, the extent of realizing the desired hysteretic energy dissipation mechanism cannot be actually examined through an elastic analysis procedure. In order to quantify, rather than just qualify, the hysteretic energy dissipation of a SFRS under an earthquake ground motion, the dynamic response history of each individual member needs to be accounted for. The hysteretic energy dissipation of a group of structural members can then be obtained by summing the energies of individual members of the group. In this way, the hysteretic energy dissipations of fuse and non-fuse members can be compared directly and the hysteretic energy dissipation mechanism can be examined quantitatively.

In this section, a numerical approximation method to calculate the hysteretic energy of one structural member is proposed by utilizing its seismic response history. The hysteretic energy dissipations of fuse and non-fuse members will be employed as energy performance parameters to direct the optimal design procedure.

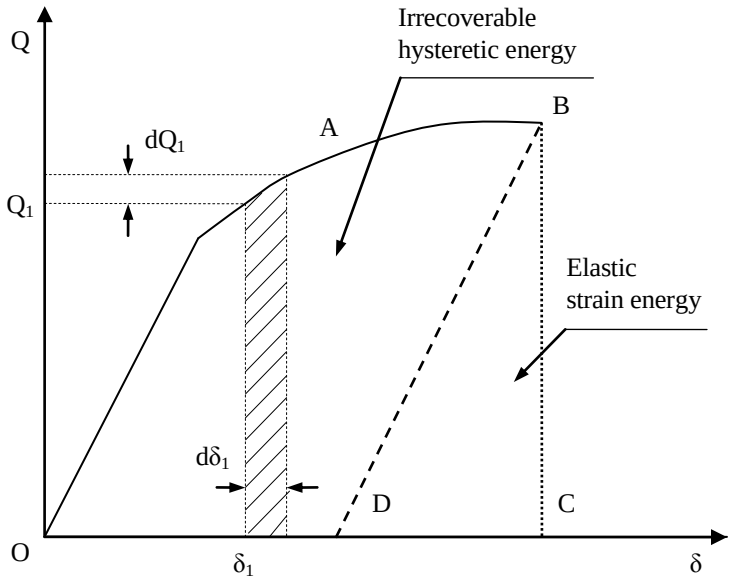

Figure 2-3 Elastic strain energy and irrecoverable hysteretic energy of structural members

Strains or deformations are produced when internal forces are induced within structural members. Strain energy describes the energy absorbed during the deformation process. According to the law of conservation of energy, the absorbed strain energy is equal to the work done by the internal forces if no energy enters or leaves in the form of heat (Philpot 2008). To evaluate this work, the manner in which the internal forces vary in respect to the deformations must be known. In the typical force-deformation diagram of a structural member, as shown in Figure 2-3, the vertical axis represents the generalized force (which may be the axial force, bending moment, or shear force) and the horizontal axis represents the corresponding deformation of the structural member. For a value of force Q_1 on the load-deformation curve, its corresponding deformation is denoted as δ_1. As an increment dQ_1 of the force produces an increment deformation $d\delta_1$, the work done by the force during this incremental deformation is expressed as $Q_1 d\delta_1$. Geometrically, the incremental work is represented by the area of the elemental strip below the force-deformation

curve in Figure 2-3. Consequently, the total work done by the force up to point B on the curve can be denoted as the area below the load-deformation curve, i.e.,

$$W = \int_0^{\delta} Q \, d\delta \qquad (2 - 14)$$

For a structural member undergoing an inelastic strain beyond the elastic limit, a residual or permanent strain remains in the member. As shown in Figure 2-3, the unloading line will be parallel to the initial elastic portion of the curve when the force is removed. Of the total deformation OC developed during the loading process, only portion CD is recovered and portion OD remains as a permanent deformation. As a result, only part of the strain energy (i.e., the area of triangle BCD) is recovered. The area OABD represents the energy permanently lost during the loading history, i.e., irrecoverable hysteretic energy.

Various schemes are available to carry out the computation of hysteretic energy. The method proposed hereafter is to utilize the force and displacement histories of structural members obtained through the nonlinear time-history analysis procedure. For a frame member in a SFRS, bending moment, axial force, and shear force are the primary internal force resultants. The frame member will undergo flexing, changing in length, and warping in respect to these internal forces, respectively. The hysteretic energy dissipation of a structural member $E_{h,k}$ at the end of an earthquake is expressed as the sum of the work of internal forces and corresponding displacements, i.e.,

$$E_{h,k} = W_{Moment,k} + W_{Axial,k} + W_{Shear,k} \qquad (k = 1,2, \dots n_e) \qquad (2 - 15)$$

where

$$W_{Moment,k} = \sum \frac{1}{2} \left(\Delta\varphi_{t,k} + \Delta\varphi_{t-\Delta t,k} \right) M_{t,k} \qquad (2 - 16)$$

$$W_{Axial,k} = \sum \frac{1}{2} \left(\Delta x_{t,k} + \Delta x_{t-\Delta t,k} \right) P_{t,k} \qquad (2 - 17)$$

$$W_{Shear,k} = \sum \frac{1}{2}\left(\Delta y_{t,k} + \Delta y_{t-\Delta t,k}\right) V_{t,k} \qquad (2 - 18)$$

$W_{Moment,k}$, $W_{Axial,k}$, and $W_{Shear,k}$ are the work done by the bending moment, axial force and shear force of the k^{th} member, respectively; and n_e is the number of the structural members. $M_{t,k}$, $P_{t,k}$, and $V_{t,k}$ are the internal bending moment, axial force and shear force of the k^{th} structural element at time t, respectively. $\Delta\varphi_{t,k}$, $\Delta x_{t,k}$, and $\Delta y_{t,k}$ are the increments of end rotation, axial deformation and shear deformation of the k^{th} structural element from time (t-Δt) to time t, respectively. The summation starts from time zero to the time point at which the time-history analysis ends. Then, the hysteretic energy E_h can be expressed as

$$E_h = \sum E_{h,k} \quad (k = 1,2, \dots n_e) \qquad (2 - 19)$$

2.2 Structural Analysis Method

2.2.1 Nonlinear Time History Analysis

As a building structure deforms into its inelastic region, where the equation of motion governing the dynamic response is denoted as Equation (2 - 1), the restoring force and the damping force vectors may not remain proportional to the displacement or the velocity, respectively. Furthermore, the ground motion acceleration varies arbitrarily with time, the analytical solution of Equation (2 - 1) is usually impossible. As a consequence, the nonlinear responses of a MDOF system will generally require a numerical procedure for the integration of differential equations.

A ground motion record is given by a set of discrete values (i.e., $\ddot{x}_{g,i} = \ddot{x}_g(t_i)$, $i = 0\ to\ N$), the displacement, velocity, and acceleration vectors of a MDOF system are assumed to be known as $\{u\}_i = \{u(t_i)\},\ \{\dot{u}\}_i = \{\dot{u}(t_i)\},\ and\ \{\ddot{u}\}_i = \{\ddot{u}(t_i)\}$ at time-step i, as well as the restoring force vector $\{F_r\}_i = \{F_r(t_i)\}$.

These values satisfy Equation (2 - 1) at time-step i

$$[M]\{\ddot{u}\}_i + [C]\{\dot{u}\}_i + \{F_r\}_i = -[M]\{r\}\ddot{x}_{g,i} \qquad (2 - 20)$$

The response quantities $(i.e., \{u\}_{i+1}, \{\dot{u}\}_{i+1}, \{\ddot{u}\}_{i+1}, \{F_r\}_{i+1})$ at a small time later, time i+1 (where $t_{i+1} = t_i + \Delta t$), also satisfy Equation (2 - 1)

$$[M]\{\ddot{u}\}_{i+1} + [C]\{\dot{u}\}_{i+1} + \{F_r\}_{i+1} = -[M]\{r\}\ddot{x}_{g,i+1} \qquad (2 - 21)$$

The incremental equilibrium equation of motion of the MDOF system can be obtained by subtracting Equation (2 - 20) from Equation (2 - 21), i.e.,

$$[M]\Delta\{\ddot{u}\}_{t+\Delta t} + [C]\Delta\{\dot{u}\}_{t+\Delta t} + \Delta\{F_r\}_{t+\Delta t} = -[M]\{r\}\Delta\ddot{x}_{g,t+\Delta t} \qquad (2 - 22)$$

where:

$$\Delta\{\ddot{u}\}_{t+\Delta t} = \{\ddot{u}\}_{i+1} - \{\ddot{u}\}_i \qquad (2 - 23)$$

$$\Delta\{\ddot{u}\}_{t+\Delta t} = \{\ddot{u}\}_{i+1} - \{\ddot{u}\}_i \qquad (2 - 24)$$

$$\Delta\{F_r\}_{t+\Delta t} = \{F_r\}_{i+1} - \{F_r\}_i \qquad (2 - 25)$$

$$\Delta\ddot{x}_{g,t+\Delta t} = \ddot{x}_{g,i+1} - \ddot{x}_{g,i} \qquad (2 - 26)$$

Although the restoring force vector $\{F_r\}$ will not be proportional to the displacement vector $\{u\}$ when the structure deforms into its inelastic region, the incremental restoring force vector $\Delta\{F_r\}_{t+\Delta t}$ may be linearly approximated by assuming the tangent stiffness matrix $[K]_T$ constant during the time increment Δt,

$$\Delta\{F_r\}_{t+\Delta t} = [K]_T\, \Delta\{u\}_{t+\Delta t} \qquad (2 - 27)$$

where $\Delta\{u\}_{t+\Delta t} = \{u\}_{i+1} - \{u\}_{i.}$. Subsequently, the equation of motion of the MDOF system can be approximated by a series of linear incremental equilibrium equations,

$$[M]\Delta\{\ddot{u}\}_{t+\Delta t} + [C]\Delta\{\dot{u}\}_{t+\Delta t} + [K]_T\, \Delta\{u\}_{t+\Delta t} = -[M]\{r\}\Delta\ddot{x}_{g,t+\Delta t} \qquad (2 - 28)$$

Employing Newmark method of direct integration, in which the variation of acceleration over the time increment Δt is defined through the following equations by using parameters β and γ,

$$\Delta\{\dot{u}\}_{t+\Delta t} = [(1-\gamma)\,\Delta t\,]\,\{\ddot{u}\}_i + (\gamma\,\Delta t)\,\{\ddot{u}\}_{i+1} \qquad (2\text{ - }29)$$

$$\Delta\{u\}_{t+\Delta t} = \Delta t\,\{\dot{u}\}_i + [(0.5-\beta)\,(\Delta t)^2\,]\,\{\ddot{u}\}_i + [\beta\,(\Delta t)^2\,]\,\{\ddot{u}\}_{i+1} \qquad (2\text{ - }30)$$

The structural response can be determined by an effective linear equation to calculate the incremental displacement $\Delta\{u\}_{t+\Delta t}$

$$\widehat{[K]}\Delta\{u\}_{t+\Delta t} = \Delta\widehat{\{F\}} \qquad (2\text{ - }31)$$

where:

$$\widehat{[K]} = [K]_T + \frac{\gamma}{\beta\,\Delta t}\,[C] + \frac{1}{\beta\,(\Delta t)^2}\,[M] \qquad (2\text{ - }32)$$

$$\begin{aligned}\Delta\widehat{\{F\}} = {} & -[M]\{r\}\Delta\ddot{x}_{g,t+\Delta t} + \left(\frac{1}{\beta\,\Delta t}\,[M] + \frac{\gamma}{\beta}\,[C]\right)\{\dot{u}\}_i \\ & + \left[\frac{1}{2\beta}\,[M] + \Delta t\left(\frac{\gamma}{2\beta}-1\right)[C]\right]\{\ddot{u}\}_i\end{aligned} \qquad (2\text{ - }33)$$

Given the known initial conditions,$\{u\}_0 = 0\ and\ \{\dot{u}\}_0 = 0$, the quantities of structural response $\{\ddot{u}\}_{i+1}$, $\{\dot{u}\}_{i+1}\ and\ \{u\}_{i+1}$ at time step i+1 can be successively determined by using Equations (2 - 22) to (2 - 33).

In the implementation of the Newmark method, the values of β and γ in Equations (2 - 29) and (2 - 30) need to be selected in advance. In this research, β = 0.25 and γ = 0.5 are adopted, since it has been proven that the Newmark method is unconditionally stable when these parameter values are used (Chopra 2007; Paz 1991).

For an inelastic system, a non-iterative procedure (i.e., from Equation (2 - 28) to Equation (2 - 33)) can lead to inaccurate results. As shown in Figure 2-4, discrepancies due to the use of the

tangent stiffness matrix can accumulate significant errors over a series of time steps. However, the errors can be minimized by using Newton-Raphson iteration procedure.

To improve the numerical estimation during each time interval Δt, the iterative procedure starts with the effective linear stiffness matrix $[\widehat{K}]^{(0)}$ and the initial unbalanced force $\Delta\{R\}^{(0)}$ corresponding to displacement state of time t_i,

$$\Delta\{u\}^{(1)} = \left([\widehat{K}]^{(0)}\right)^{-1} \Delta\{R\}^{(0)} \qquad (2 - 34)$$

where $\Delta\{u\}^{(1)}$ is the first approximation to the final increment $\Delta\{u\}_{t+\Delta t}$; $\Delta\{R\}^{(0)}$ is equal to the incremental force vector $\Delta\{\widehat{F}\}$ calculated from Equation (2 - 33). In consequence, the first approximation to deformation state of the whole system can be determined from ${\{u\}_{i+1}}^{(1)} = \{u\}_i + \Delta\{u\}^{(0)}$.

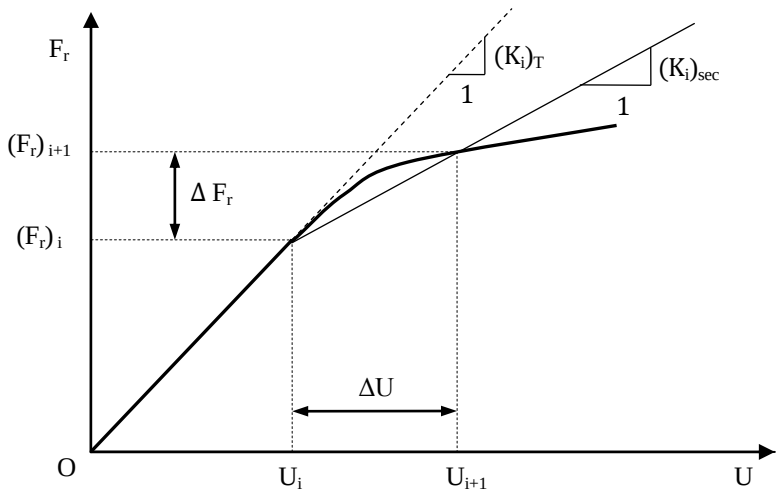

Figure 2-4 Illustration of tangent stiffness and secant stiffness

The force state, $\Delta\{f\}^{(1)}$, associated with ${\{u\}_{i+1}}^{(1)}$ is evaluated to determine the corresponding unbalanced force vector $\Delta\{R\}^{(1)}$,

$$\Delta\{R\}^{(1)} = \Delta\{R\}^{(0)} - \Delta\{f\}^{(1)} \qquad (2 - 35)$$

The effective linear stiffness matrix, $[\widehat{K}]^{(1)}$, is re-evaluated corresponding to the displacement state of $\Delta\{u\}^{(1)}$ by using Equation (2 - 32).

Then, the second approximation $\Delta\{u\}^{(2)}$ is calculated by using the new effective stiffness matrix, $[\widehat{K}]^{(1)}$, and the new unbalanced force $\Delta\{R\}^{(1)}$

$$\Delta\{u\}^{(2)} = \left([\widehat{K}]^{(1)}\right)^{-1} \Delta\{R\}^{(1)} \qquad (2 - 36)$$

The iterative process will continue until convergence is achieved. Once the norm of the incremental displacement $\Delta\{u\}^{(c)}$ or the norm of the unbalanced force $\Delta\{R\}^{(c)}$ is less than a specified tolerance, the final estimate of incremental displacement vector can be obtained,

$$\Delta\{u\}_{t+\Delta t} = \sum_{j=1}^{c} \Delta\{u\}^{(j)} \qquad (2 - 37)$$

With $\Delta\{u\}_{t+\Delta t}$ known, the final estimate of incremental velocity and acceleration vector can be solved using Equations (2 - 29) and (2 - 30),

$$\Delta\{\dot{u}\}_{t+\Delta t} = \frac{\gamma}{\beta\,\Delta t}\,\Delta\{u\}_{t+\Delta t} - \frac{\gamma}{\beta}\{\dot{u}\}_i + \left[\left(1 - \frac{\gamma}{2\beta}\right)\Delta t\right]\{\ddot{u}\}_i \qquad (2 - 38)$$

$$\Delta\{\ddot{u}\}_{t+\Delta t} = \frac{1}{\beta\,(\Delta t)^2}\,\Delta\{u\}_{t+\Delta t} - \frac{1}{\beta\,\Delta t}\{\dot{u}\}_i - \frac{1}{2\beta}\{\ddot{u}\}_i \qquad (2 - 39)$$

Consequently, the quantities of $\{u\}_{i+1}$, $\{\dot{u}\}_{i+1}$, $and\ \{\ddot{u}\}_{i+1}$ are ready for the next time step. The Newmark numerical integration method together with the Newton-Raphson iteration procedure traces the displacement state of the whole MDOF system step-by-step till the end of the excitation time history.

As shown in the incremental equilibrium equation (2 - 28), the direct numerical procedure of integration for differential equations requires an explicit damping matrix [*C*]. However, the damping properties of materials are not well established, and it is impractical to form the damping matrix [*C*] directly from the properties of a structure. To account for the non-yielding

energy dissipation effect (such as the energy dissipated in friction at steel connections, stressing of non-structural elements, and other similar mechanisms) in MDOF systems, the equivalent viscous damping with recommended modal damping ratios varying between 3% and 7% is adopted in structural engineering profession (Chopra 2007). Consequently, the damping matrix $[C]$ of a MDOF system can be determined from its modal damping ratios to simplify the implementation. It should be noted that an increased damping ratio is often employed to estimate energy losses due to anticipated inelastic effect in an elastic linear analysis. Such increased damping values should be avoided in a nonlinear time-history analysis since the energy dissipation effect of yielding is directly included in the analysis procedure.

It has been proven that classical Rayleigh-type damping is an appropriate idealization for the dynamic analysis of a MDOF system (Leger and Dussault 1992; Paz 1991). For nonlinear time-history analysis, a tangent damping matrix $[C]_t$ is employed to account for the continuous changes in structural characteristics along the step-by-step numerical integration. Generally, the tangent damping matrix $[C]_t$ can be expressed as a linear combination of mass matrix $[M]$ with various stiffness matrixes $[K]$,

$$[C]_t = a_m[M] + b_t[K]_t + b_i[K]_i + b_c[K]_c \qquad (2 - 40)$$

where $[K]_t$ is the tangent stiffness matrix of the current iteration; $[K]_i$ is the initial elastic stiffness matrix; $[K]_c$ is the last converged stiffness matrix of the current iteration; a_m, b_t, b_i and b_c are the proportionality constants computed using the natural frequencies of the MDOF system.

The tangent damping matrix $[C]_t$ computed based on the initial stiffness matrix $[K]_i$ represents constant damping during the analysis. On the other hand, the tangent damping matrix $[C]_t$ computed using either the tangent stiffness matrix $[K]_t$ or the last converged stiffness matrix $[K]_c$ of the current iteration accounts for the changes of stiffness matrix $[K]$ in the process of time-history analysis.

To be consistent with the aforedescribed step-by-step numerical integration procedure and Newton-Raphson method, the tangent stiffness matrix $[K]_t$ of the current iteration is used (i.e., $b_i = 0$ and $b_c = 0$) in Equation (2 - 40). Given two distinct frequencies, ω_p and ω_q (in practice, ω_p is

taken as the first natural frequency and ω_q is taken as the highest frequency to be considered in the analysis), with damping ratios ξ = 5%, coefficients a_m and b_t are expressed as

$$a_m = \frac{2\,\xi\,\omega_p\,\omega_q}{\omega_p + \omega_q} \qquad (2 - 41)$$

$$b_t = \frac{2\,\xi}{\omega_p + \omega_q} \qquad (2 - 42)$$

where, ω_p and ω_q are computed based on the initial elastic stiffness of the structure. The experimental results agreed reasonably well with such determined damping matrix (Leger and Dussault 1992).

During the Newton-Raphson iteration process defined by Equation (2 - 34) to Equation (2 - 37), the determination of a force state corresponding to the displacement or deformation state of the current time-step involves evaluation of both material and geometric nonlinearities. This simulation of the nonlinearity of individual members is essential for structural nonlinear analysis.

2.2.2 Geometric and Material Nonlinear Analysis

Geometric and Material nonlinearities are two major concerns in the analysis of steel structures. The nonlinearity properties of structural members are generally represented by advanced analytical finite element models. Meanwhile, the structural responses, such as displacements and internal forces, are approximated element by element through the aforementioned nonlinear time-history analysis procedure.

Geometric Nonlinear Analysis

For a two-dimensional frame element, there are 6 unknown forces (with 3 at each end of the element). As the corotational formulation of the frame element (Crisfield 1991) shown in Figure 2-5, it is assumed that (1) the basic system changes orientation as the element deforms; and (2) the basic forces act on the deformed element with w_1 always along the deformed element chord.

Practically, 3 element forces (i.e., axial force w_1, end bending moment w_2 and w_3) are selected as the basic forces to express the remainders by using 3 independent equilibrium equations.

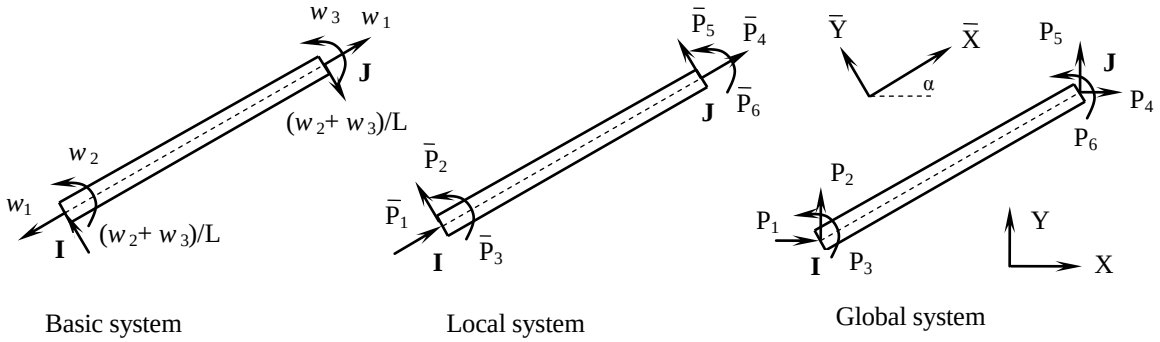

Figure 2-5 Element forces in different systems

Considering equilibrium equations with respect to the un-deformed configuration, the element end forces $\overline{\boldsymbol{p}}$ in the local coordinate system can be expressed in terms of the equilibrium transformation matrix $\boldsymbol{b}$,

$$\overline{\boldsymbol{p}} = \begin{pmatrix} \overline{p}_1 \\ \overline{p}_2 \\ \overline{p}_3 \\ \overline{p}_4 \\ \overline{p}_5 \\ \overline{p}_6 \end{pmatrix} = \begin{bmatrix} -1 & 0 & 0 \\ 0 & 1/L & 1/L \\ 0 & 1 & 0 \\ 1 & 0 & 0 \\ 0 & -1/L & -1/L \\ 0 & 0 & 1 \end{bmatrix} \begin{pmatrix} w_1 \\ w_2 \\ w_3 \end{pmatrix} = \boldsymbol{b}\,\boldsymbol{w} \qquad (2 - 43)$$

By employing a rotation transformation matrix $\boldsymbol{b}_r$, the element end forces $\boldsymbol{p}$ in the global coordinate system can be stated as $\boldsymbol{p} = \boldsymbol{b}_r\,\overline{\boldsymbol{p}}$. Then, the equilibrium equations with respect to the un-deformed configuration are expressed as

$$\boldsymbol{p} = \boldsymbol{b}_e \boldsymbol{w} \qquad (2 - 44)$$

where $\boldsymbol{b}_e = \boldsymbol{b}_r\,\boldsymbol{b}$. Similar to the transformation of the equilibrium equations from the basic system to the global coordinate system, the geometric displacement-deformation compatibility relation

which transforms displacement $\boldsymbol{u}$ in the global coordinate system to the basic deformation $\boldsymbol{v}$ (corresponding to the basic force $\boldsymbol{w}$) is expressed symbolically as

$$\boldsymbol{v} = \boldsymbol{a}_r\, \overline{\boldsymbol{u}} = \boldsymbol{a}_r\, (\boldsymbol{a}\, \boldsymbol{u}) = \boldsymbol{a}_g\, \boldsymbol{u} \qquad (2 - 45)$$

where $\boldsymbol{a}_g = \boldsymbol{a}_r\, \boldsymbol{a}$. By employing the virtual displacement principle which states that the work done by element end force $\boldsymbol{p}$ on the virtual displacements $\boldsymbol{\delta u}$ is equal to the work done by internal force $\boldsymbol{w}$ on the compatible virtual deformation $\boldsymbol{\delta v}$, i.e.,

$$\boldsymbol{\delta u}^{\boldsymbol{T}}\, \boldsymbol{p} = \boldsymbol{\delta v}^{\boldsymbol{T}}\, \boldsymbol{w} \qquad (2 - 46)$$

Equation (2 - 45) gives $\delta \boldsymbol{v} = \boldsymbol{a}_{\boldsymbol{g}}\, \boldsymbol{\delta u}$, then

$$\boldsymbol{\delta u}^{\boldsymbol{T}}\, \boldsymbol{p} = \boldsymbol{\delta v}^{\boldsymbol{T}}\, \boldsymbol{w} = \boldsymbol{\delta u}^{\boldsymbol{T}}\, \boldsymbol{a}_g{}^{\boldsymbol{T}}\, \boldsymbol{w} \quad \rightarrow \quad \boldsymbol{\delta u}^{\boldsymbol{T}}\, \left(\boldsymbol{p} - \boldsymbol{a}_g{}^{\boldsymbol{T}}\, \boldsymbol{w}\right) = \boldsymbol{0} \qquad (2 - 47)$$

If Equation (2 - 47) holds true for any possible virtual displacement $\boldsymbol{\delta u}$, then $\left(\boldsymbol{p} - \boldsymbol{a}_g{}^{\boldsymbol{T}}\, \boldsymbol{w}\right) = \boldsymbol{0}$ is true. Comparing with Equation (2 - 44), the equilibrium Equation (2 - 47) demonstrates that the equilibrium transformation matrix $\boldsymbol{b}_e$ is equal to the transpose of the displacement-deformation compatibility matrix $\boldsymbol{a}_g$, i.e.,

$$\boldsymbol{b}_e = \boldsymbol{a}_g{}^{\boldsymbol{T}} \qquad (2 - 48)$$

Therefore, to transform the element force and displacement between different systems, only one of these matrices is required to be established, the other can be obtained through a transpose operation. In practice, if the forces transforms from the basic system (i.e., element end force $\boldsymbol{w}$) to the global coordinate system (i.e., element end force $\boldsymbol{p}$) by using equilibrium transformation matrix $\boldsymbol{p} = \boldsymbol{b}_e \boldsymbol{w}$, then the displacements corresponding to forces transforms by using the relationship $\boldsymbol{v} = \boldsymbol{b}_e{}^{\boldsymbol{T}}\, \boldsymbol{u}$.

A key step in the numerical algorithm for a nonlinear system is to determine the resisting forces and the element stiffness matrix for a given displacement during the iteration process. The

tangent stiffness matrix of the element, $\boldsymbol{k_t}^{el}$, is obtained as the partial derivative of the resisting forces $\boldsymbol{p}$ with respect to the displacements $\boldsymbol{u}$ in the global coordinate system

$$\boldsymbol{k_t}^{el} = \frac{\partial \boldsymbol{p}}{\partial \boldsymbol{u}} = \frac{\partial}{\partial u}(\boldsymbol{b_e w}) = \boldsymbol{b_e}\frac{\partial \boldsymbol{w}}{\partial \boldsymbol{v}}\frac{\partial \boldsymbol{v}}{\partial \boldsymbol{u}} = \boldsymbol{b_e k_t}^{\boldsymbol{m}}\boldsymbol{a_g} = \boldsymbol{b_e k_t}^{\boldsymbol{m}}\boldsymbol{b_e}^{\boldsymbol{T}} \qquad (2 - 49)$$

where $\boldsymbol{b_e} = \boldsymbol{a_g}^{\boldsymbol{T}}$ is the equilibrium transformation matrix under un-deformed configuration and it does not depend on the displacement $\boldsymbol{u}$; $\boldsymbol{k_t}^{\boldsymbol{m}} = \partial \boldsymbol{w}/\partial \boldsymbol{v}$ is the tangent stiffness of the basic element associated with the yielding of material (i.e., the material nonlinearity property). Details about $\partial \boldsymbol{w}/\partial \boldsymbol{v}$ will be discussed in the next section. The element force-deformation relation is established in the basic system without rigid-body mode.

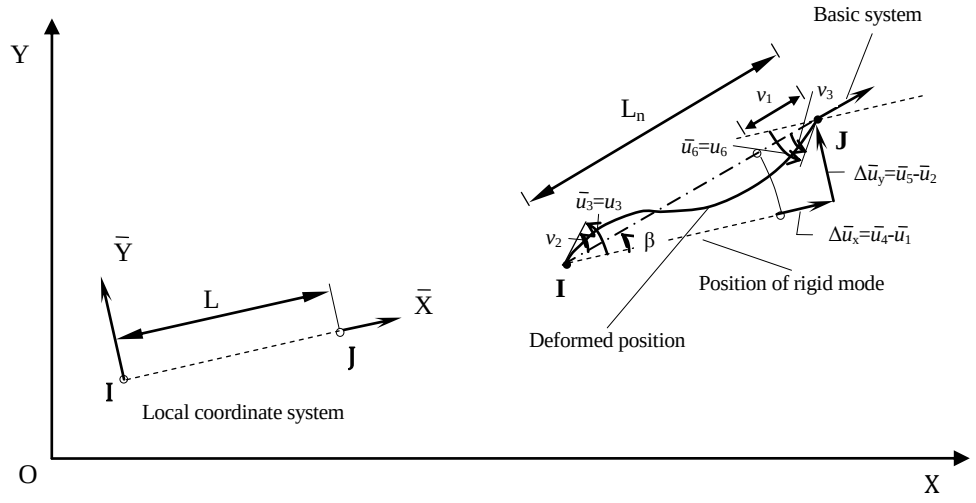

Figure 2-6 Deformed configuration of frame element

Equation (2 - 49) is derived on the assumption that the equilibrium equations are satisfied with respect to the un-deformed configuration. To account for instability effect, element equilibrium equations should be established based on the deformed configuration. As it is shown in Figure 2-6, since the rigid-body displacement of the element does not generate element deformation, the displacement-deformation compatibility relation can be expressed as

$$\begin{cases} v_1 = \dfrac{1}{2L}(L_n^2 - L^2) \\ v_2 = \overline{u}_3 - \beta \\ v_3 = \overline{u}_6 - \beta \end{cases} \tag{2 - 50}$$

where

$$L_n = \sqrt{(L + \Delta\overline{u}_x)^2 + (\Delta\overline{u}_y)^2} \tag{2 - 51}$$

$$\beta = \arctan\frac{\Delta\overline{u}_y}{L + \Delta\overline{u}_x} \quad , \quad \Delta\overline{u}_x = \overline{u}_4 - \overline{u}_1 \quad , \quad \Delta\overline{u}_y = \overline{u}_5 - \overline{u}_2 \tag{2 - 52}$$

The equilibrium equations of the free-body element are

$$\overline{\boldsymbol{p}} = \begin{pmatrix} \overline{p}_1 \\ \overline{p}_2 \\ \overline{p}_3 \\ \overline{p}_4 \\ \overline{p}_5 \\ \overline{p}_6 \end{pmatrix} = \begin{bmatrix} -(L + \Delta\overline{u}_x)/L_n & -\Delta\overline{u}_y/{L_n}^2 & -\Delta\overline{u}_y/{L_n}^2 \\ -\Delta\overline{u}_y/L_n & (L + \Delta\overline{u}_x)/{L_n}^2 & (L + \Delta\overline{u}_x)/{L_n}^2 \\ 0 & 1 & 0 \\ (L + \Delta\overline{u}_x)/L_n & \Delta\overline{u}_y/{L_n}^2 & \Delta\overline{u}_y/{L_n}^2 \\ \Delta\overline{u}_y/L & -(L + \Delta\overline{u}_x)/{L_n}^2 & -(L + \Delta\overline{u}_x)/{L_n}^2 \\ 0 & 0 & 1 \end{bmatrix} \begin{pmatrix} w_1 \\ w_2 \\ w_3 \end{pmatrix} = \boldsymbol{b}_u\, \boldsymbol{w} \tag{2 - 53}$$

Note that the equilibrium transformation matrix $\boldsymbol{b}_u$ depends on the end displacements. In practice, the terms of $\boldsymbol{b}_u$ are approximated by a Taylor series with consistent order of magnitude. The Equation (2 - 53) can be simplified to

$$\overline{\boldsymbol{p}} = \begin{pmatrix} \overline{p}_1 \\ \overline{p}_2 \\ \overline{p}_3 \\ \overline{p}_4 \\ \overline{p}_5 \\ \overline{p}_6 \end{pmatrix} = \begin{bmatrix} -1 & -\Delta\overline{u}_y/L^2 & -\Delta\overline{u}_y/L^2 \\ -\Delta\overline{u}_y/L & 1/L & 1/L \\ 0 & 1 & 0 \\ 1 & \Delta\overline{u}_y/L^2 & \Delta\overline{u}_y/L^2 \\ \Delta\overline{u}_y/L & -1/L & -1/L \\ 0 & 0 & 1 \end{bmatrix} \begin{pmatrix} w_1 \\ w_2 \\ w_3 \end{pmatrix} = \boldsymbol{b}_s\, \boldsymbol{w} \tag{2 - 54}$$

In building frameworks, the shear force $(w_2 + w_3) / L$ is usually small relative to the axial force w_1, and the transverse deformation $\Delta\overline{u}_y/L$ is always less than 0.1 (Filippou and Fenves 2004). Therefore, the so-called *p*-Δ transformation can be obtained with further simplification

$$\overline{\boldsymbol{p}} = \begin{pmatrix} \overline{p}_1 \\ \overline{p}_2 \\ \overline{p}_3 \\ \overline{p}_4 \\ \overline{p}_5 \\ \overline{p}_6 \end{pmatrix} = \begin{bmatrix} -1 & 0 & 0 \\ -\Delta\overline{u}_y/L & 1/L & 1/L \\ 0 & 1 & 0 \\ 1 & 0 & 0 \\ \Delta\overline{u}_y/L & -1/L & -1/L \\ 0 & 0 & 1 \end{bmatrix} \begin{pmatrix} w_1 \\ w_2 \\ w_3 \end{pmatrix} = \boldsymbol{b}_{p\Delta}\, \boldsymbol{w} \qquad (2 - 55)$$

Then, the rotation transformation matrix $\boldsymbol{b_r}$ is used to transform $\overline{\boldsymbol{p}}$ to the global coordinate system.

$$\boldsymbol{p} = \boldsymbol{b_r}\, \overline{\boldsymbol{p}} = \boldsymbol{b_r}\, \boldsymbol{b}_{p\Delta} \boldsymbol{w} \qquad (2 - 56)$$

The tangent stiffness matrix of the element under deformed equilibrium equations can be obtained,

$$\boldsymbol{k_t}^{el} = \frac{\partial \boldsymbol{p}}{\partial \boldsymbol{u}} = \frac{\partial}{\partial u}\,(\boldsymbol{b_r}\, \overline{\boldsymbol{p}}) = \boldsymbol{b_r} \frac{\partial \overline{\boldsymbol{p}}}{\partial \overline{\boldsymbol{u}}} \frac{\partial \overline{\boldsymbol{u}}}{\partial \boldsymbol{u}} = \boldsymbol{b_r} \frac{\partial \overline{\boldsymbol{p}}}{\partial \overline{\boldsymbol{u}}}\, \boldsymbol{a_r} = \boldsymbol{b_r} \frac{\partial \overline{\boldsymbol{p}}}{\partial \overline{\boldsymbol{u}}}\, \boldsymbol{b_r}^{\boldsymbol{T}} \qquad (2 - 57)$$

From Equation (2 - 53), the tangent stiffness matrix in the local system is found as

$$\overline{\boldsymbol{k_t}} = \frac{\partial \overline{\boldsymbol{p}}}{\partial \overline{\boldsymbol{u}}} = \frac{\partial}{\partial \overline{\boldsymbol{u}}}\,(\boldsymbol{b}_u\, \boldsymbol{w}) = \frac{\partial \boldsymbol{b}_u}{\partial \overline{\boldsymbol{u}}}\, \boldsymbol{w} + \boldsymbol{b}_u \frac{\partial \boldsymbol{w}}{\partial \boldsymbol{v}} \frac{\partial \boldsymbol{v}}{\partial \overline{\boldsymbol{u}}} \qquad (2 - 58)$$

When neglecting the difference between L_n and L in $\partial v_1/\partial \overline{\boldsymbol{u}}$, it can be shown that the condition $\partial \boldsymbol{v}/\partial \overline{\boldsymbol{u}} = \boldsymbol{b}_u{}^T$ holds.

Then, the tangent element stiffness matrix in the local system can be rewritten as

$$\overline{\boldsymbol{k}_t} = \overline{\boldsymbol{k}_g} + \overline{\boldsymbol{k}_m} = \frac{\partial \boldsymbol{b}_u}{\partial \overline{\boldsymbol{u}}}\, \boldsymbol{w} + \boldsymbol{b}_u \boldsymbol{k}_t{}^{\boldsymbol{m}} \boldsymbol{b}_u{}^{\boldsymbol{T}} \qquad (2 - 59)$$

where $\overline{\boldsymbol{k_g}} = \frac{\partial \boldsymbol{b}_u}{\partial \overline{\boldsymbol{u}}}\, \boldsymbol{w}$ and $\boldsymbol{k}_t{}^{\boldsymbol{m}} = \frac{\partial \boldsymbol{w}}{\partial \boldsymbol{v}}$. According to Equation (2 - 59), it is noted that the geometric transformation can be possibly separated from equilibrium transformation as long as the element force-deformation relation is established in the basic system.

Combining Equations (2 - 57) and (2 - 59) gives

$$\boldsymbol{k_t}^{el} = \boldsymbol{b_r}\left(\overline{\boldsymbol{k_g}} + \overline{\boldsymbol{k_m}}\right)\boldsymbol{b_r}^{\boldsymbol{T}} = \boldsymbol{b_r}\left(\frac{\partial \boldsymbol{b}_u}{\partial \overline{\boldsymbol{u}}}\,\boldsymbol{w} + \boldsymbol{b}_u \boldsymbol{k_t}^{\boldsymbol{m}} \boldsymbol{b}_u{}^{\boldsymbol{T}}\right)\boldsymbol{b_r}^{\boldsymbol{T}} \qquad (2 - 60)$$

To obtain the exact geometric transformation, the geometric stiffness $\overline{\boldsymbol{k_g}}$ needs to be determined. Using *p*-Δ transformation matrix to approximate the geometric stiffness $\overline{\boldsymbol{k_g}}$ is acceptable in earthquake engineering.

$$\overline{\boldsymbol{k_g}} = \overline{\boldsymbol{k}_{p\Delta}} = \frac{\partial \boldsymbol{b}_{p\Delta}}{\partial \overline{\boldsymbol{u}}}\,\boldsymbol{w} = \frac{w_1}{L}\begin{bmatrix} 0 & 0 & 0 & 0 & 0 & 0 \\ 0 & 1 & 0 & 0 & -1 & 0 \\ 0 & 0 & 0 & 0 & 0 & 0 \\ 0 & 0 & 0 & 0 & 0 & 0 \\ 0 & -1 & 0 & 0 & 1 & 0 \\ 0 & 0 & 0 & 0 & 0 & 0 \end{bmatrix} \qquad (2 - 61)$$

In practice, the linear compatibility matrix $\boldsymbol{b}_e$ is used for the approximation of $\boldsymbol{b}_u$ in the second term of Equation (2 - 60). With such simplifications, the simplified form of Equation (2 - 60) can be stated as

$$\boldsymbol{k_t}^{el} = \boldsymbol{b_r}\left(\overline{\boldsymbol{k_g}} + \overline{\boldsymbol{k_m}}\right)\boldsymbol{b_r}^{\boldsymbol{T}} = \boldsymbol{b_r}\overline{\boldsymbol{k}_{p\Delta}}\boldsymbol{b_r}^{\boldsymbol{T}} + \boldsymbol{b_r}\boldsymbol{b_e}\boldsymbol{k_t}^{\boldsymbol{m}}\boldsymbol{b_e}^{\boldsymbol{T}}\boldsymbol{b_r}^{\boldsymbol{T}} \qquad (2 - 62)$$

Using Equation (2 - 62), the material nonlinearity can be handled inside the basic system without regard for the kinematic and equilibrium transformations outside the basic system.

Material Nonlinear Analysis

In general, the yielding effects of structural members are simulated in accordance with the stress-strain relations of materials. The bilinear elastic-plastic stress-strain model is widely used in earthquake engineering analysis. It has been found that the elasto-perfectly-plastic stress-strain model (which neglects strain hardening) of structural steel material is generally conservative as long as strength is the primary concern (Bruneau et al 1998). However, the influence of strain hardening on plastic deformation calculations can be more significant. For uniaxial material analysis, lower strain hardening values will generally produce larger maximum plastic strains

and curvatures while higher values will translate into higher stresses and moments. In this research, the bilinear stress-strain relation of the Menegotto-Pinto model (Menegotto and Pinto 1973) with strain hardening (which is implemented in OpenSees analysis environment (OpenSees 2008)) is employed for the nonlinear time-history analysis.

To simulate material nonlinear property of a structural member, either "concentrated plasticity with elastic interior" or "distributed plasticity" models can be used through various approaches. A concentrated plasticity analysis is often an approximate method as concentrated plasticity models separate axial force-moment interaction from the member behaviour. However, the actual end force-deformation relation of a frame member results from the integration of the sectional response contribution along the element length. Thus, a calibration process against the "concentrated plasticity element" is usually required to reflect the actual response under idealized loading conditions. On the other hand, the gradual spread of yielding can be accurately captured in a distributed plasticity analysis since the stress state is being updated with respect to the integrated member sectional response. In this research, a distributed plasticity nonlinear beam-column element is used to represent steel frame members.

Based on simplified assumptions such as plane sections remain plane, elements are subjected to uniaxial bending, and shearing deformations are negligible, an efficient force-based nonlinear beam-column element can be formulated in a manner that the equilibrium between bending moment and axial force along the element can be strictly satisfied with regard to element deformations. Specifically, the force-based element modeling starts with the analysis of the pre-defined cross sections located along the element length. At each location, the element internal forces are determined with respect to the equilibrium equation of the element, while the corresponding sectional deformations at such locations are computed with respect to the defined cross-sectional stress-strain relationship. It is obvious that the computed sectional deformations should be compatible with the real deformations of the element with relation to the external forces. Often, the reasonably accurate prediction of the nonlinear response can be achieved through limited iterations. At the final step of the iterations, not only the internal forces but also the nonlinear deformation distributions along the element length are obtained with respect to the nonlinear stress-strain relationship of the structural material. Thus, the material nonlinear

property of the structural frame member can be directly defined in terms of the explicit relations between the section force resultants and deformations.

Force-Based Distributed Plasticity Nonlinear Beam-Column in OpenSees

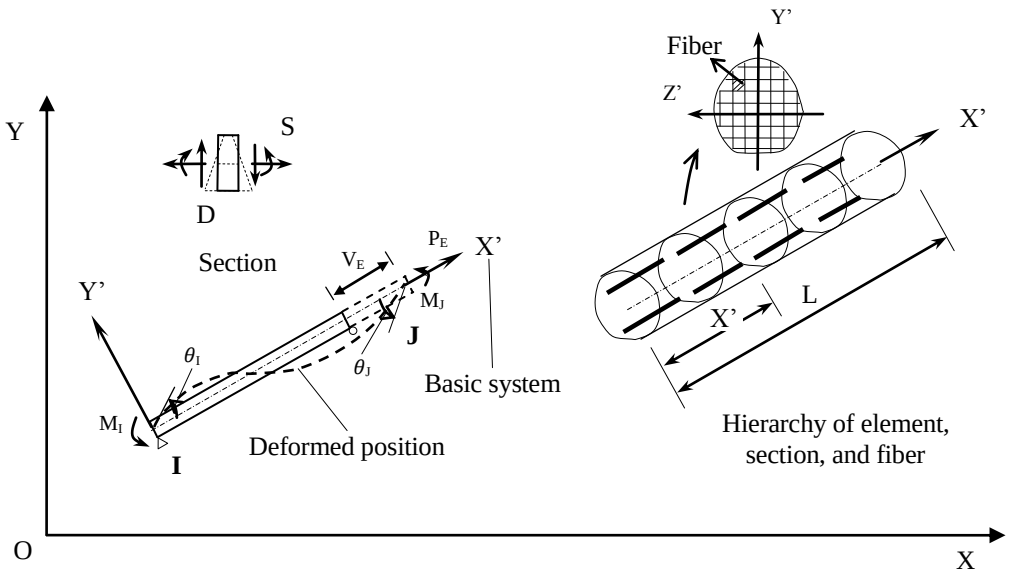

Figure 2-7 Basic (rotating) and global coordinate system (Neuenhofer and Filippou 1997)

Distributed plasticity of a beam-column member can be simulated either by displacement- or force-based formulations. Following the standard displacement-based approach, the transverse and axial displacements of a beam-column member are expressed as appropriate interpolation functions of the nodal displacements. To approximate the nonlinear displacement field in the displacement-based formulation, several elements are required along the length of a frame member to represent the distributed plastic behaviour if the axial force is large. On the other hand, the force-based beam-column element employs section forces interpolation functions to formulate element flexibility matrix with respect to the element nodal forces. The ability to maintain equilibrium within the element (even in the range of nonlinear response) makes it possible to use one force-based element to simulate the nonlinear behaviour of a frame member (Neuenhofer and Filippou 1997).

According to the corotational formulation (Crisfield, 1991), the element is formulated in the basic system without rigid body modes and the specific transformation is employed to transform the basic variables to the global system. The basic (rotating) and global coordinate systems of a

beam-column element are shown in Figure 2-7. The material nonlinearity within the basic system is represented by a discrete number of cross sections (which are located at the control points of the numerical integration algorithm along the length of the element). Moreover, these sections (i.e., 5 cross sections in Figure 2-7) can be further subdivided into fibres such that the nonlinear sectional response can be obtained through the integration of the fibre responses with respect to the given material constitutive relationship rather than a directly defined force-deformation relationship curve. For the two-dimensional elements, the element deformation vector $\boldsymbol{V}$, force vector $\boldsymbol{W} = W(\boldsymbol{V})$ and the corresponding section deformation vector $\boldsymbol{D}$, force vector $\boldsymbol{S} = S(\boldsymbol{D})$ are expressed as

Element deformation vector

$$\boldsymbol{V} = \left\{ v_E \;\; \theta_I \;\; \theta_J \right\}^T \tag{2 - 63}$$

Element force vector

$$\boldsymbol{W} = \left\{ P_E \; M_I \;\; M_J \right\}^T \tag{2 - 64}$$

Section deformation vector

$$\boldsymbol{D} = \{\bar{\varepsilon}(x) \;\; \kappa_z(x)\}^T \tag{2 - 65}$$

Section force vector

$$\boldsymbol{S} = \{N(x) \;\; M_z(x)\}^T \tag{2 - 66}$$

where $\bar{\varepsilon}(x), \kappa_z(x)$ are the axial strain and moment curvature, respectively; $N(x)\; M_z(x)$ are the sectional axial force and bending moment, respectively.

In the force-based method the force interpolation functions are employed to approximate the force field within the element. The relation between the nodal force vector and internal section force vector is described as

$$\boldsymbol{S}(x) = \boldsymbol{a}(x) \cdot \boldsymbol{W} \tag{2 - 67}$$

where $\boldsymbol{a}(x)$ contains the force interpolation functions. Those interpolation functions can be readily obtained from the equilibrium of axial forces and bending moments within the element. For the two-dimensional elements shown in Figure 2-7, the interpolation function matrix is expressed as

$$\boldsymbol{a}(x) = \begin{bmatrix} 1 & 0 & 0 \\ 0 & \frac{x}{L} - 1 & \frac{x}{L} \end{bmatrix} \tag{2 - 68}$$

The compatibility relationship between the section and element deformations can be determined by employing the principle of virtual force,

$$\boldsymbol{V} = \int_0^l \boldsymbol{a}^T \boldsymbol{D} \, dx \tag{2 - 69}$$

In the force-based Finite Element Analysis, the element flexibility matrix needs to be formulated in advance. The linearization of deformation or displacement with respect to the corresponding force yields the flexibility matrix. The section flexibility matrix $\boldsymbol{f_s}$ and element flexibility matrix $\boldsymbol{F}$ can be expressed, respectively, as

$$\boldsymbol{f_s} = \partial \boldsymbol{D} / \partial \boldsymbol{S} \tag{2 - 70}$$

$$\boldsymbol{F} = \partial \boldsymbol{V} / \partial \boldsymbol{W} \tag{2 - 71}$$

Substituting equations (2 - 67) and (2 - 70) into equation (2 - 71) yields the element flexibility matrix

$$\boldsymbol{F} = \frac{\partial \boldsymbol{V}}{\partial \boldsymbol{W}} = \frac{\partial \boldsymbol{V}}{\partial \boldsymbol{D}} \cdot \frac{\partial \boldsymbol{D}}{\partial \boldsymbol{S}} \cdot \frac{\partial \boldsymbol{S}}{\partial \boldsymbol{W}} = \int_0^l \boldsymbol{a}^T \boldsymbol{f}_s \boldsymbol{a} \, dx \tag{2 - 72}$$

While the control sections are subdivided into fibres, the strain distribution in a section x can be determined based on the assumption that the plane section remains plane and normal to the longitudinal axis. Then the corresponding stresses and tangent modulus with respect to the strain values at each fibre are computed according to the material constitutive relation. Subsequently, the section stiffness $\boldsymbol{k_s(x)}$ and resisting force $\boldsymbol{S(x)}$ are evaluated through a numerical integration scheme, respectively. The section stiffness is then inverted to obtain the flexibility matrix $\boldsymbol{f_s(x)}$. Then, the element flexibility matrix $\boldsymbol{F}$ is computed from Equation (2 - 72).

As shown in the element formulation procedure, the advantage of the force-based element is that it always comes up with force interpolation functions which satisfy equilibrium exactly. However, the implementation of the force-based element model in a direct-stiffness-method-based nonlinear analysis program is not straightforward (Neuenhofer and Filippou 1997; Scott et al 2008). When iterative numerical methods (i.e., the procedure from Equation (2 - 34) to Equation (2 - 39)) are employed to solve the nonlinear system differential equations, the element stiffness matrix as well as the force state at each iteration step need to be determined. Although the element stiffness matrix can be obtained by inverting the element flexibility matrix $\boldsymbol{F}$, there are no direct functions to compute the element generalized resisting forces (e.g., the element forces corresponding to $\Delta\{f\}^{(1)}$ in Equation (2 - 35)) with respect to the section force vector $\boldsymbol{S}$.

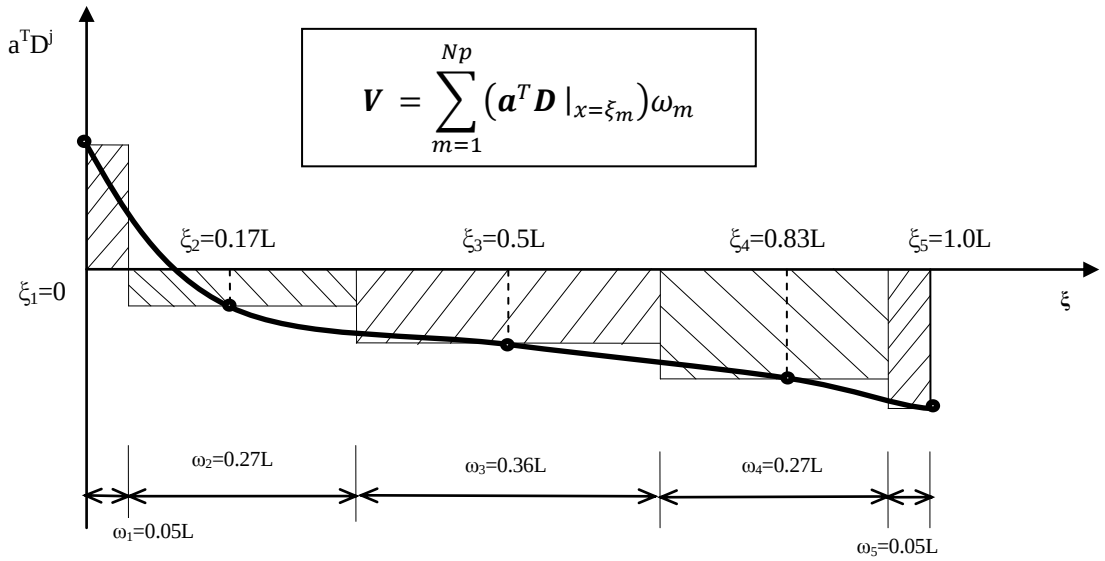

Figure 2-8 Evaluation of force-based element compatibility relation (Scott et al 2006)

In practice, an iterative algorithm at the element level (Spacone et al 1996) is employed to approach the element force state with respect to the updated deformation state. The detail of the procedure is described in Appendix 2.A. It has been shown (Neuenhofer and Filippou 1998) that by using the force-based nonlinear element, only one element is required to represent the material nonlinearity of a frame member. Comparing to the displacement-based nonlinear elements where several elements are needed to approximate the nonlinear displacement field, the degrees of freedom of the structural model can be substantially reduced. Therefore, the potential computational saving is obvious.

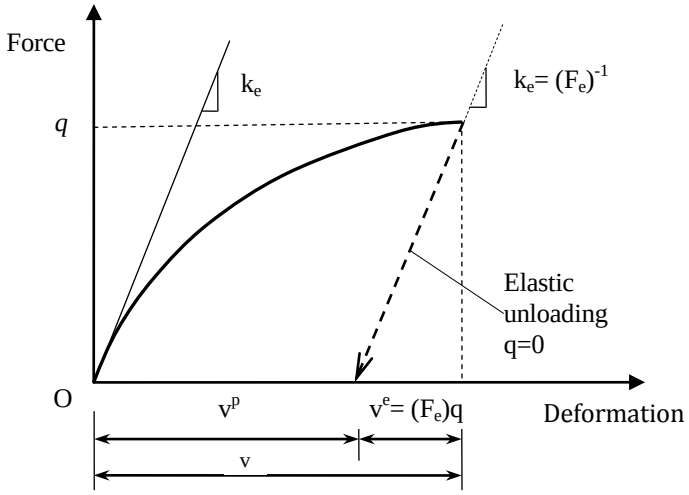

Figure 2-9 Plastic rotation in beam-column

To restore the element deformation from the section deformations, the Gauss-Lobatto quadrature numerical method is employed to evaluate the integral of Equation (2 - 69). The numerical procedure can be visually illustrated in Figure 2-8, where ξ and ω represent locations and associated weights, respectively, of the N_p integration points over the element length. The method is equivalent to treating $\boldsymbol{a}^T\boldsymbol{D}$ as constant over the length ω_m for the element deformation evaluation. The relation between the element deformation $\boldsymbol{V}$ and the convergenced section deformation $\boldsymbol{D}$ can be numerically expressed as

$$\boldsymbol{V} = \sum_{m=1}^{Np} \left(\boldsymbol{a}^T\boldsymbol{D}\,|_{x=\xi_m}\right)\omega_m \qquad (2 - 73)$$

To assess the plastic rotation of a beam-column, the element deformation is decomposed into elastic and plastic components. As shown in Figure 2-9, the plastic deformation can be computed (Scott et al 2006) as

$$\boldsymbol{V}^{p} = \sum_{m=1}^{Np} \left(\boldsymbol{a}^{T} \boldsymbol{D} \; \Big|_{x=\xi_m} \right) \omega_m - \boldsymbol{F_e W} \qquad (2 - 74)$$

2.2.3 Input Ground Motion Time Histories

The inelastic behaviour of steel building frameworks depends not only on the dynamic characteristics of the SFRSs, but also upon the properties of the input ground motion time histories. For a nonlinear time-history analysis, the ground motion histories can be obtained by scaling and/or modifying real records from past earthquakes or by employing suitable artificial records. Tremblay (2001) showed that simulated time histories and real ground motion time histories are functionally equivalent for both linear and nonlinear analyses.

The adopted ground motion time histories for conducting a nonlinear time-history analysis should be consistent with the magnitude, fault distance, and source mechanism where the building structure is to be built. Furthermore, due to the sensitivity of structural response to the properties of a ground motion, a nonlinear time-history analysis using only one ground motion time history input may not truly represent the actual seismic responses. To account for this uncertainty in earthquake loading, an assembly of (e.g., at least three by NBCC 2010) different ground motion time histories are required for one nonlinear time history analysis. When a sufficient number of ground motions are included in a nonlinear time history analysis (e.g., 7 by FEMA-450 (2004a)), the mean values of structural responses are used as the performance parameters for design purposes. In this research, mean values of the structural responses such as seismic input energy, hysteretic energy, and deformations are used in the design examples.

To serve the purpose of this research, an assembly of recorded “real time histories” selected from the PEER Strong Ground Motion Database (PEER 2008) will be used. The adopted ground motion time histories will be scaled to simulate the design earthquake hazard level. In particular,

as a design earthquake level is typically represented by a design spectrum, the adopted ground motions will be scaled such that their response spectrum coordinates should equal to or exceed the corresponding design spectrum value throughout the period range of interest. The details of how to scale the selected ground motion time histories to be compatible with a design spectrum are presented in the design examples in Chapter 4.

2.3 Comparison of Seismic Energy Input

In this section, an educational program called NONLIN (Charney 2004) has been employed to validate the proposed numerical method for seismic energy computation (which is described in Section 2.1.2).

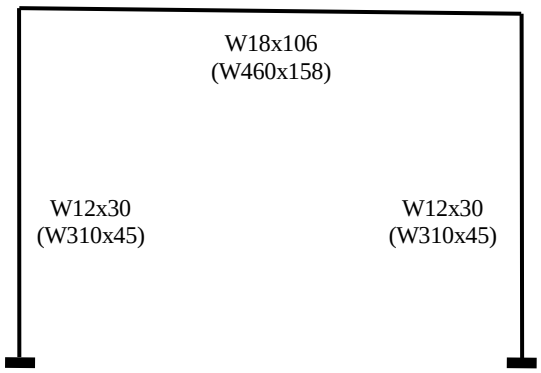

Figure 2-10 Steel portal frame for computation of seismic energy input

As it is shown in Figure 2-10, a feasible design of the steel portal frame is subjected to a given earthquake ground motion (the details of the design problem are shown in Appendix 3.B). Herein, the educational software NONLIN (Charney 2004) serves as the baseline for comparison. Since NONLIN is only applicable for the dynamic analysis of SDOF systems (i.e., only one mass is considered by NONLIN), the analytical model for comparison needs to be calibrated. For this reason, the design with the smallest column structural steel section size, W12x30 (W310x45), and the largest structural steel beam section size, W18x106 (W460x158), in which the difference between the lateral displacements of the two mass points (i.e., the two beam-to-column joints) is the minimum among the total 256 trial designs so that the structural response can be estimated by using a SDOF model, is employed for comparison.

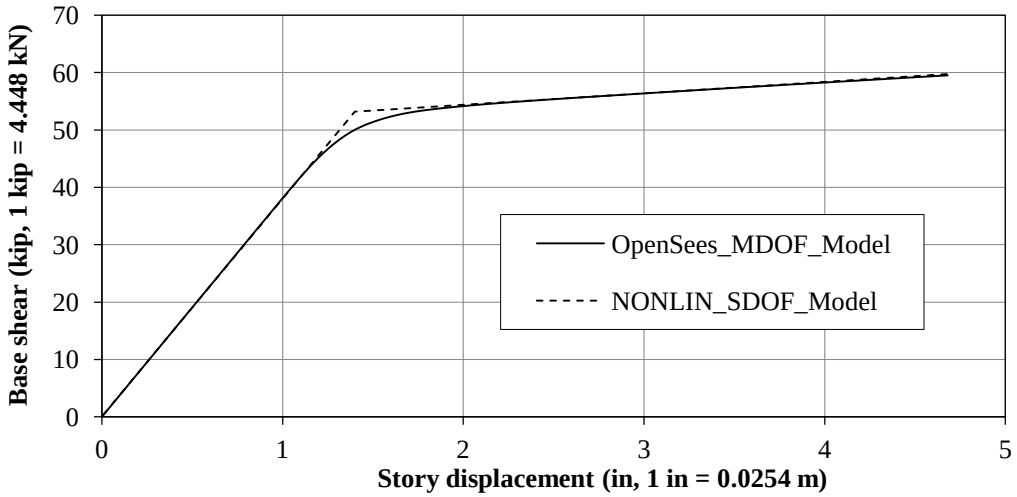

Figure 2-11 Push-over curve (base shear – story displacement) for model calibration

First, an equivalent SDOF model of the portal frame needs to be established for NONLIN. The lateral stiffness and strength parameters of the SDOF model are obtained from the push-over curve of the steel portal frame. The solid-line shown in Figure 2-11 illustrates that the portal frame is pushed to the lateral displacement of 3% story height (0.03x12x13=4.68 in (0.118 m)). The bilinear dashed-line is used to approximate the lateral force vs. deflection of the SDOF model. Thus, the parameters for the SDOF model are as follows: yield strength F_y=53.4 kip (237 kN), initial stiffness k_1= 38 kip/in (6654 kN/m), and post yield stiffness k_2=2 kip/in (350 kN/m).

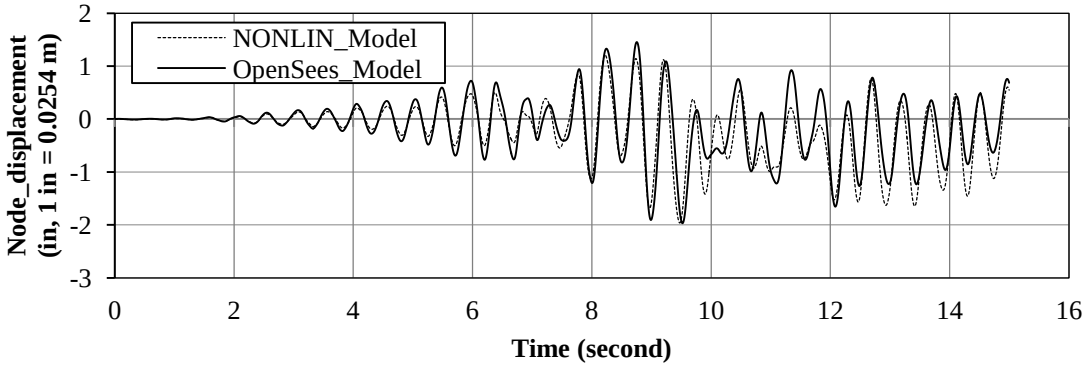

Figure 2-12 Comparison of lateral displacement response histories

The lateral displacement response histories of the SDOF and MDOF models are compared in Figure 2-12, where the curves are obtained by adopting the ground motion record of "Imperial Valley 10/15/79 2316, El Centro array #12" (PEER 2008) with a scale factor of 3.0. It can be

seen that the nonlinear response of the SDOF model of NONLIN agrees well with the response of the MDOF model of OpenSees.

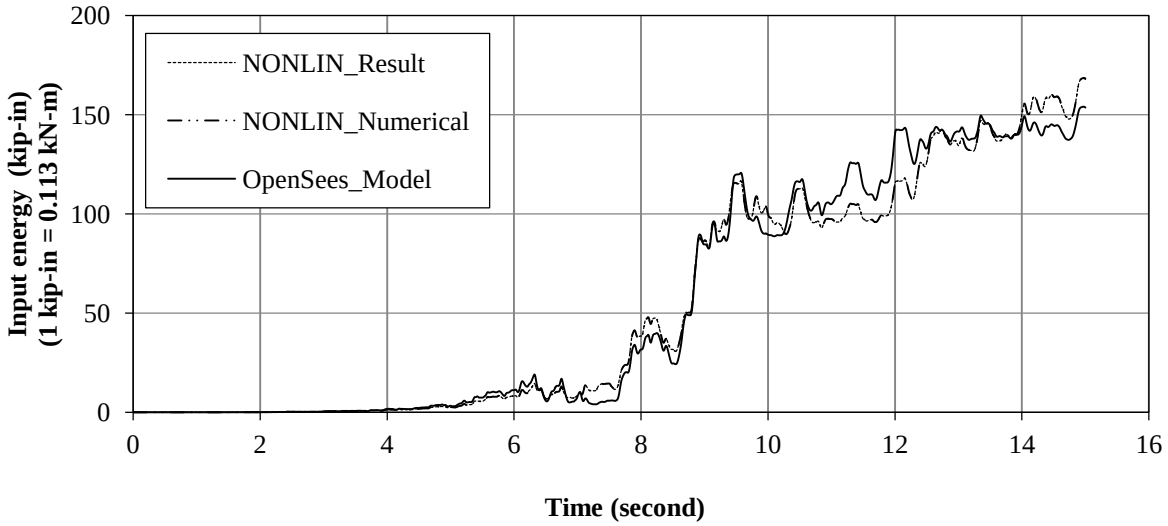

Figure 2-13 Seismic energy input response history

Figure 2-13 shows the comparison of seismic input energy histories obtained by various methods. The history curves "NONLIN_Numerical" and "OpenSees_Model" are obtained using the proposed procedure in Section 2.1.2 (SDOF model in NONLIN and MDOF model in OpenSees). The NONLIN program uses a step-by-step method to solve the nonlinear equations of motion. The history curve "NONLIN_Result" is obtained by the embedded method in NONLIN program. Indeed, all the curves show the same trend of the seismic input energy during the earthquake ground motion. The curve of "NONLIN_Numerical" matches the curve of "NONLIN_Results" perfectly. Some small differences can be observed between the energy history curves of "NONLIN_Numerical" and "OpenSees_Model", which is derived from the estimation errors of the lateral displacement response histories (see Figure 2-12) of the two models. It can be concluded from this numerical test that the proposed method for seismic energy computation (Section 2.1.2) is valid.

Chapter 3

Design Optimization Problem Formulation

The task of the seismic design of steel building frameworks is to proportion the member sizes of a SFRS of a steel building as per the governing seismic provisions and economical requirements. Conventionally, the design process involves repetitive application of structural analysis with respect to the iterative changes in member sizes. Often, the trial-and-error design cycle could be repeated quite a number of times. Specifically, the reanalysis-redesign cycle may lead to an uncontrollable decision-making state when a nonlinear time-history analysis is employed as the evaluating tool since it is much more difficult to predict the nonlinear structural response beforehand with regard to the changes in member sizes. To overcome the computational difficulties, efficient and reliable strategies are needed to facilitate the tedious analysis-design procedure.

On the other hand, the conventional trial-and-error evolving design procedure can be conceptually viewed as an optimization process. It is intuitive that an efficient and reliable design methodology can be developed with the assistance of optimization techniques. Indeed, devotion to providing optimization techniques in design of steel frameworks to achieve economical structures has gained wide acceptance in academic community over years. This research will extend optimization applications to develop an automatic capacity design procedure for steel building frameworks by using nonlinear time-history analysis.

In this research, the optimal design solutions are sets of cross-section sizes of commercially available steel shapes. In its general mathematical form, a multi-objective design optimization problem can be expressed as

$$\text{Minimize} \quad \mathbf{OBJ} = \{OBJ_1(\boldsymbol{X}), OBJ_2(\boldsymbol{X}) \ldots . OBJ_n(\boldsymbol{X})\} \tag{3 - 1}$$

$$\text{Subject to} \qquad g_l(\boldsymbol{X}) \leq g_l{}^u \ \ (l = 1,2, \ldots \ n_c) \tag{3 - 2}$$

$$x_j{}^l \leq x_j \leq x_j{}^u \quad (j = 1,2, \ldots n_x) \qquad (3 - 3)$$

$$x_j \in \boldsymbol{X}_j \qquad (j = 1,2, \ldots n_x) \qquad (3 - 4)$$

where: **OBJ** is a set of objective functions; $\boldsymbol{X}$ is the vector of n_x design variables that are required to be found in order to minimize the objective functions; $g_l(\boldsymbol{X})$ is the l^{th} constraint function bounded by its upper limit, $g_l{}^u$; $x_j{}^l$ and $x_j{}^u$ are the lower bound and upper bound for design variable x_j respectively. For discrete variables, the variable x_j should be selected from among a predetermined set of $\boldsymbol{X_j}$ of discrete sizes.

Specifically, the details of the proposed energy-based optimal design methodology, i.e., the formulations of design objective functions and the design constraints, are described in the following sections.

3.1 Design Objective Functions

An objective function, also known as a cost or performance criterion which is used as a measure of effectiveness of a design, is expressed in terms of design variables and serves as a decision motivator. Generally, one design with a preferable objective value compared to another can be deemed as a "better design" if all the design constraints are satisfied. For seismic design of steel building frameworks, the proposed objective functions (along with the design constraints) must represent the structural behaviour regarding to the design ground motions and reflect the seismic design philosophy. The measures which are most interesting to structural engineers should be included in the optimization framework. In this research, three design objectives are considered: 1) the minimum structural cost of SFRS; 2) the minimum seismic input energy imparted to the SFRS; and 3) the maximum hysteretic energy dissipation of the fuse members of SFRS.

3.1.1 Minimum Cost of SFRS

Cost-saving is usually the pursuit of every structural design. Herein, minimum structural cost is adopted, as in many other optimization problems. Under the assumption that member cost is in proportion to its weight, the least-cost design can be interpreted as the least-weight design of the

structure; and the structural cost objective OBJ_1 is thus expressed by the following *minimization* function:

$$OBJ_1(\boldsymbol{X}) = min\left(\sum \rho\, L_k\, A_k\right) \qquad (k = 1,2,\ldots\, n_e) \qquad (3 - 5)$$

where: $\boldsymbol{X}$ is the vector of design cross-section size variables; ρ is the material mass density; L_k and A_k are the length and cross-sectional area of the k^{th} member, respectively; and n_e is the number of the structural members in the SFRS.

3.1.2 Minimum Seismic Input Energy

The structural demands on a SFRS in terms of stiffness, strength, and energy dissipation are interrelated with the supplies while the structure responds to earthquake ground motions. The potential seismic damage depends on the severity of earthquake ground motions (or peak ground acceleration), duration of earthquakes and the frequency contents of the ground excitations. Seismic energy input quantities, rather than a single peak force or displacement response, account for the duration and dynamic effects of seismic loading. The smaller the amount of energy imparted into a SFRS is, the smaller the amount of consequential damage will be and the greater the chance the structure will survive. It is desirable to design building structures with the minimum damage potential with respect to earthquake ground motions; i.e., the objective OBJ_2 is expressed by the following *minimization* function:

$$OBJ_2(X) = min\left(\hat{E}_i\right) \qquad (3 - 6)$$

where $\hat{E}_i$ is the mean value of the seismic input energies for n_g ground motions considered in the nonlinear time-history analysis.

3.1.3 Maximum Hysteretic Energy Dissipation of Fuse Members

It has been widely accepted that (FEMA 2004b; NRCC 2006) a well performing SFRS should be able to dissipate a large amount of seismic energy through its stable, non-degrading, predictable cyclic inelastic behaviour. Indeed, the analysis of hysteretic energy dissipation mechanisms forms the basis for seismic design. To dissipate seismic energy efficiently and safely, the

capacity design principle is explicitly required in seismic provisions. Since fuse members are detailed to stably sustain large cyclic inelastic deformations, a large amount of seismic input energy can be dissipated through fuse members without significant impact on the integrity of a SFRS. From the viewpoint of energy, it is reasonable to say that the larger the amount of energy dissipated through fuse members, the greater the chance the structure will survive. Thus, the hysteretic energy dissipation objective which reflects the capacity design philosophy is expressed by the following *maximization* function:

$$OBJ_3(\boldsymbol{X}) = max(\hat{\beta}) \qquad (3 - 7)$$

where $\hat{\beta}$ is the mean value of $\beta_j = \left(E_{h\_fuse}/E_h\right)_j$, $\left(j = 1,2, \ldots n_g\right)$, the hysteretic energy dissipation ratio of fuse members under n_g ground motions; in which E_{h_fuse} is the hysteretic energy of fuse members and E_h is the total hysteretic energy of the SFRS (it is shown in the numerical examples that this objective function effectively serves to confine plastic deformation to the fuse members of a SFRS).

3.2 Design Constraints

In general, the space of design solutions is divided into a feasible domain and an infeasible domain based on the satisfaction of the imposed constraints. Following an optimization procedure, while the objective functions are improved, a feasible design has to satisfy a host of stress, displacement, buckling, fabrication and functional requirements.

The constraints that represent limitations to the performance of a system are termed performance constraints. On the other hand, the constraints imposed on the availability, fabrication or other physical limitations are called side constraints. For this research, the specific constraint functions are described as follows.

3.2.1 Performance Constraints

All feasible designs are required to resist force and deformation actions within the acceptance criteria stated in a governing code or specification. To be consistent with current seismic design practice, the research considers the seismic performances of both individual structural members

and the whole structural system as the primary design constraints for evaluating the feasibility of a candidate design. At the member level, it is required that a member is able to undergo a plastic deformation without any premature strength failure. At the system level, the integrity of a SFRS must be maintained to support gravity loads, and the general damage to non-structural elements should also be restricted within an acceptable limit.

For the design of frame members, conventional elastic-analysis-based design methods always require explicit member strength checking, in which the strength equations account for material yielding and P-delta effects (such as CSA-S16-09). For the Nonlinear Time-History Analysis (OpenSees 2008) employed in this research, steel members are modeled such that the stress states of the considered cross-sections are directly determined in accordance with the experimentally-proven nonlinear constitutive relationship. Furthermore, the destabilizing effects of gravity loads, i.e., P-delta effects, are directly included in the analysis procedure. Consequently, the element strength checks are implicitly accounted for in the analysis procedure. Therefore, there is no further need to include explicit forms of strength constraints in the formulation of the proposed optimal design problem. As a result, the acceptance criteria for the steel frame members are only expressed in terms of inelastic deformation limits.

Plastic Deformation Constraints on Fuse Members

Fuse members are designed to experience large inelastic deformations. A plastic deformation constraint on fuse members is necessary in order to achieve a stable and undegraded plastic behaviour, i.e.,

$$\hat{\theta}_l \leq \theta_{l,0} \qquad \left(l = 1,2,\dots\ n_f\right) \tag{3 - 8}$$

where: $\hat{\theta}_l$ is the mean value of plastic deformation demand for the l^{th} fuse member under n_g ground motion time histories; and $\theta_{l,0}$ is the corresponding allowable plastic deformation limit capacity. For the beams in a moment resisting frame, $\hat{\theta}_l$ is the member-end plastic-hinge rotation. For the shear links in an eccentrically braced frame, $\hat{\theta}_l$ is the shear link plastic rotation. For the diagonal braces in a concentrically braced frame, $\hat{\theta}_l$ is the plastic axial deformation of the braces.

Plastic Deformation Constraints on Non-Fuse Members

For the non-fuse members in a SFRS, their plastic deformations usually need to be strictly restricted. In its generic form, the deformation constraints on non-fuse members of SFRSs can be expressed as

$$\hat{\varphi}_m \leq \varphi_{m,0} \qquad (m = 1,2, \ldots n_{nf}) \tag{3 - 9}$$

where: $\hat{\varphi}_m$ is the mean value of the plastic deformation demand of the m^{th} non-fuse member; and $\varphi_{m,0}$ is the corresponding allowable plastic deformation. If no plastic deformation is permitted, the value of $\varphi_{m,0}$ should be set to a very small number but non-zero to facilitate the numerical instabilities in the design algorithm.

Plastic Deformation Capacities of Frame Members

The typical moment versus deformation curve of a steel member is illustrated in Figure 3-1. The curve is composed of an elastic range, points O to A on the curve, and an inelastic range, points A to C. The inelastic portion of the curve includes a strain hardening range, points A to B, and a strength degraded range, points B to C. In general, the deformation acceptance criterion for a ductile behaviour of a member should be within the ranges between O to B. Steel beams, having a compact cross section, always exhibit a large plastic range without significant moment capacity degradation. The failure of such a beam is characterised by the exhaust of its plastic deformation capacity. For a beam-column, its plastic deformation capacity is greatly influenced by the existence of an axial force. In general, the greater the axial force is, the less its plastic bending deformation capacity will be. For example, if the axial force of a beam-column is equal to its pure axial force resistance (i.e., the capacity of the member under axial force only), then its plastic bending deformation capacity (the range AB) is zero.

The plastic rotation capacities of shear links in EBFs are taken as 0.08 radians in the Canadian Standard CSA-S16-09. The plastic deformation capacity of a beam-column, $\theta_{l,0}$ or $\varphi_{m,0}$, is dependent upon both its axial force and sectional slenderness ratio. According to the ASCE/SEI standard 41-06 (ASCE 2007), (see Appendix 3.A for details) the plastic rotation capacity of a ductile frame member, whose axial force ratio is less than 0.2, is at least $3.0\theta_y$, where θ_y is the

yield rotation and is computed as $\theta_y = (ZF_{ye}L)/(6EI)$. The plastic rotation capacity is at least equal to $0.8\theta_y$ if the member has a greater axial force. The actual chosen values for the plastic limits in Equations (3 - 8) and (3 - 9) must reflect capacity design philosophy in addition to satisfying the deformation capacity requirement.

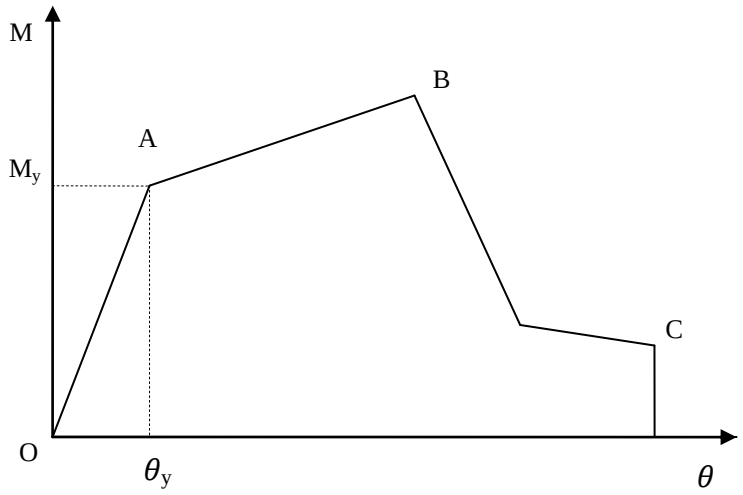

Figure 3-1Typical bending moment versus deformation curve

It should be noted that the recommended acceptance criteria in Appendix 3.A correspond to Collapse Prevention level. If the Immediate Occupancy performance level is required, the acceptance criteria will be much more stringent (ASCE 2007). For example, in general, the allowable plastic rotations under the Immediate Occupancy level are less than $1.0\theta_y$. Practically, such a small plastic deformation level may be interpreted as non-detrimental plastification allowed in non-fuse members for enforcing the capacity design requirements.

Table 3-1 Plastic rotation limits of structural members

Type of SFRS	Fuse Members		Non-Fuse Members	
MRF	Beams	8 θ_y / 3 θ_y	Columns	2.0 θ_y / 0.5 θ_y
EBF	Shear Link	0.08 radians	Beams	0.6 θ_y
			Columns	0.5 θ_y
			Braces	0.5 θ_y

Table 3-1 gives the plastic deformation acceptance criteria adopted by the design examples for MRFs in Chapter 4 and EBFs in Chapter 5. For MRFs, the allowable plastic rotation for columns is taken as $2.0\theta_y$ to $0.5\theta_y$ depending on the relative magnitude of the column axial force. For

EBFs, $0.5\theta_y$ and $0.6\theta_y$ are adopted as the allowed non-detrimental plastic deformations for non-fuse beam-column and beam members, respectively.

Deformation Constraints on SFRS

Stability of seismic force resisting systems is another essential issue for building structures to survive a strong earthquake ground motion. To this end, controlling drift is still commonly employed as a practical method to indirectly address the overall stability problem in spite of P-delta effects being already considered in structural analysis procedures. It has been proven that the earthquake damage to non-structural elements can also be restricted through drift controls (FEMA 2004b).

Specifically, a SFRS is deemed to be lateral deformation acceptable if it satisfies the following constraints on the inter-storey drifts,

$$\hat{\delta}_s \leq \delta_0 \qquad (s = 1,2, \dots n_s) \tag{3 - 10}$$

where: $\hat{\delta}_s$ is the mean value of the s^{th} inter-storey drift for n_g ground motions; n_s is the number of stories; δ_0 are the specified allowable values for drift.

3.2.2 Side Constraints

General speaking, it is desirable to use commercially available standard sections to proportion steel frameworks. Furthermore, the local buckling failure of structural members should be avoided to ensure the development of stable, non-degrading hysteretic behaviour. For this research, the frame members are selected from among the compact sections if the development of plastic hinges is anticipated. At present, the side constraints imposed on the optimization problem can be expressed as

$$x_j \in \boldsymbol{C_j} \qquad (j = 1,2, \dots n_x) \tag{3 - 11}$$

where: $\boldsymbol{C_j}$ is a set of discrete steel cross-sections (e.g., from AISC 2005b or CISC 2010) for member *j*.

3.3 Optimization Formulation and Algorithm

From the forgoing, the multi-objective design optimization problem is formulated as follows:

$$\text{Minimize:} \quad \mathbf{OBJ} = \{f_1 \quad f_2 \quad f_3\}^T \tag{3 - 12}$$

$$\text{Subject to:} \quad \hat{\theta}_l \leq \theta_{l,0} \qquad (l = 1,2, \ldots n_f) \tag{3 - 8}$$

$$\hat{\varphi}_m \leq \varphi_{m,0} \quad (m = 1,2, \ldots n_{nf}) \tag{3 - 9}$$

$$\hat{\delta}_s \leq \delta_0 \qquad (s = 1,2, \ldots n_s) \tag{3 - 10}$$

$$x_j \in \boldsymbol{C_j} \qquad (j = 1,2, \ldots n_x) \tag{3 - 11}$$

where the objective vector **OBJ** consists of three objective criteria. The objective functions in Equation (3 - 12) are normalized in order to facilitate numerical realization. The cost objective is normalized as $f_1 = (\sum \rho L_k A_k)/(\sum \rho L_k A_{kmax})$, where A_{kmax} is the largest cross section in set $\mathbf{C}_k$ or among the current group of evaluated designs. The input energy objective defined in Equation (3 - 6) is normalized as $f_2 = \hat{E}_i/\hat{E}_{imax}$, where $\hat{E}_{imax}$ is the maximum input energy among the current group or population of evaluated designs. The third objective on hysteretic energy in Equation (3 - 7) is transformed into a minimization criterion by rewriting it as $f_3 = (1 - \hat{\beta})$. Thus, all the three normalized objectives, f_1 to f_3, have a value ranging from 0 to 1.

For multi-objective optimization problems, it is common that there is no unique design that could achieve all of the optimal criteria simultaneously. As the objectives generally conflict with each other, it is expected that a set of optimal solutions with a varying degree of the objective values are available. Such optimal solutions are known as 'Pareto-optimal' since none is dominated by other feasible solutions for all of the objectives. Therefore, the important task for solving a multi-objective optimization problem is to find as many Pareto-optimal solutions as possible (ideally, all the Pareto-optimal solutions would be found). Although only one solution is required in a real-world optimization problem, the knowledge of the optimal solutions can facilitate the trade off study between various objectives.

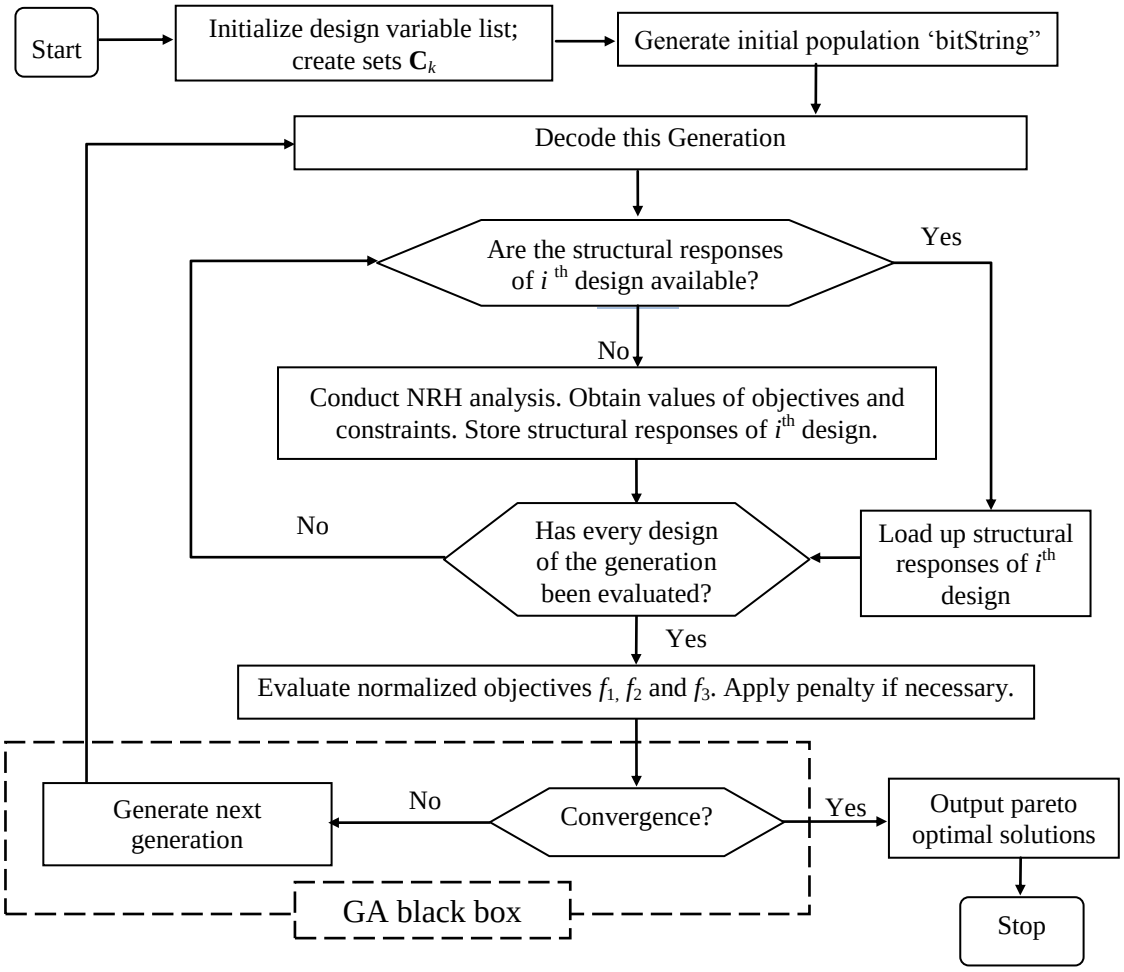

Figure 3-2 Flowchart of the proposed design procedure

Various optimization algorithms are available to solve a multi-objective design problems. A classical method is to transform a multi-objective optimization problem into a single-objective problem by introducing a weight vector for the multiple objectives. However, only a single optimal solution can be found each time when using this converted single-objective formulation. One has to use the algorithm many times in order to find a set of Pareto-optimal solutions through adjusting the user-defined weight vector.

For this research, no preference is given to any particular criterion. Thus, a weight vector is not employed. Instead, the Multi-objective Genetic Algorithm (MGA) based on the concept of domination (Deb 2001) is adopted hereafter. Genetic Algorithm (GA), a procedure simulating

the natural evolution process, has been successfully used in a wide array of applications due to ease of implementation and robust performance. GA is especially suitable for the design problem of this research since it does not require gradient information and it is the perfect fit for discrete optimization problems. A typical GA uses reproduction, crossover and mutation operations to create a subsequent generation based on the relative fitness values of the current generation. Thus, the average quality of the solutions is improved from one generation to the next. The striking advantage of using GA for multi-objective optimization problems is that a population of solutions is processed in each iteration (or generation), and the outcome of one implementation is also a population of solutions. In each generation of the adopted MGA, the pair-wise comparisons (with respect to all of the objectives) are conducted to classify the population into a non-dominated set and a dominated set (the solutions of the non-dominated set are better than those of the dominated set). Thus, multiple trade-off solutions among each generation can be determined in one single run. As the population set improved with respect to the non-dominated set of solutions, the MGA will end up with the Pareto-optimal solutions in its final population.

For the multi-objective design optimization problem Equations (3 - 8) to (3 - 12), the design procedure is described as follows:

1) Each of the design variables $x_i (i = 1,2, \dots n)$ is encoded with a fixed-length binary string regarding to the side constraints.
2) Each design is represented by a unique Binary String Chromosome formulated from the encoded design variables.
3) The first generation of designs is randomly generated.
4) The objectives and constraints of each design of the current generation (or population) are evaluated by using Nonlinear Time-History analysis.
5) The design objectives are normalized with respect to their maximum values among the current population.
6) A penalty number 1.0 is added to all the three normalized objectives f_1 to f_3 if any of the design constraints is violated.
7) The current population is handled by the Multi-objective Genetic Algorithm to generate a new population set.

8) Repeat step 4 to step 7 until the convergence criterion is satisfied.

The overall design procedure is also illustrated by the flowchart in Figure 3-2. The MGA algorithm embedded in MATLAB software package (The MathWorks Inc. 2009) is adopted and treated as a black box during computer programming. The convergence criterion, called the spread of Pareto-optimal solutions (Deb 2001) is defined as

$$s_p = \frac{d_{ex}+d_m}{d_{ex}+ n_0 d_a} \qquad (3 - 13)$$

where $d_m = \sum_{int} d_i / n_{int}$ is the mean distance of interior Pareto-optimal solutions, and n_{int} is the number of interior Pareto-optimal solutions; $d_i = \sum_{j=1}^{n_0} \left(f_j^{i+1} - f_j^{i-1} \right)$ is the crowding distance of Pareto-optimal solution *i*, defined as the objective difference of its two neighbouring solutions (*i*+1) and (*i*-1); n_0 is the number of objectives, which is equal to 3 for this study; d_{ex} is the distance between extreme Pareto-optimal solutions; and $d_a = \sqrt{\sum_{int}(d_i - d_m)^2 / n_{int}}$ for interior Pareto-optimal solutions. The more detailed description of s_p can be found in MATLAB. A design iterative process is considered to converge if the average change of s_p over a number of generations is less than a specified tolerance. Alternatively, a design process may be terminated if a specified maximum generation number is reached.

In summary, the nonlinear dynamic analysis-based capacity design of steel building frameworks is cast into a multi-objective optimal design problem and it is solved using a genetic algorithm.

Chapter 4

Design of Moment Resisting Frames

This chapter presents optimal design solutions for a 3-story and 4-bay Moment Resisting Frame (MRF). The design problems serve as the numerical examples to illustrate the effectiveness and practicability of the proposed optimal design formulation in the previous chapter. The specific techniques and numerical strategies required for conducting design of MRFs are demonstrated through the examples.

4.1 Geometry and Seismic Loading of the 3-Story-4-Bay MRF

The MRF is the seismic force resisting system of a hypothetical three-story office building located in Vancouver, British Columbia, Canada.

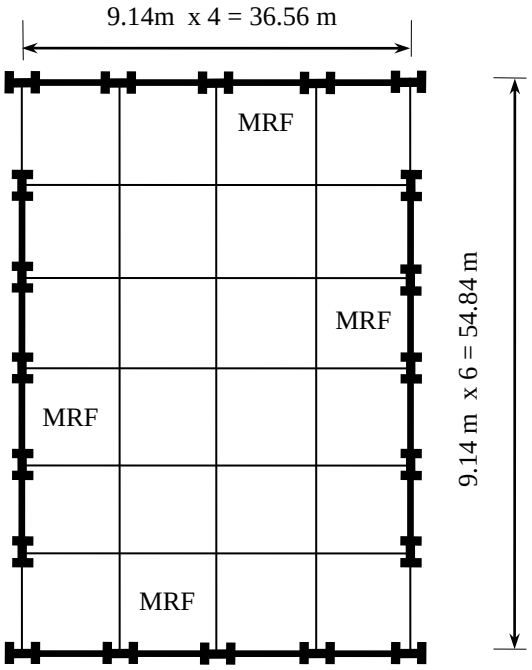

Figure 4-1 Plan view of the hypothetical office building

The plan view of the office building is shown in Figure 4-1. The structural layout is symmetric and the seismic lateral loads in each principal direction are resisted by a pair of 4-bay MRFs located at the perimeter of the building. The schematic side view of a MRF is illustrated in

Figure 4-2. A fictitious lean-on column, connected with the MRF through a rigid link at each floor level, is used in the analytical model to simulate the effect of interior simple gravity frames. For the purpose of illustration, only east-west direction MRF design is considered in this example.

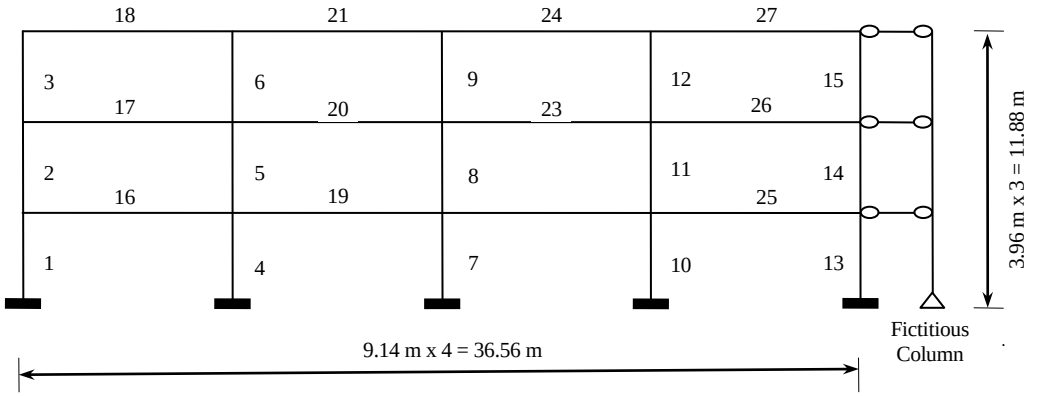

(a) member numbering

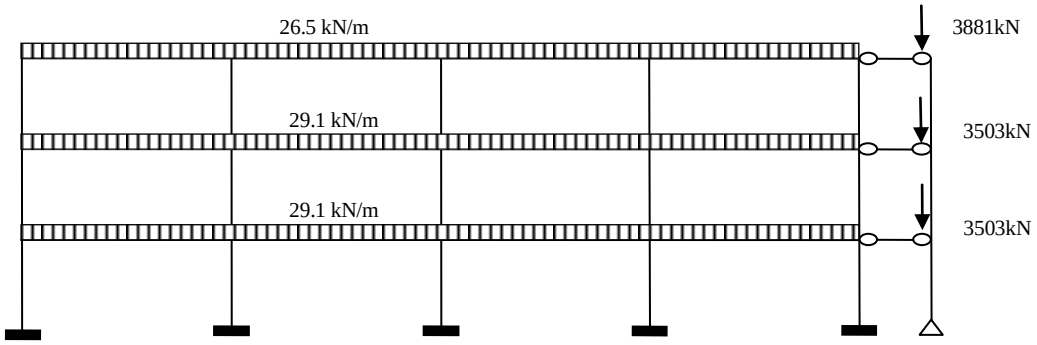

(b) seismic weight distribution

Figure 4-2 Side view of the E-W direction MRFs

All four bays are each 9.14 m wide (centerline dimensions) and all three stories are each 3.96 m high. The design dead and live load are 4.79 kPa and 2.39 kPa for both of the first and second story, respectively. The roof has dead load of 4.07 kPa and live load of 0.96 kPa. For each frame, the seismic weights of floors 2, 3, and the roof are 4567 kN, 4567 kN, and 4850 kN, respectively. The distribution of the seismic weights among the frame and the leaning column is illustrated in Figure 4-2(b).

Table 4-1 Selected ground motion time-histories

Record Name	Earthquake Magnitude	PGA (g)	PGV (cm/sec)	Scale Factor
1979 Imperial Valley: El Centro Array #12 (EL_2.1)	6.5	0.143	17.6	2.1
1989 Loma Prieta: Belmont Envirotech (BES000_4.5)	6.9	0.108	11.8	4.5
1994 Northridge: Old Ridge RT 090 (ORR090_0.8)	6.7	0.568	52.1	0.8
1989 Loma Prieta: Presidio (PRS090_1.5)	6.9	0.2	32.4	1.5

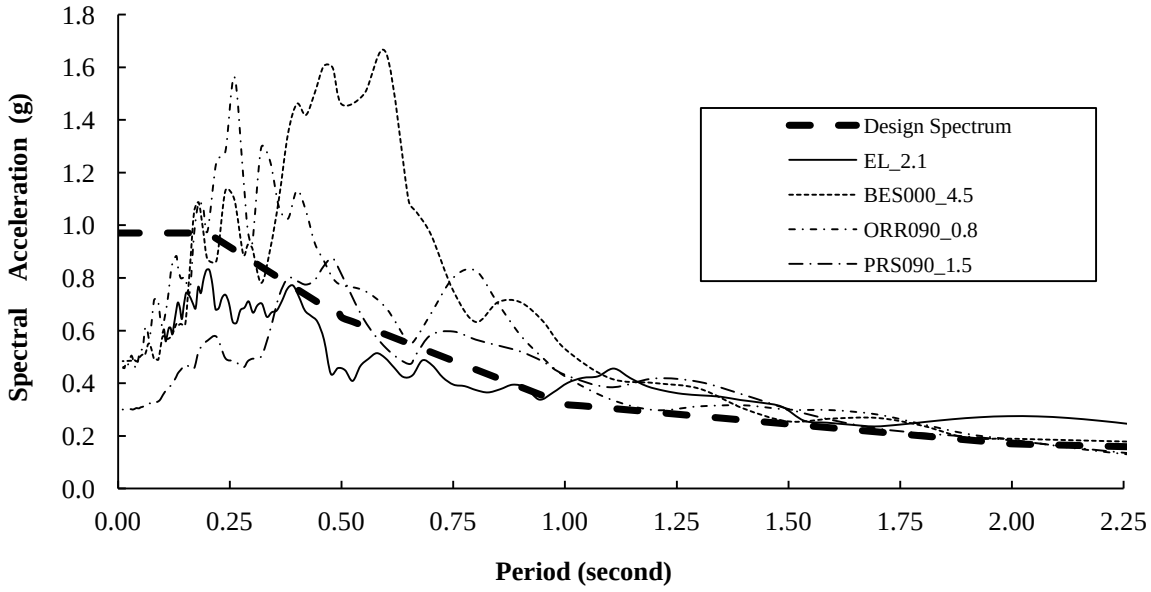

Figure 4-3 Response spectra

The design response spectrum for Vancouver specified by the National Building Code of Canada (NRCC 2010) is employed as the datum for scaling ground motions. The spectral acceleration values are 0.97g, 0.65g, 0.32g, 0.17g, and 0.085g at period T = 0.2, 0.5, 1.0, 2.0, and 4.0 sec, respectively (g is the gravity acceleration). Though FEMA-450 (FEMA 2004a) requires seven ground motions to establish average values of the structural response, with the view to mitigate calculation burden, only four ground motions (i.e., n_g=4) are herein adopted from PEER (PEER 2008) for this example. The selected ground motion time-histories need to be scaled such that their response spectra equal to or exceed the design response spectrum throughout the period range of interest. The names of the adopted ground motion records and the corresponding scale

factors are shown in Table 4-1 (the ground motion acceleration histograms are given in Appendix 4.A). Illustrated in Figure 4-3 are the response spectra of the scaled ground motions. Note that these response spectra are equal to or greater than the design spectral values throughout the period ranging from 1.0 sec to 2.25 sec.

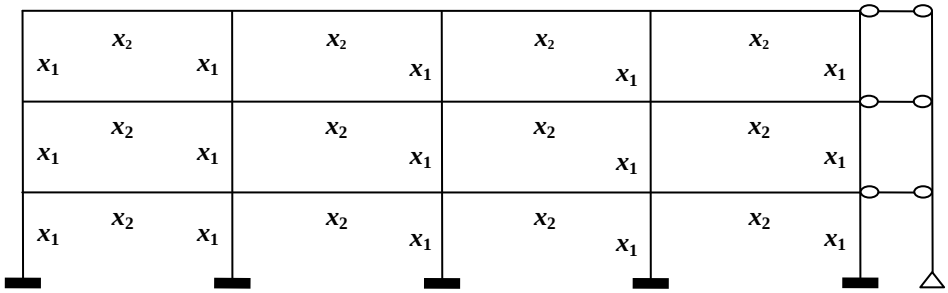

(a) design variable groups of design example one

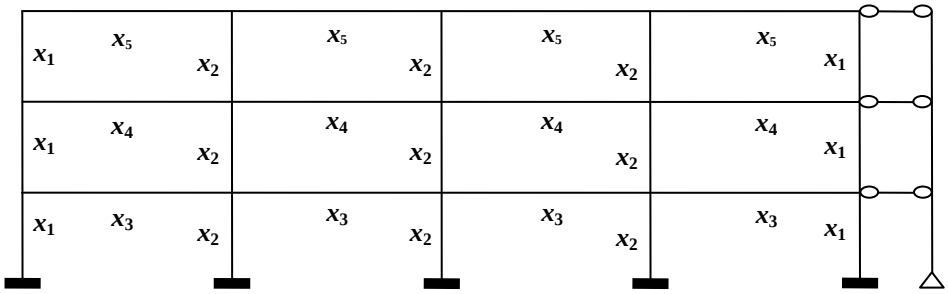

(b) design variable groups of design example two

Figure 4-4 Design variable groups of MRF

The frame is assumed to have rigid beam-to-column connections, with all column bases fixed at the ground level. All the columns use wide-flange sections of 345 MPa grade steel, while all the beams use wide-flange sections of 248 MPa grade steel based on the consideration of ductility. As shown in Figure 4-2(a), the MRF consists of 27 structural members. Two different numerical examples will be executed for this MRF according to different member linking schemes. The first example, with only two design variables, as shown in Figure 4-4(a), is used to illustrate the basic behaviour of the design formulation. The second example, optimizing the same moment resisting frame with more design variables, as shown in Figure 4-4(b), is carried out to illustrate the method applied to a larger scale design problem.

4.2 Design Example One

For example one (Figure 4-4(a)), all the beams have the same cross-section and are designed as a fuse-member group, while all the columns are assumed to have the same cross-section and are linked as a non-fuse-member group. The design problem has two variables. The first variable x_1, the column section, is to be selected from among W360 sections (which are the most commonly used column shapes). The second variable x_2, the beam section, is to be selected from among W460 sections. Table 4-2 lists the W360 and W460 section sets $\mathbf{C}_1$ and $\mathbf{C}_2$, each consisting of eight compact sections, whose other sectional properties can be found in Handbook of Steel Construction (CISC 2010).

Table 4-2 Section sets for design variables of design example one

Index	Column Section $\boldsymbol{C_1}$	Section area A (mm^2)	Plastic modulus Z (10^3 mm^3)	Moment of inertia I (10^6 mm^4)	Beam Section $\boldsymbol{C_2}$	Section area A (mm^2)	Plastic modulus Z (10^3 mm^3)	Moment of inertia I (10^6 mm^4)
1	W360x262	33500	5260	894	W460x128	16400	3050	637
2	W360x237	30100	4690	788	W460x106	13500	2390	488
3	W360x216	27600	4260	712	W460x97	12300	2180	445
4	W360x196	25000	3840	636	W460x89	11400	2010	410
5	W360x179	22800	3480	575	W460x82	10400	1830	370
6	W360x122	15500	2270	365	W460x74	9450	1650	333
7	W360x101	12900	1880	301	W460x68	8730	1490	297
8	W360x79	10100	1430	226	W460x60	7590	1280	255

The reason to use compact sections is because the beams as fuse members are expected to form plastic hinges and the columns might form plastic hinges at their base even though they are non-fuse members. The sectional properties of the fictitious column include moment of inertia 845×10^6 mm^4 and cross-sectional area 89,000 mm^2, which are equal to the sum of the corresponding values of all the gravity columns (which is taken as HSS254x254x13) divided by the number of moment frames in the considered direction. In accordance with ASCE/SEI 41-06 (ASCE 2007), the plastic rotation limits for individual frame members are estimated to be somewhere between $2.0\theta_y$ and $3.0\theta_y$. For simplicity, this example adopts 0.015 radians as the

plastic rotation limit φ_0 for all frame members. The inter-story drift limit δ_0 is taken as 2.5% of the story height (i.e., $\delta_0 = 3960 \times 0.025 = 99$mm).

The seismic demands for the candidate design solutions under the four selected ground motion time-histories are evaluated by using the programmed codes of OpenSees software (OpenSees 2008). The bilinear elastoplastic stress-strain relationship with 5% strain hardening is employed to represent the material behaviour of structural steel. Based on the assumptions that the cross sections of the structural member in bending remain plane and the stress-strain relationships are uniaxial, the moment-curvature relationship of a W-section is obtained through the integration of 256 subdivided segments over a cross-section (where each portion of web and flanges has been divided into 128 segments). The force-based beam-column elements with five Gauss-Labatto numerical integration points along the length of one element are employed to account for the distributed plasticity characteristic of columns and beams. The mass of a frame member is represented by the point masses at its two nodes. The lumped mass at a joint of the frame is the sum of the mass contributions of all the members connected to the joint. The Rayleigh damping model is employed to construct the damping matrix. The proportionality constants are computed from the frequencies of modes 1 and 3 with damping ratios of 0.05.

For two sizing variables that each has eight section choices, there are 64 possible design solutions for this moment frame. Due to the small number of candidate design solutions we are able to evaluate the structural responses for all the possible designs, which allow us to determine the optimal solutions directly. The beam and column sections for each candidate solution are listed in Table 4-3 along with the corresponding values of the three objectives, the maximum inter-story drift and the maximum member-end plastic rotation.

Table 4-3 Design results

Design	Column Section	Beam Section	Period (sec)	Weight OBJ_1 (kN)	Input Energy OBJ_2 (kN-m)	Hyst. Energy of Beams OBJ_3 (%)	Member End Plastic-Rotation (rad)	Average Maximum Inter-Story Drift (mm)	Col. Strength Ratio r_m	Fea-sible?
1	W360x262	W460x128	1.351	290.4	884.8	80.9	0.0085	78.0	1.6	Y
2	W360x237	W460x128	1.384	275.6	857.9	75.9	0.0080	75.4	1.4	Y

Design	Column Section	Beam Section	Period (sec)	Weight OBJ_1 (kN)	Input Energy OBJ_2 (kN-m)	Hyst. Energy of Beams OBJ_3 (%)	Member End Plastic-Rotation (rad)	Average Maximum Inter-Story Drift (mm)	Col. Strength Ratio r_m	Fea-sible?
3	W360x216	W460x128	1.417	263.5	825.1	71.3	0.0076	75.0	1.3	Y
4	W360x196	W460x128	1.454	252.2	821.6	65.9	0.0076	75.9	1.2	Y
5	W360x179	W460x128	1.489	241.8	827.4	59.7	0.0081	79.0	1.1	Y
6	W360x122	W460x128	1.672	208.8	691.2	29.0	0.0109	95.3	0.7	Y
7	W360x101	W460x128	1.772	196.7	732.2	12.4	0.0142	97.2	0.6	Y
8	W360x79	W460x128	1.933	183.7	727.5	4.9	0.0160	101.4	0.4	N
9	W360x262	W460x106	1.459	266.4	790.1	88.0	0.0083	75.7	2.1	Y
10	W360x237	W460x106	1.493	251.6	796.9	86.1	0.0090	80.2	1.8	Y
11	W360x216	W460x106	1.526	239.5	790.5	83.0	0.0099	85.6	1.7	Y
12	W360x196	W460x106	1.564	228.2	762.7	77.8	0.0102	88.4	1.5	Y
13	W360x179	W460x106	1.599	217.8	736.1	72.2	0.0103	90.1	1.4	Y
14	W360x122	W460x106	1.780	184.8	730.2	47.0	0.0111	101.9	0.9	N
15	W360x101	W460x106	1.877	172.7	774.0	28.4	0.0143	102.5	0.7	N
16	W360x79	W460x106	2.034	159.7	714.3	10.9	0.0156	100.4	0.6	N
17	W360x262	W460x97	1.498	256.8	783.2	91.0	0.0096	82.2	2.3	Y
18	W360x237	W460x97	1.533	242.0	776.1	89.0	0.0105	85.8	2.0	Y
19	W360x216	W460x97	1.566	229.9	758.5	85.3	0.0109	88.8	1.8	Y
20	W360x196	W460x97	1.604	218.6	727.2	80.8	0.0111	90.6	1.7	Y
21	W360x179	W460x97	1.639	208.2	691.7	75.7	0.0108	91.1	1.5	Y
22	W360x122	W460x97	1.820	175.2	750.0	51.2	0.0117	103.2	1.0	N
23	W360x101	W460x97	1.917	163.1	773.2	35.4	0.0137	102.6	0.8	N
24	W360x79	W460x97	2.072	150.1	707.8	14.6	0.0157	101.0	0.6	N
25	W360x262	W460x89	1.543	248.7	758.9	93.5	0.0111	89.7	2.5	Y
26	W360x237	W460x89	1.577	234.0	744.2	90.7	0.0115	91.2	2.2	Y
27	W360x216	W460x89	1.612	221.9	718.4	87.5	0.0117	92.7	2.0	Y
28	W360x196	W460x89	1.650	210.6	683.8	84.0	0.0114	91.4	1.8	Y
29	W360x179	W460x89	1.685	200.2	657.9	79.5	0.0114	94.7	1.6	Y
30	W360x122	W460x89	1.866	167.2	777.9	54.4	0.0120	103.8	1.1	N
31	W360x101	W460x89	1.962	155.1	761.2	41.6	0.0134	101.8	0.9	N
32	W360x79	W460x89	2.116	142.1	702.6	19.6	0.0157	101.7	0.7	N
33	W360x262	W460x82	1.589	240.7	727.3	95.1	0.0121	94.4	2.7	Y
34	W360x237	W460x82	1.624	226.0	703.2	92.4	0.0122	94.8	2.4	Y

Design	Column Section	Beam Section	Period (sec)	Weight OBJ_1 (kN)	Input Energy OBJ_2 (kN-m)	Hyst. Energy of Beams OBJ_3 (%)	Member End Plastic-Rotation (rad)	Average Maximum Inter-Story Drift (mm)	Col. Strength Ratio r_m	Fea-sible?
35	W360x216	W460x82	1.659	213.8	678.3	90.6	0.0121	94.9	2.2	Y
36	W360x196	W460x82	1.698	202.6	658.7	86.6	0.0124	94.6	2.0	Y
37	W360x179	W460x82	1.733	192.2	666.2	83.2	0.0128	98.3	1.8	Y
38	W360x122	W460x82	1.914	159.2	791.5	58.4	0.0120	103.3	1.2	N
39	W360x101	W460x82	2.010	147.1	745.0	47.8	0.0127	99.6	1.0	N
40	W360x79	W460x82	2.163	134.0	696.9	26.3	0.0155	101.2	0.7	N
41	W360x262	W460x74	1.641	232.7	686.2	96.2	0.0126	96.1	3.0	Y
42	W360x237	W460x74	1.677	218.0	670.5	94.8	0.0131	96.7	2.7	Y
43	W360x216	W460x74	1.712	205.8	666.4	92.7	0.0136	99.1	2.4	N
44	W360x196	W460x74	1.752	194.6	676.0	89.2	0.0140	100.6	2.2	N
45	W360x179	W460x74	1.788	184.2	696.3	86.0	0.0141	101.7	2.0	N
46	W360x122	W460x74	1.970	151.2	780.5	62.9	0.0119	101.3	1.3	N
47	W360x101	W460x74	2.066	139.1	726.6	55.4	0.0118	102.9	1.1	N
48	W360x79	W460x74	2.217	126.0	699.3	33.4	0.0152	100.3	0.8	N
49	W360x262	W460x68	1.699	226.3	670.9	97.3	0.0138	99.8	3.3	N
50	W360x237	W460x68	1.736	211.6	682.0	96.1	0.0146	103.9	3.0	N
51	W360x216	W460x68	1.772	199.4	687.6	93.5	0.0149	105.7	2.7	N
52	W360x196	W460x68	1.813	188.2	702.2	90.4	0.0150	106.4	2.4	N
53	W360x179	W460x68	1.849	177.8	741.6	87.3	0.0149	107.5	2.2	N
54	W360x122	W460x68	2.033	144.8	763.4	68.2	0.0117	99.2	1.4	N
55	W360x101	W460x68	2.129	132.6	717.5	59.5	0.0128	101.7	1.2	N
56	W360x79	W460x68	2.280	119.6	709.0	40.1	0.0150	99.9	0.9	N
57	W360x262	W460x60	1.782	216.7	705.3	97.6	0.0160	108.1	3.9	N
58	W360x237	W460x60	1.821	202.0	707.9	95.7	0.0157	110.0	3.4	N
59	W360x216	W460x60	1.859	189.8	724.9	93.7	0.0155	109.9	3.1	N
60	W360x196	W460x60	1.901	178.6	761.3	91.7	0.0155	110.2	2.8	N
61	W360x179	W460x60	1.939	168.1	782.0	89.5	0.0149	108.8	2.6	N
62	W360x122	W460x60	2.126	135.2	741.4	74.5	0.0129	103.1	1.7	N
63	W360x101	W460x60	2.222	123.0	708.7	67.1	0.0133	103.7	1.4	N
64	W360x79	W460x60	2.372	110.0	702.5	47.1	0.0139	100.4	1.1	N

Among the 64 designs, only 29 solutions are feasible. Design #37 best satisfies the minimum weight objective (OBJ_1 = 192.2 kN), design #29 best satisfies the seismic energy input objective (OBJ_2 = 657.9 kN-m), and design #41 best satisfies the hysteretic energy dissipation objective (OBJ_3 =96.2%). Most feasible solutions have the maximum inter-story drift close to its limit 99 mm, indicating the governing constraint in this example is inter-story drift.

The further scrutiny of the 29 feasible solutions reveals 6 Pareto-optimal solutions (Table 4-4). Apparently, designs #37, #29 and #41 are optimal solutions. The other three design solutions, i.e. designs #35, #36 and #42, are equally worthy candidate designs for further consideration. Tables 4-3 and 4-4 provide a means for validating the effectiveness of the proposed optimization algorithm, as shown in the following.

Table 4-4 Pareto-optimal solutions

Design	Column Section	Beam Section	Period (sec)	Weight OBJ_1 (kN)	Input Energy OBJ_2 (kN-m)	Hyst. Energy of Beams OBJ_3 (%)	Member End Plastic-Rotation (rad)	Average Maximum Inter-Story Drift (mm)	Col. Strength Ratio
29	W360x179	W460x89	1.685	200.2	657.9	79.5	0.0114	94.7	1.6
35	W360x216	W460x82	1.659	213.8	678.3	90.6	0.0121	94.9	2.2
36	W360x196	W460x82	1.698	202.6	658.7	86.6	0.0124	94.6	2.0
37	W360x179	W460x82	1.733	192.2	666.2	83.2	0.0128	98.3	1.8
41	W360x262	W460x74	1.641	232.7	686.2	96.2	0.0126	96.1	3.0
42	W360x237	W460x74	1.677	218.0	670.5	94.8	0.0131	96.7	2.7

For the optimization algorithm employed in this example, the population size is taken as 15, and the mutation rate is taken as 0.05. During the design process, the seismic demands of each generated design in MGA are to be evaluated by OpenSees Nonlinear Response History analysis procedure. Since a design might be re-generated in the current and later generations, the seismic demands for each design are stored for a later recovery, if necessary. As a design process approaches the convergence of Pareto-optimal solutions, the demand recovery strategy becomes very effective on saving the computation time. Generally, a MGA procedure can be terminated

when the obtained set of Pareto-optimal solutions does not change over a number of evolutional generations. Specifically, for this example the convergence criterion of a design process is

1) the average changes of the spread s_p of Pareto-optimal solutions (The MathWorks Inc. 2009) is less than 10^{-6} over 100 generations; or,
2) the number of the evolutional generations reaches 500.

Table 4-5 Ten runs' results of the MGA (population = 15)

Index	Obtained solutions
Run 1	All the 6 Pareto-optimal solutions
Run 2	All the 6 Pareto-optimal solutions
Run 3	All the 6 Pareto-optimal solutions
Run 4	All the 6 Pareto-optimal solutions
Run 5	Solutions 35, 36, 37, 41, 42
Run 6	All the 6 Pareto-optimal solutions
Run 7	Solutions 29, 37, 41, 42
Run 8	Solutions 35, 36, 37, 41, 42
Run 9	Solutions 37, 41, 42
Run 10	Solutions 37, 41

As a typical characteristic of numerical evolutionary process (Grierson 2009), GA is not guaranteed to converge to the correct result in a single run. Therefore, a total of 10 MGA runs were conducted to arrive at the results listed in Table 4-5. Indeed, it is shown that although each run does not necessarily lead to the same design group, the obtained solutions are either a subset or the full set of the Pareto-optimal designs. As is a typical exercise for evolutionary algorithm applications, the results of 10 runs are combined together to obtain a set of solutions, which is exactly the same as those solutions in Table 4-4. It was noted that for the two design variables with eight discrete values each, the average running time for one MGA search is about 240 min on a desktop with Intel Core i5 750 CPU and 4 GB random access memory.

The specific requirement for the capacity design principle applied to Moment Resisting Frames is the so-called strong-column-weak-beam. Thus, it is instructive to investigate how the design

criterion OBJ_3 values impact the realization of this capacity design requirement in a design process. To this end, in accordance with CSA-S16, r_m, a parameter named moment-capacity-to-demand ratio for the columns at a typical beam-to-column intersection is defined as

$$r_m = \sum M_{rc} / \sum M_{fc} \tag{4- 1}$$

where the moment capacity, $\sum M_{rc}$, and the moment demand, $\sum M_{fc}$, of the columns are determined as

$$\sum M_{rc} = \sum \Phi\, M_{pc} = \sum 0.9\, F_{yc} Z_c \tag{4- 2}$$

$$\sum M_{fc} = \sum \left(1.1\, R_y\, M_{pb} + V_h\, (x + d_c/2)\right) \tag{4- 3}$$

In the equations, M_{pc} and M_{pb} are the nominal plastic moment resistance of the columns and beams at the intersection; Φ, F_{yc} and Z_c are resistance factor, yield strength of column steel, and plastic modulus of column section, respectively; $M_{pb} = F_{yb}Z_b$, and F_{yb} and Z_b are yield strength of beam steel and plastic modulus of beam section, respectively; d_c is column depth; R_y is the factor to estimate the probable yield stress of steel material during earthquake events (a code recommended value of 1.1 is adopted for this example); V_h is the shear force acting at the beam plastic hinge location when moment ($1.1R_yM_{pb}$) is reached at beam hinge locations. In general, the plastic hinges of a beam are assumed to be ($d_b/2$) away from the column face (hence, $x = d_b/2$ in Equation (4- 3), where d_b is the beam depth).

For this example, since the columns and beams are selected among W360 and W460 sections, the nominal depths of columns and beams are 0.36 m and 0.46 m, respectively. Taking Φ=0.9, as it is suggested by CSA-S16, the value of V_h (x + d_c / 2) can be approximated as $0.12M_{pb}$. Therefore, the moment ratio is rewritten as

$$r_m = \sum 0.9\, F_{yc} Z_c / \sum 1.33 F_{yb} Z_b \tag{4- 4}$$

The value of the moment ratio r_m at a typical interior beam-to-column intersection, the intersection of members 4, 5, 16 and 19 in Figure 4-2, is given in the second last column in Table 4-3 for each design. The relationship between the OBJ_3 and the moment ratio r_m is shown in Figure 4-5 for the feasible solutions. It is evident that the greater the relative strength of the columns is, the greater the hysteretic energy dissipated through the fuse members is. It is also noted that the rate of increase of beam hysteretic energy ratio becomes insignificant when the moment ratio is greater than 2.0 (this value of ratio is dependent upon the configuration and support conditions of the concerned moment resisting frame, and it is different for various frames).

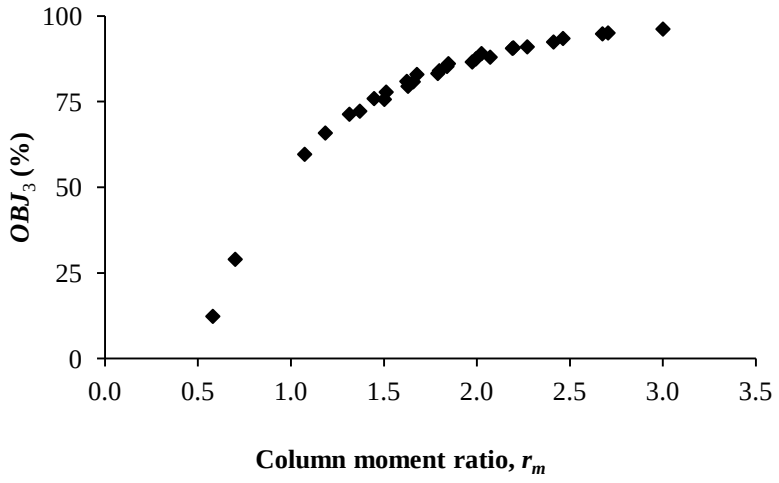

Figure 4-5 Relationship between OBJ_3 and moment ratio r_m

In Table 4-3, each of the feasible design with a moment ratio r_m being greater than 1.0 is a design satisfying the strong-column-weak-beam requirement. Solutions #6 and #7 are weak-column-strong-beam designs among the feasible solutions. Inspection of the obtained Pareto-optimal solutions reveals that the maximization of OBJ_3 indeed enables us to obtain design solutions following capacity design principle. Though the strong-column-weak-beam design requirement can be easily included as an explicit constraint in the design formulation, Equations 3-8 to 3-12, it is not necessary as demonstrated by this design example.

Among the 6 Pareto-optimal solutions, design #41 may not be selected as the final optimum although its objective OBJ_3 = 96.2% has the maximum value, i.e., the design dissipates almost

all of the hysteretic energy through its fuse-members' inelastic behaviour. One reason is that design #41 has the maximum weight among the Pareto-optimal solutions (whose OBJ_1 = 232.7 kN, which is 21% heavier than that of design #37). Another reason is that, it has the largest column moment-capacity-to-demand ratio (which is r_m=3.0) among the Pareto-optimal solutions. As discussed previously, the value of r_m being greater than 2.0 is not necessary for this frame in terms of structural efficiency.

Design #29 has the minimum seismic input energy, OBJ_2 = 657.9 kN-m. However, comparing with design #41 whose seismic input energy is 686.2 kN-m (the greatest value among the Pareto-optimal solutions), there is only 4.2% improvement. On the other hand, design #29 has the least, and much lesser than the others', fuse-member hysteretic energy dissipation (whose OBJ_3 = 79.5%, meaning almost 20% hysteretic energy dissipation occurs among the columns). By inspection, design #36 appears a better solution than design #29 as both have similar OBJ_1 and OBJ_2 values but design #36 has a much better value of OBJ_3.

Design #37 is the minimum weight design. It has a column moment-capacity-to-demand ratio r_m=1.8, which satisfies strong-column-weak-beam requirement. It also has the average fuse-member hysteretic dissipation among the Pareto-optimal solutions, and its seismic input energy is only 1.2% greater than that of design #29. Therefore, design #37 appears more attractive in comparison with other solutions.

The other 3 Pareto-optimal solutions further reflect the compromise among the three objectives. Specifically, design #36 may be selected as the optimum because it has better fuse-member hysteretic energy dissipation value than design #37 and it has the least weight among the 3 solutions.

In summary, although none of the 6 Pareto-optimal solutions can be shown to dominate, with the help of above discussion, one can easily choose a final solution based on his/her preference.

4.3 Design Example Two

As shown in Figure 4-4(b), example two has five design variables. Design variables x_1 and x_2 are the exterior W310 and interior W360 column sections, respectively. Design variables x_3, x_4, and

x_5 are W610, W530 and W460 beam sections of floor 2, floor 3 and roof, respectively. Section sets $\mathbf{C}_1$, $\mathbf{C}_2$, $\mathbf{C}_3$, $\mathbf{C}_4$ and $\mathbf{C}_5$ (Table 4-6), each consisting of four compact sections, are chosen with respect to the six Pareto-optimal solutions of example one. To be consistent with example one, the plastic rotation limits for columns and beams are still taken as 0.015 radians.

For five sizing variables with four section choices each, there are 1024 possible design solutions. Following the same MGA algorithm, except that the population size is increased to 50, the design results of 5 runs are summarized as follows.

Table 4-6 Section sets for design variables of design example two

Variable	Section set $\mathbf{C}_i$	A (mm^2)	Z_x (10^3 mm^3)	I (10^6 mm^4)
Columns x_1	W310x226	28900	3980	596
	W310x202	25800	3510	520
	W310x179	22800	3050	445
	W310x158	20100	2670	386
Columns x_2	W360x237	30100	4690	788
	W360x216	27600	4260	712
	W360x196	25000	3840	636
	W360x179	22800	3480	575
Beams x_3	W610x113	14400	3290	875
	W610x101	13000	2900	764
	W610x92	11800	2530	651
	W610x82	10500	2210	565
Beams x_4	W530x92	11800	2360	552
	W530x85	10800	2100	485
	W530x74	9520	1810	411
	W530x66	8370	1560	351
Beams x_5	W460x89	11400	2010	410
	W460x82	10400	1830	370
	W460x74	9450	1650	333
	W460x68	8730	1490	297

As shown in Tables 4-7 and 4-8, a Pareto-optimal set with 17 solutions is obtained. The weight of the optimal solutions ranges from 181 kN to 212 kN, while the seismic input energies fall in the domain from 659 kN-m to 721 kN-m. All optimal designs have OBJ_3 values greater than 85% (i.e., at least 85 per cent seismic energy is dissipated by fuse members or beams).

From the viewpoint of optimization, an economical outcome can be expected when most of the design constraints are active. In comparison with design example one, the constraint values of the obtained Pareto-optimal solutions are more likely to be active simultaneously, i.e., both the maximum member end plastic rotation and the maximum inter-story drift are near the allowable values of 0.015 radians and 99mm, respectively.

Table 4-7 Search results of design example two

Index	Exterior column x_1(W)	Interior column x_2(W)	Floor 2 beam x_3(W)	Floor 3 beam x_4(W)	Roof beam x_5(W)
1	310x226	360x196	610x82	530x66	460x82
2	310x202	360x237	610x82	530x66	460x82
3	310x202	360x216	610x82	530x66	460x82
4	310x202	360x196	610x82	530x66	460x82
5	310x202	360x179	610x82	530x66	460x82
6	310x179	360x237	610x82	530x66	460x82
7	310x179	360x216	610x82	530x66	460x82
8	310x179	360x179	610x82	530x74	460x74
9	310x179	360x179	610x82	530x66	460x89
10	310x179	360x179	610x82	530x66	460x82
11	310x158	360x237	610x82	530x66	460x82
12	310x158	360x216	610x82	530x74	460x74
13	310x158	360x216	610x82	530x66	460x82
14	310x158	360x196	610x82	530x66	460x82
15	310x158	360x179	610x82	530x74	460x74
16	310x158	360x179	610x82	530x66	460x89
17	310x158	360x179	610x82	530x66	460x82

Table 4-8 Structural Response of design example two

Index	Period (sec)	Weight OBJ_1 (kN)	Input Energy OBJ_2 (kN-m)	Hyst. Energy of Beams OBJ_3 (%)	Member End Plastic-Rotation (radians)	Average Maximum Inter-Story Drift (mm)
1	1.626	204	683	91	0.0138	98.1
2	1.587	212	721	94	0.0140	98.8
3	1.612	205	696	92	0.0139	98.4
4	1.639	198	672	90	0.0137	97.0
5	1.664	192	662	89	0.0140	96.9
6	1.599	207	708	93	0.0140	98.6
7	1.624	199	684	91	0.0138	97.4
8	1.656	187	673	88	0.0131	98.0
9	1.670	189	659	86	0.0139	93.8
10	1.677	186	662	88	0.0142	97.1
11	1.610	202	698	92	0.0140	98.1
12	1.615	195	693	90	0.0132	98.3
13	1.635	194	674	90	0.0138	96.6
14	1.664	188	663	89	0.0141	96.1
15	1.669	182	672	87	0.0133	97.7
16	1.683	184	661	85	0.0141	95.2
17	1.690	181	666	87	0.0145	98.0

Among the 17 optimal solutions, the difference between the beams of floor levels 2 and 3 is minimal. It is shown that heavier column section sizes are generally corresponding to a higher level of hysteretic energy dissipation of beams. If only changing the beam sections at roof level occurs (e.g., designs #9 and #10, designs #16 and #17), a lighter beam section results in a greater hysteretic energy dissipation ratio of beams. It is re-assured that objective function OBJ_3 works well to enforce the strong-column-weak-beam requirement.

Comparing with design example one, most of the optimal solutions of design example two have a better OBJ_1 value. Due to more design variables in design example two, the material

distribution among the MRF is more consistent with structural demands, which leads to more economical design solutions.

The selection of a final solution among the Pareto-optimal set involves a trade-off among the three design criteria. For this example, the author would recommend design #17, since its weight is the least and its seismic input energy is only 1% greater than the best value (i.e., 659 kN-m of design #9) and its fuse members dissipate 87% of the hysteretic energy.

In addition to the objective and design constraint values provided in Table 4-8, the detailed responses of design #17 under ground motion "1979 Imperial Valley: El Centro Array #12" are provided hereafter to illustrate the structural behaviour of the optimal design.

As shown in Figures 4-6 and 4-7, the peaks and valleys of the response histories of the lateral deflection (read at the first column line) at various elevations follow the same trend. The maximum inter-story drift was observed at story 2 while the maximum deflection occurs.

The height-wise distribution of maximum inter-story drift does not exhibit significant difference (Figure 4-8), which suggests that a relatively uniform stiffness distribution exists height-wise. The unexpected plastic localization would hardly happen.

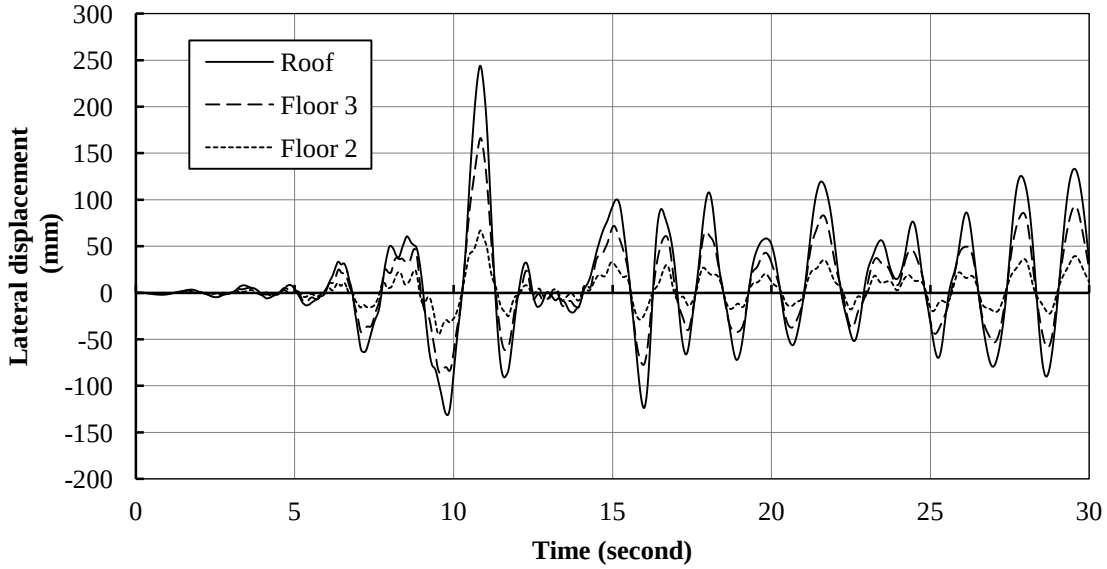

Figure 4-6 Lateral displacement response histories

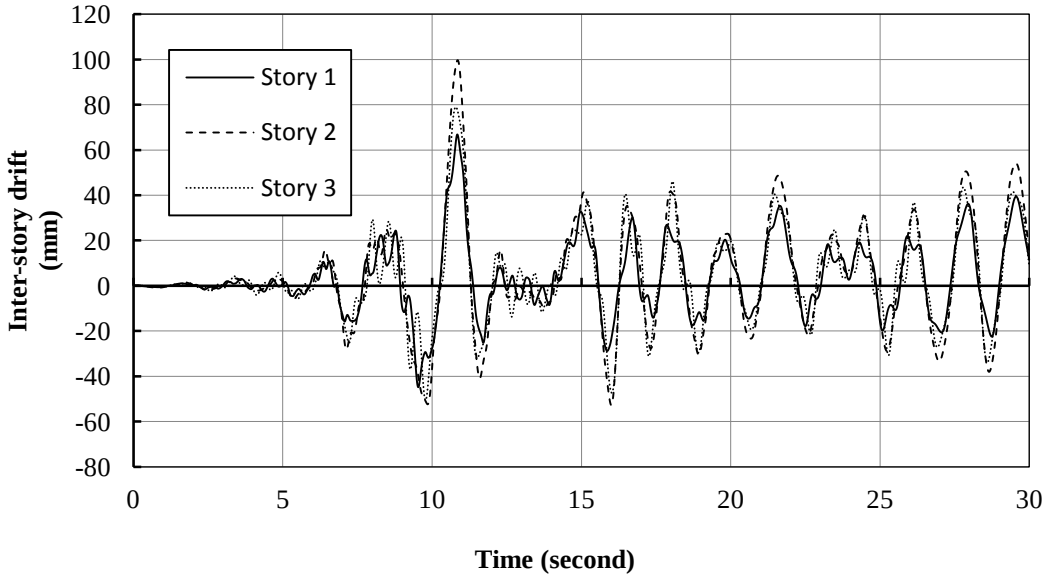

Figure 4-7 Inter-story drift response histories

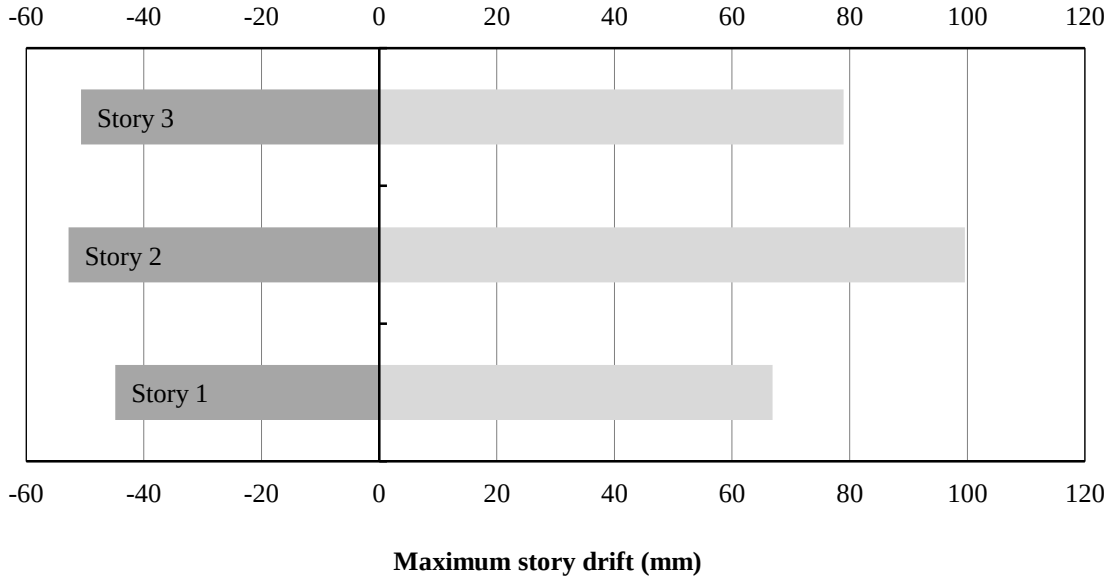

Figure 4-8 Distribution of the maximum inter-story drift

Figure 4-9 provides the history of the base shear, which is obtained by summing the shear force of all the columns at the first story. The shape of the base shear history is somewhat different than that of the lateral displacement in Figure 4-6. In particular, it is noticed that the peak base shear occurs at 9.5 second while the peak roof drift occurs at 10.9 second. The reason for this lack of synchronization is due to a softening effect that occurs at the first story, a phenomenon shown in Figure 4-10 (note that the story shear decreases when the story drift is greater than 43mm).

Figures 4-11 and 4-12 give the bending moment and plastic rotation histories of the beam end at the first column line. It is observed that the maximum plastic rotations occur at 10.9 second, the same instant the maximum roof drift occurs. Figures 4-13 to 4-15 plot the bending moment - plastic rotation hysteretic curves. As expected, the hysteresis loops are consistent with the assumed ductile beam behaviour.

In summary, the analytical results show that design #17 satisfies design constraints and exhibits excellent performance under the strong earthquake ground motion.

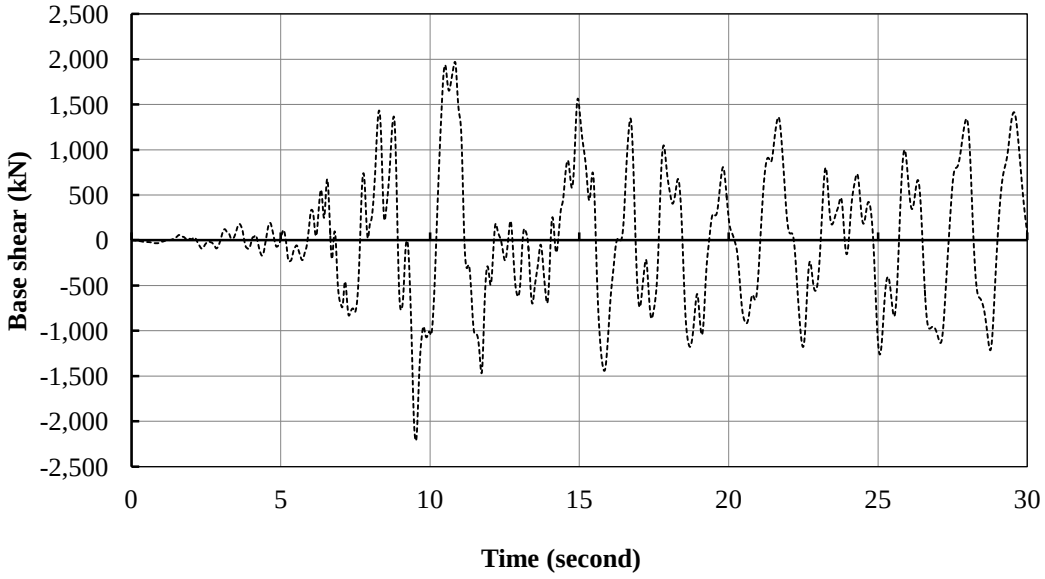

Figure 4-9 Base shear response history

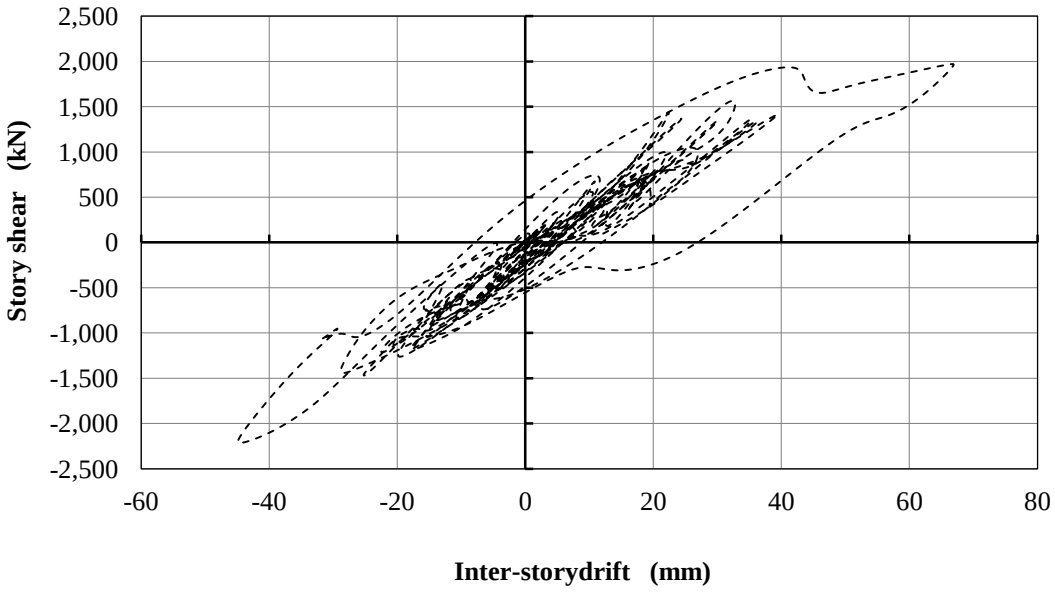

Figure 4-10 First story shear versus inter-story drift

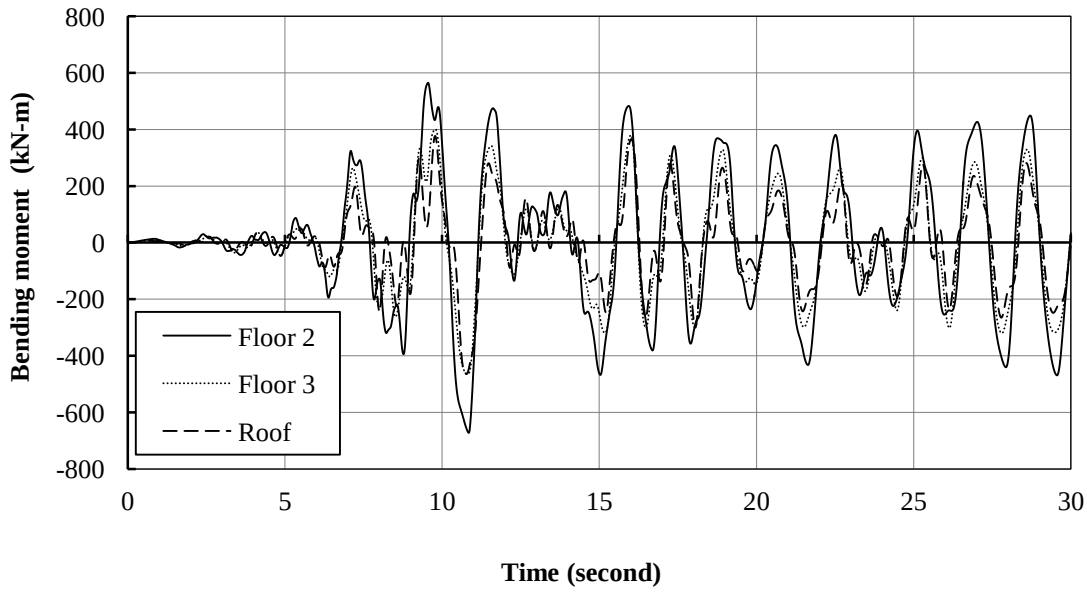

Figure 4-11 Beam bending moment response histories (at the first column line)

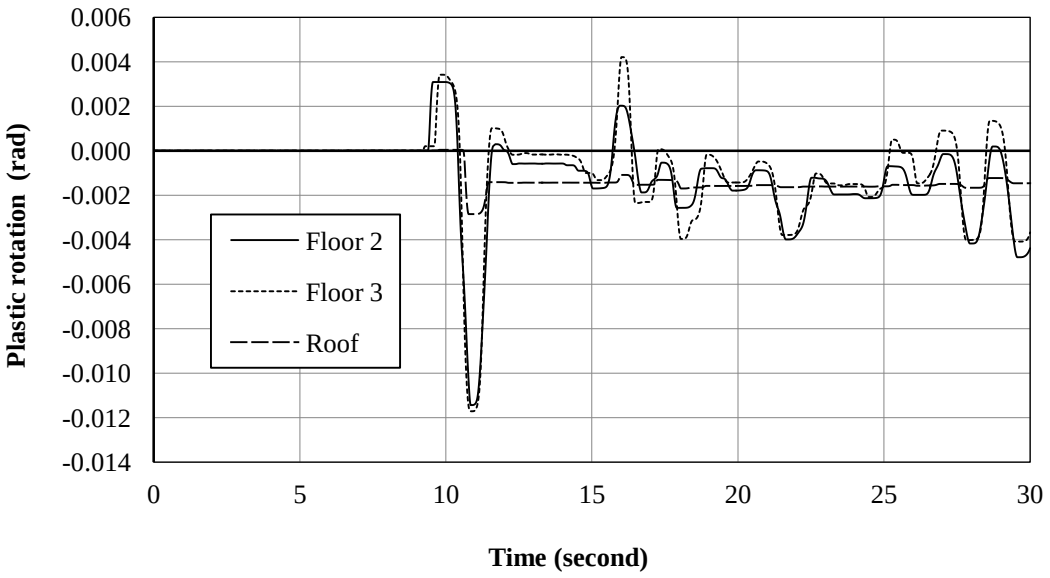

Figure 4-12 Beam end plastic rotation response histories (at the first column line)

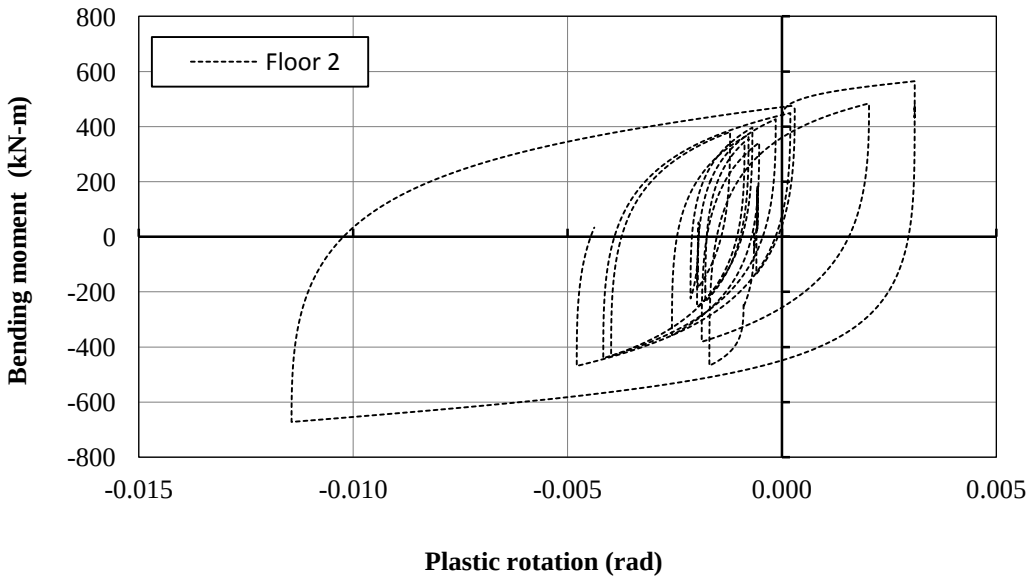

Figure 4-13 Beam bending moment versus plastic rotation (Floor 2)

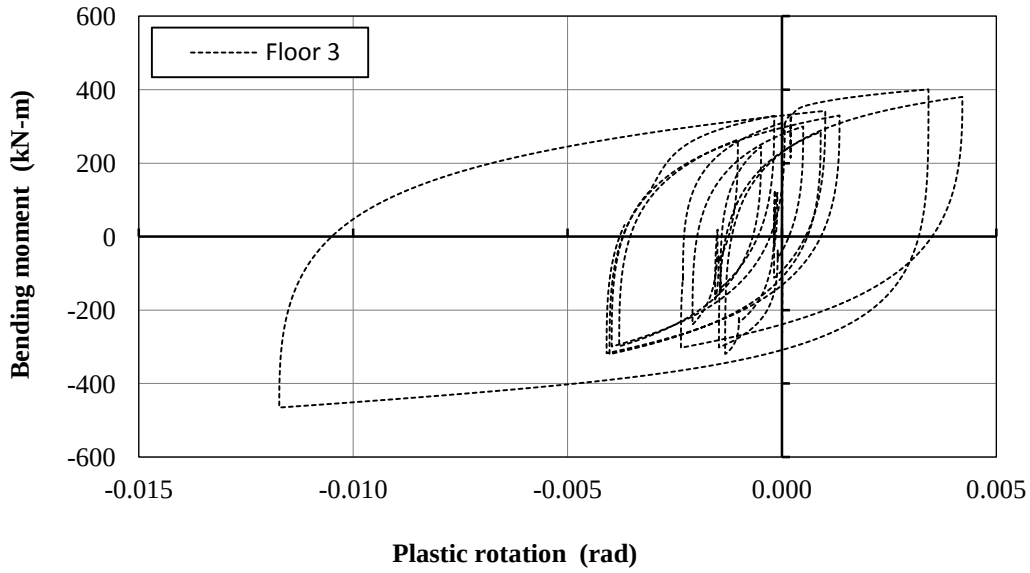

Figure 4-14 Beam bending moment versus plastic rotation (Floor 3)

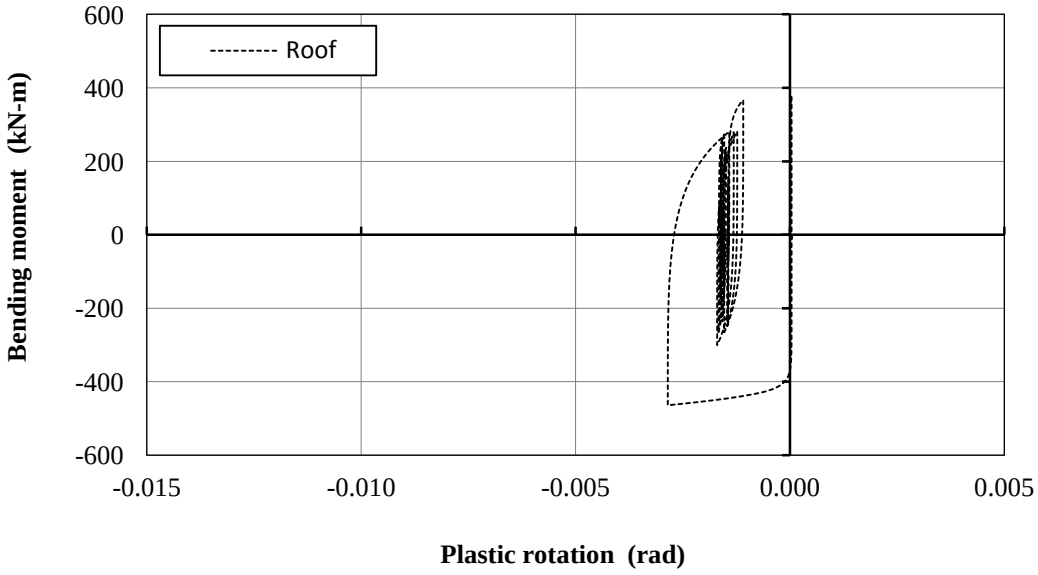

Figure 4-15 Beam bending moment versus plastic rotation (Roof)

Chapter 5

Design of Eccentrically Braced Frames

This chapter illustrates the practical application of the capacity design formulation in Section 3.3 through the design process of an Eccentrically Braced Frame. In this example, the numerical strategies such as including load and resistance factors in the analysis, grouping of design variables considering link and beam outside the link, rounding-off of objective function values, and ranking Pareto-optimal solutions for trade-off are introduced. An analytical model for computing shear link rotation is developed as well.

5.1 Geometry and Seismic Loading of the 3-Story-1-Bay EBF

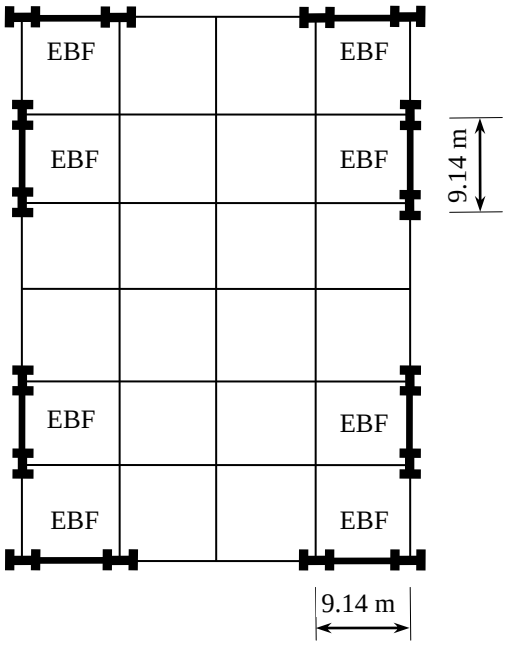

Figure 5-1 Plan view of the hypothetical office building (EBF)

The hypothetical three-story office building, which was employed to demonstrate the optimization design procedure of Moment Resisting Frames in Chapter 4, is redesigned herein by using pairs of Eccentrically Braced Frame (EBF) as the Seismic Force Resisting System. As it is shown in Figure 5-1, in both principal directions each of the original 3-story and 4-bay MRF is

replaced by a pair of 3-story and 1-bay EBFs. For the purpose of illustration, only one EBF design is considered in this example.

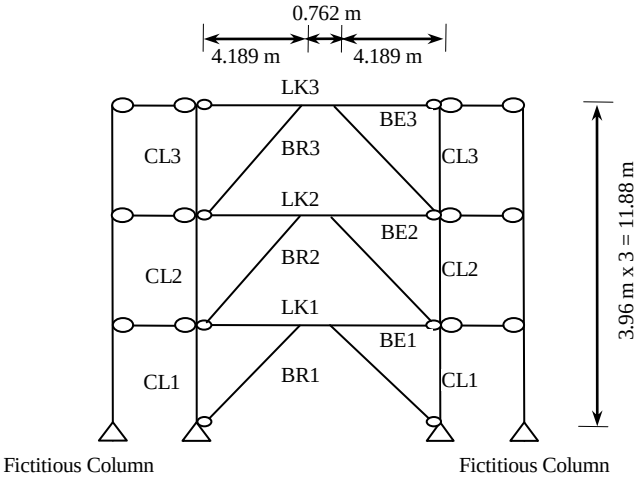

(a) member grouping

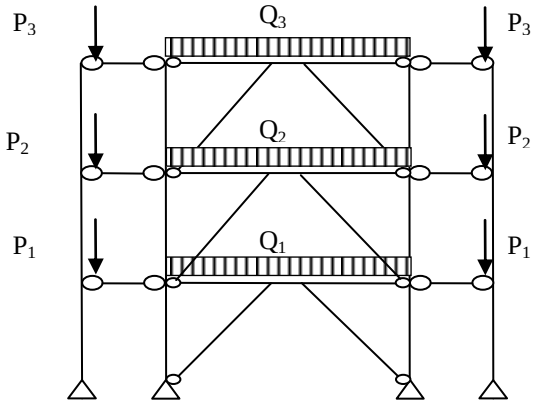

P_3 = 1100 kN Q_3 = 26.5 kN/m
P_2 = 1321 kN Q_2 = 29.1 kN/m
P_1 = 1321 kN Q_1 = 29.1 kN/m

(b) Loading on EBF

Figure 5-2 Side view of the EBFs

The schematic side view of the EBF is illustrated in Figure 5-2. The bay size is 9.14 m center-to-center and all three stories are each 3.96 m high. The columns are continuous over the height and the column bases are pinned. The symmetrically opposed brace pairs are used to maintain the

overall symmetry of seismic response within the plane of the lateral force resisting frames. As it is shown in Figure 5-2(a), in order to avoid the link-to-column moment resisting connections (which are generally expensive and vulnerable to brittle fracture), the braces are concentrically connected to the columns. The beam- and brace-to-column connections are assumed to be pinned. But the brace-to-beam and brace-to-link connections are designed to be rigid, which allows the braces to contribute to the resisting of the moment developed at the end of the links.

Since the bending of the interior gravity columns due to building drift has an impact on the overall lateral stiffness of the structural system, two fictitious lean-on columns are symmetrically arranged to facilitate the simulation of the seismic weight and the destabilizing effect of the gravity loads of the interior simple frames. The sectional properties (i.e., the moment of inertia and the cross-sectional area) of the fictitious columns are taken to the sum of the corresponding values of all the gravity columns (which are HSS254x254x13 sections) divided by the number of EBFs (which is four, as it is shown in Figure 5-1) in the considered direction. Specifically, the moment of inertia of each fictitious column is computed as $I_{pD} = (19 / 4 / 2)\ I_G = 2.375\ I_G$, where I_G is the moment of inertia of one gravity column.

For the EBF configuration shown in Figure 5-2(a), the horizontal component of the brace forces are mainly resisted by the beam segment outside the links. Thus, large axial forces through links are avoided. Popov and Engelhardt (1988) recommended that the brace-to-beam angles should not be less than 40 degrees to avoid introducing greater-than-necessary axial force in frame beams. In this example, it is assumed that the lengths of all the links are 762 mm, which corresponds to a brace-to-beam angle of 43 degree.

The design of the EBF is based on the same gravity loads previously used for the examples of the MRFs. The accompanying gravity loads are given in Figure 5-2(b), where Q_1 to Q_3 are the gravity loads directly applied to the frame members, and P_1 to P_3 are the gravity loads of interior frames which generate destabilizing effect. For this example, we should assume that the load factors for the limit state design philosophy (e.g., NBCC 2010) are already included in the computation of the gravity loads.

Table 5-1 Selected ground motion time-histories for EBF design

Record Name	Earthquake Magnitude	PGA (g)	PGV (cm/sec)	Scale Factor
1979 Imperial Valley: El Centro Array #12 (EL_3.2)	6.5	0.143	17.6	3.2
1989 Loma Prieta: Belmont Envirotech (BES000_4.2)	6.9	0.108	11.8	4.2
1994 Northridge: Old Ridge RT 090 (ORR090_0.8)	6.7	0.568	52.1	0.8

Although more ground motion time history records are desirable (e.g., FEMA-450 requires seven) to establish the average values of seismic demands, with the view to mitigate calculation burden only three ground motion records from PEER (PEER 2008) are adopted for this example. As it is required by governing codes, such as NBCC 2010, the employed ground motion time-histories need to be scaled to the design level.

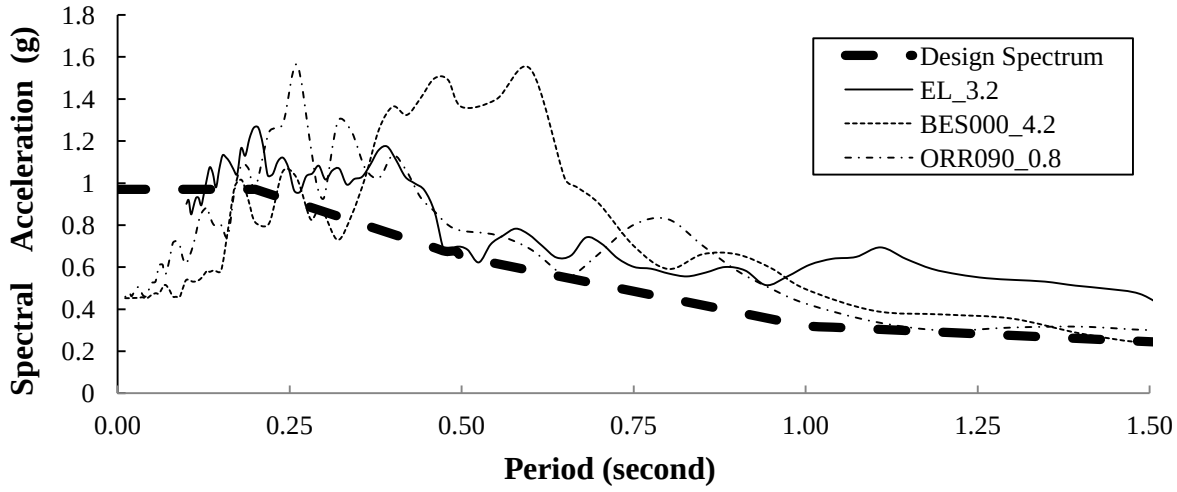

Figure 5-3 Response spectra (for EBF design)

For this example, the fundamental period of the 3-story steel EBF is estimated, according to NBCC 2010, to be $T_a = 0.025(h_n) = 0.297$ sec (where h_n is the height of the building in meters). However, in the subsequent nonlinear time-history analysis it is shown that the fundamental period of the final designs ranges from 0.6 second to 0.8 second. To take into account the deterioration of the Seismic Force Resisting System due to the material yielding, for the nonlinear response history analysis it is conservative to define the period range of interest to range from 0.3 second to 1.25 second. As it is shown in Table 5-1 and Figure 5-3, the selected

ground motion time histories are scaled such that their response spectra are compatible with the design spectrum of NBCC 2010 throughout the periods of interest.

The proposed inelastic-analysis-based design is in essence a limit state design methodology. In a limit state design, member strength equation is generally written as $\sum \alpha_i S_i \leq \Phi R_n$, where Φ and α_i are resistance factor and load factors, respectively; S_i are load effects; and R_n is nominal resistance. To be consistent with the limit state design philosophy, the uncertainty in the prediction of member resistance (i.e., the resistance factor Φ) needs to be included in the design formulation. For an inelastic-analysis-based design, it is more convenient to move the resistance factor to the left side of the strength equation, i.e., to amplify the load effects by $1/\Phi$. Such obtained load effects are called required nominal strength for members. Accordingly, for this design example, the ground motion time-histories are amplified by $1/\Phi$ to account the variation of nominal member strength. Since Φ is typically equal to 0.9 in steel structural design (e.g., CSA-S16-09), the ground motion time-histories in Table 5-1 are further multiplied by 1.11 for evaluating the seismic demands.

Determination of Design Variables

As it is shown in Figure 5-2(a), the member design variables include the column section, the beam section, the brace section and the link section. The link length, which has a major impact on the hysteresis behaviour of a link, is a geometric design variable. For this example, short shear links are adopted since shear links are most commonly used due to their stable energy dissipation capacity (a shear link is also called a shear hinge since the material yielding is concentrated on the web of the link under shear force). In general, link length e should be less than $1.6\ M_p / V_p$ (where M_p and V_p are the plastic moment and shear resistance of the link, respectively), as recommended in CSA-S16-09, in order for the link to act as a shear hinge. Though it can be easily done to include e as a design variable for GA, this example chooses to have a fixed link length of 762 mm throughout the design process in order to exclude link length from its design variable set. The selected link length will satisfy $e < 1.6\ M_p / V_p$ for all the candidate link sections.

If a link and the beam outside the link on the same floor level use one steel component, they are then treated as one design variable. However, one may find it advantageous to design a link and the beam outside the link with different sections due to the following reasons: 1) it is often necessary to have a stronger beam outside the link to carry the combined effect of large axial force and bending moment; and 2) it allows the practice of using replaceable links (Mansour et al 2009).

When a link and the beam outside the link are made using a single steel component, a common practice for obtaining a stronger beam outside of the link is to use flange cover plates. In this case, the strategy to relate the sectional properties of the link and the beam outside the link is as follows. Assume the cross sectional area, plastic modulus and moment of inertia of a link are A_n, Z_n and I_n, respectively. The beam outside the link has a cross sectional area of $(1 + k_n) A_n$, where $k_n \geq 0$. The total sectional area of the two flange cover plates is $k_n A_n$. The area of one cover plate is $(k_n A_n)/2$. The plastic modulus and moment of inertia of the beam outside the link are $Z_n+(k_n A_n/2)(d_n+t_c)$ and $I_n+(k_n A_n /4)(d_n+t_c)^2$, respectively, where d_n is link section depth and t_c is cover plate thickness.

There are three ways to implement the above strategy. First, a link and the beam outside the link use the same design variable with a predetermined k_n value. The cover plate size for each link is thus dependent on the section size of the link itself. Second, a link and the beam outside the link use the same design variable with a predetermined cover plate size. The value of k_n is thus dependent on the size of the link. Third, a link and the beam outside the link use separate design variables. For the third case, it is necessary to establish a cover plate size set. The link section is a design variable while the beam outside the link is replaced by the cover plate size variable which is chosen from among the cover plate size set.

For the illustration of this EBF design example, six design variables are chosen as follows

1) All the columns are designed to have the same section and grouped as the first design variable, x_1.
2) For each floor, the link and the beams outside the link are designed as one structural component (if necessary, the beams outside of the link will be reinforced with 12mm

x100mm flange cover plates) and thus are treated as one variable. The links at floor levels 2, 3 and roof correspond to variables, x_2, x_3, and x_4.

3) The two braces at story 1 are grouped as the fifth design variable, x_5, and the braces at stories 2 and 3 are the sixth design variable, x_6.

Each design variable is to be selected from among 4 candidate section sizes (though more candidate sections can be selected, this example uses four sections only to mitigate computational burden). The properties of the sections are provided in Table 5-2, where the shape for columns and beams is wide-flange I-section and for braces is hollow structural sections. These candidate sections are chosen because they are commonly used in construction and they satisfy the shear link criterion.

The requirements on section class and/or slenderness are accounted for in the selection of the candidate sections. For example, as it is required by Canadian standard S16-09 (CSA 2009), only compact sections are allowed for the columns and braces. However, developing an automated selection of section sets is beyond the scope of this research, and it is the topic of future work.

Determination of Design Constraint Limits

The allowed inter-story drift limit (as per National Building Code of Canada 2010) is taken as 0.025h, where h is story height. In accordance with the requirements of CSA-S16-09 (CSA 2009), the link rotation capacity is taken as 0.08 radians. It has been suggested (CSA 2009; Ricles and Popov 1994; Koboevic and Redwood 1997) that some yielding of the beams outside the link is acceptable. For this example, the plastic rotation limits at the Immediate Occupancy level as per ASCE/SEI 41-06 (ASCE 2007) are adopted as the non-detrimental plastification for non-fuse members. These limits are estimated to be $0.5\theta_y$, $0.6\theta_y$, and $0.5\theta_y$ [θ_y is yield rotation and $\theta_y = (Z\ F_{ye}\ L) / (6EI)$, where: Z, L, E are plastic modulus, length, and Young's modulus of the member, respectively] for columns, beams outside the links, and braces, respectively, and they are provided in Table 5-3. In actual implementation, the plastic rotation limits on columns, beams and braces are taken as 0.005, 0.005 and 0.010 radians, respectively.

Table 5-2 Section sets for design variables of EBF design

Variable	Section $\mathbf{C_i}$	A (mm^2)	Z_x (10^3 mm^3)	I (10^6 mm^4)	I with cover plates (10^6 mm^4)	$1.6M_p/V_p$ (mm)
Columns (CL) x_1	W310x107	13600	1770	248		
	W310x79	10100	1280	177		
	W310x52	6670	841	119		
	W310x33	4180	480	65		
Link and beams (BE1 & LK1) x_2	W410x100	12700	2130	398	507	1514
	W410x74	9550	1510	275	383	1097
	W410x60	7580	1190	216	321	1105
	W410x46	5890	885	156	259	913
Link and beams (BE2 & LK2) x_3	W410x74	9550	1510	275	383	1097
	W410x60	7580	1190	216	321	1105
	W410x46	5890	885	156	259	913
	W360x39	4980	662	102	182	839
Link and beams (BE3 & LK3) x_4	W410x60	7580	1190	216	321	1105
	W410x46	5890	885	156	259	913
	W360x39	4980	662	102	182	839
	W360x33	4170	542	82.7	161	779
Braces of story 1 (BR1) x_5	HSS 203x203x13	9260	651	54.7		
	HSS 203x203x9.5	7150	513	43.9		
	HSS178x178x8.0	5240	330	24.8		
	HSS178x178x6.4	4250	271	20.6		
Braces of upper stories (BR2 & BR3) x_6	HSS 203x203x9.5	7150	513	43.9		
	HSS178x178x8.0	5240	330	24.8		
	HSS178x178x6.4	4250	271	20.6		
	HSS152x152x6.4	3610	196	12.6		

Table 5-3 Plastic rotation limits for non-fuse members of EBF

Members	Size	I (10^6 mm^4)	Z (10^3 mm^3)	L (mm)	θ_y (radians)	0.5 θ_y (radians) or 0.6 θ_y (radians)
CL	W310x107	248	1770	3936	8.90E-03	4.45E-03
	W310x79	177	1280	3936	9.01E-03	4.51E-03
	W310x52	119	841	3936	8.81 E-03	4.40E-03
	W310x33	65	480	3936	9.20E-03	4.60E-03
BE1 (CP) CP: 12x100	W410x100	513	2672	4191	6.91E-03	4.14E-03
	W410x74	383	2020	4191	6.99E-03	4.20E-03
	W410x60	321	1693	4191	6.99E-03	4.19E-03
	W410x46	259	1383	4191	7.08E-03	4.25E-03
BE2 (CP) CP: 12x100	W410x74	383	2020	4191	6.99E-03	4.20E-03
	W410x60	321	1693	4191	6.99E-03	4.19E-03
	W410x46	259	1383	4191	7.08E-03	4.25E-03
	W360x39	182	1100	4191	8.02E-03	4.81E-03
BE3 (CP) CP: 12x100	W410x60	321	1693	4191	6.99E-03	4.19E-03
	W410x46	259	1383	4191	7.08E-03	4.25E-03
	W360x39	182	1100	4191	8.02E-03	4.81E-03
	W360x33	161	975	4191	8.04E-03	4.83E-03
BR1	HSS 203x203x13	54.7	651	5768	2.17E-02	1.09E-02
	HSS 203x203x9.5	43.9	513	5768	2.13E-02	1.07E-02
	HSS 178x178x8.0	24.8	330	5768	2.43E-02	1.22E-02
	HSS178x178x6.4	20.6	271	5768	2.40E-02	1.20E-02
BR2 & BR3	HSS 203x203x9.5	43.9	513	5768	2.13E-02	1.07E-02
	HSS 178x178x8.0	24.8	330	5768	2.43E-02	1.22E-02
	HSS178x178x6.4	20.6	271	5768	2.40E-02	1.20E-02
	HSS152x152x6.4	12.6	196	5768	2.84E-02	1.42E-02

5.2 Analytical Model of EBF

The capacity design approach for EBF assumes that the inelastic energy dissipation is primarily restricted to links, while all other structural members respond elastically under severe earthquake ground motion time-histories. Accordingly, the traditional design procedure starts with the link proportioning in regard to a code-specified seismic base shear. Then, all other structural members are proportioned with respect to the capacity of the links. Finally, the obtained design is verified by maintaining the elastic-analysis-based prediction of plastic link deformation within a code-imposed limitation.

In the past studies on EBFs (such as Popov and Engelhardt 1988; Ricles and Popov 1994; Ramadan and Ghobarah 1995; Koboevic and Redwood 1997), non-fuse members are generally modelled as elastic-response member only, while only links are simulated as inelastic-response members.

However, for this study, the model for non-fuse members must be able to consider material yielding as well since it is impossible to warrant an elastic behaviour for non-fuse members of a randomly generated candidate design solution during a design process. Furthermore, as mentioned previously, some limited yielding of non-fuse members is acceptable as long as the minor plastification does not impact the integrity of SFRS.

Shear Link Modelling

In a well designed EBF, the axial force effect in the link can be neglected (Popov and Engelhardt 1988). Under lateral seismic loads (e.g., Engelhardt and Popov 1989; Popov et al 1990) high shear force combined with high end moments develop simultaneously in the links of EBFs. Influenced by strain hardening effect, both shear and flexural yielding may occur along the length of link. Links are generally modelled based on the lumped plasticity approach with strain hardening effect.

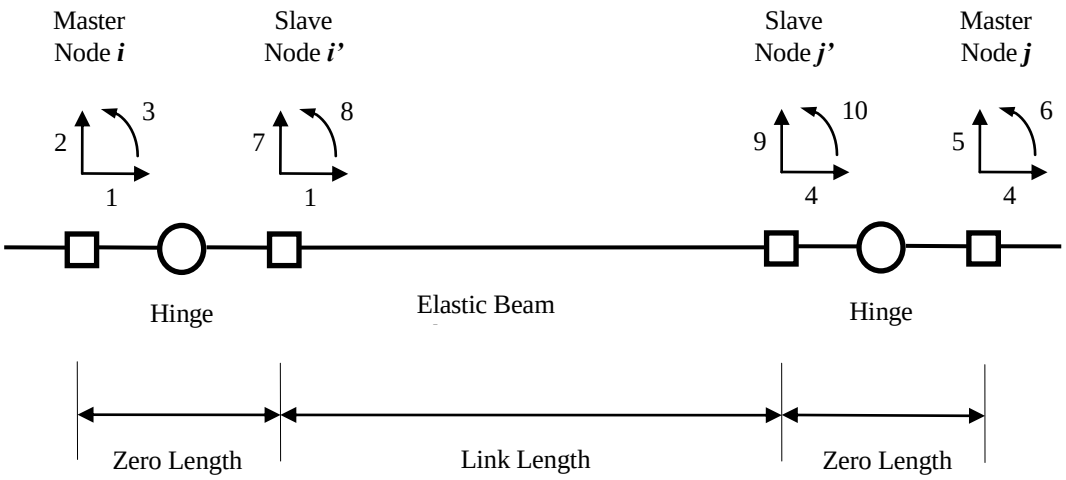

Figure 5-4 Hybrid link element

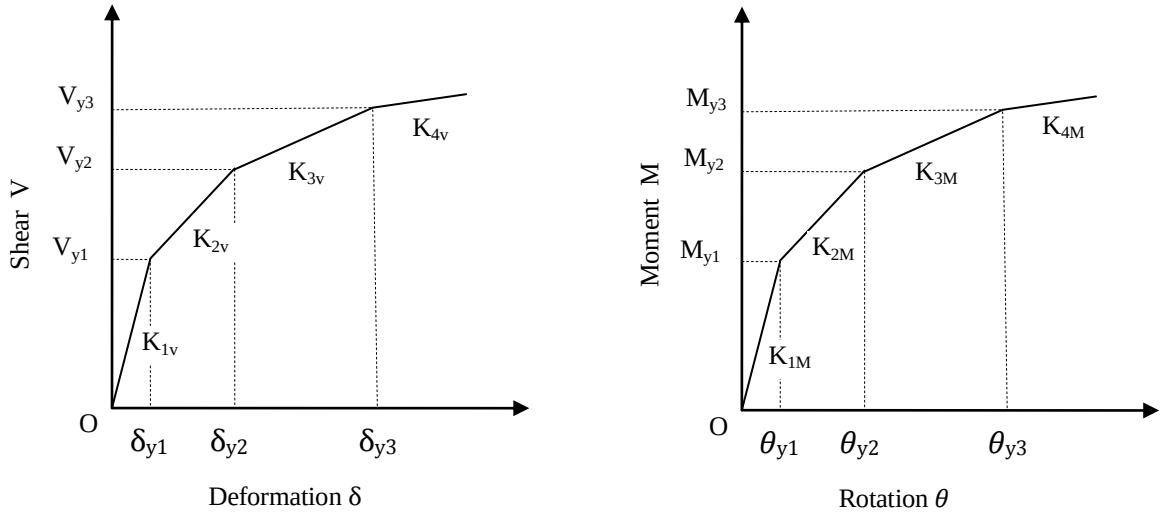

Figure 5-5 Multi-linear force-deformation relationship of link model

Several researchers have developed shear-link models (Ricles and Popov 1994; Ramadan and Ghobarah 1995). A typical link element contains a linear beam element with a series of nonlinear hinges/springs at each end. Multi-linear functions are employed to describe the yielding and strain hardening behaviour of shear and flexure through the appropriately defined hinges/springs

elements, respectively. Compared with the experimental data on shear links (Malley and Popov 1984; Ricles and Popov 1994; Ramadan and Ghobarah 1995), these analytical models show very good agreement in both the initial yield stage and the maximum shear forces.

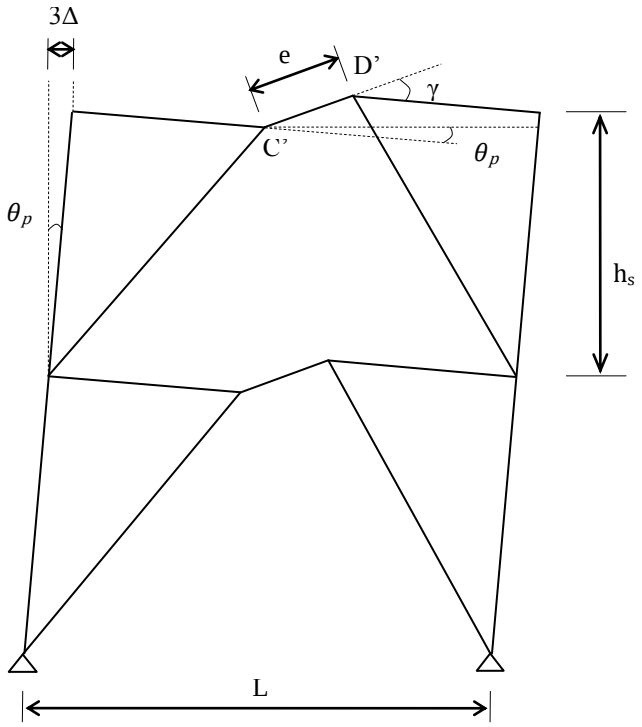

Figure 5-6 Plastic configuration of EBF

For this study, the shear-link element developed by Ramadan and Ghobarah (1995) and later modified by Richards and Uang (2006), as shown in Figure 5-4, was implemented in the OpenSees environment. The model is a hybrid element consisting of a linear elastic beam-column with a nonlinear hinge at each end, at which both the plastic shear and moment deformations are concentrated. The multi-linear functions are defined by the following parameters.

$$V_{y1} = 1.1V_y;\ V_{y2} = 1.3\ V_y;\ V_{y3} = 1.5\ V_y;\ \ V_y = V_p \qquad (5\text{- }1)$$

$$M_{y1} = M_y;\ M_{y2} = 1.03\ M_y;\ M_{y2} = 1.06\ M_y\ ;\ M_y = M_p \qquad (5\text{- }2)$$

$$K_{1v} = 2G\ A_{web}/e\ ;\ K_{2v} = 0.03\ K_{1v}; K_{3v} = 0.015\ K_{1v};\ \ K_{4v} = 0.002\ K_{1v} \qquad (5\text{- }3)$$

$$K_{1M} = \ 6\ E\ I/e\ ;\ K_{2M} = 0.03\ K_{1M};\ K_{3M} = 0.015\ K_{1M}; K_{4M} = 0.002\ K_{1M} \qquad (5\text{- }4)$$

where V_p and M_p are the expected plastic shear capacity and plastic moment capacity of the link section, respectively; $M_p = F_{ye}\ Z_b$, and F_{ye} and Z_b are the expected yield strength and plastic modulus of link section, respectively; $V_p = \left(F_{ye}/\sqrt{3}\right)\left(d - 2t_f\right)t_w$; d, t_f and t_w are the link-section depth, flange thickness and web thickness, respectively; E and G are the Young's modulus and shear modulus of the sectional material, respectively; I and A_{web} are the moment of inertia and the web area of the link section, respectively; e is the link length.

It is necessary to calculate shear link rotation demand since the design constraints include the limit imposed on the plastic rotation of links. For an elastic-analysis-based design approach, the rigid-plastic analysis methods are usually employed to approximate the plastic rotation demands of shear link γ in terms of the plastic inter-story drift ratio θ_p (where θ_p is, recommended by CSA-S16-09, to be taken as 3 times that of the elastic inter-story drift under the code specified seismic load). As the EBF undergoes the target plastic mechanism shown in Figure 5-6, by ignoring elastic deformation, the plastic rotation of a link is estimated to be $\gamma = (L/e)\ \theta_p$, where L and e are bay width and the length of the link, respectively. For this study, a new method to compute link rotation is necessary. As it is shown in Figure 5-6, the link rotation demand can be directly computed in terms of the difference of the vertical displacements between the two ends of the link,

$$\gamma = \frac{y_{D'} - y_{C'}}{e} + \theta_p \qquad (5\text{- }5)$$

where $y_{D'}$ and $y_{C'}$ are the vertical displacements of the end nodes of the link element. Substituting $\gamma = (L/e)\ \theta_p$ into Equation (5-5) gives

$$\gamma = \frac{y_{D'} - y_{C'}}{e}\left(\frac{L}{L - e}\right) \qquad (5\text{- }6)$$

Nonlinear Element Models of Columns, Beams and Braces

Columns, beams and braces are modeled by the force-based beam-column element described in Section 2.2.2. In general, the modeling of geometrically nonlinear behaviour can be improved by subdividing the structural member into smaller elements when its axial force is very large. As it is reflected in the literatures (Uriz, Filippou and Mahin 2008), the model of two elements for one brace member agrees well with the results of the extensive set of experimental data with various slenderness ratios.

For this example, each column, beam outside the link and brace are represented by two force-based beam-column elements with five numerical integration points along the element length. Furthermore, 1/500 of structural member length imperfection to columns, braces and beams (i.e., initial member crookedness) are considered through adjusting the end-nodes of internal elements.

The fictitious columns are modelled as elastic beam-column. Specifically, the simplified *p-Δ* transformation matrix (i.e., Equation (2-55)) is used for the geometrical nonlinearity simulation of the fictitious columns.

For the fibre discretization of the cross-section, each flange and web are discretized into eight layers. The material behaviour of steel is bilinear elastoplastic with 5% strain hardening.

Strength and Damping

Since capacity design principle requires that non-fuse members are proportioned in respect to the actual resistance of the links, the material strength for links in the nonlinear response history analysis should use the probable or expected yield strength in addition to accounting for material strain hardening. The probable yield stress shall be taken as $F_{ye}=R_yF_y$, where R_y is an amplification factor (which is equal to 1.1 in CSA-S16-09). It is assumed that all the structural members in this example use 345 MPa grade steel. The link members use the expected yield strength R_yF_y in the nonlinear response history analysis. Because the outer beam segments are part of the same member as the link, the beams outside the link also use R_yF_y as yielding strength in the analysis. However, the material strength of columns and braces are taken as the specified value, 345 MPa, which is consistent with the normal design practice.

In analysis, seismic masses are concentrated on column lines as well as the master end nodes of the hybrid link elements.

The damping matrix is constructed according to Rayleigh method. First, the proportionality constants of Rayleigh damping for the mass matrix and tangent stiffness matrix are computed from the frequencies of modes 1 and 3 with damping ratios of 0.05. Then, as it is recommended by the literatures (Popov et al 1986; Ricles and Popov 1994; Koboevic and Redwood 1997), only mass-related damping is assigned to the links (to minimize the impact of excessive viscous damping forces in the links).

5.3 Design Results

The Multi-objective Genetic Algorithm (MGA) tool in the MATLAB software is employed to search for the set of Pareto-optimal solutions. For six design variables that each has four candidate sections, there are 4096 possible design solutions.

Each design is represented by a 12-bit binary string, in which each variable corresponds to a 2-bit string with 2^2=4 values being available to the design. The population size of the GA is taken as 30 while the mutation rate is taken as 0.05.

The MGA search is considered to converge if the average changes of the spread s_p of Pareto solutions is less than 10^{-6} over 50 generations. Or, the algorithm will be terminated if the maximum number of generations reaches 150.

A test run was carried out first with the assumption that at each floor level the link and the beams outside the link are of same cross section. This test run ended without a single feasible solution being obtained. An examination of the analysis results revealed that the plastic rotation limits on the beams outside the link were always violated despite the observation that the plastic rotations of the links were usually within the limit. Thus, beams outside the link need to be reinforced with flange cover plates.

Three runs of MGA were conducted. 1142 designs were evaluated. The searched design solutions are plotted in a three-dimensional objective space (Figure 5-7). It was noted that the average running time for one generated design is about 8 min on a desktop with Intel Core i5 750 CPU and 4 GB random access memory.

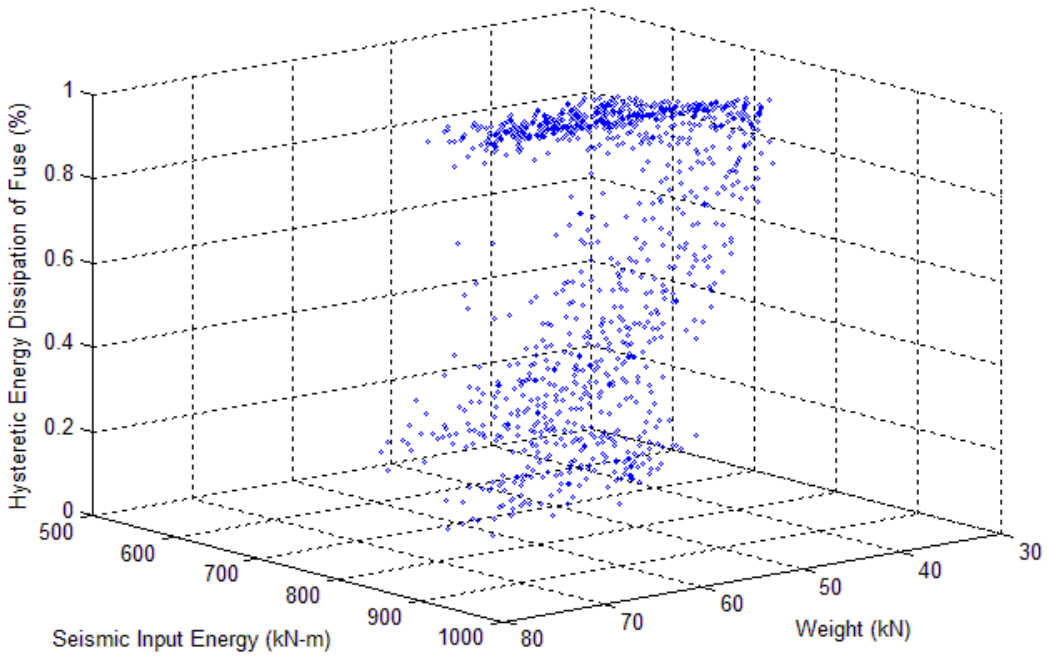

Figure 5-7 Searched design solutions in objective space

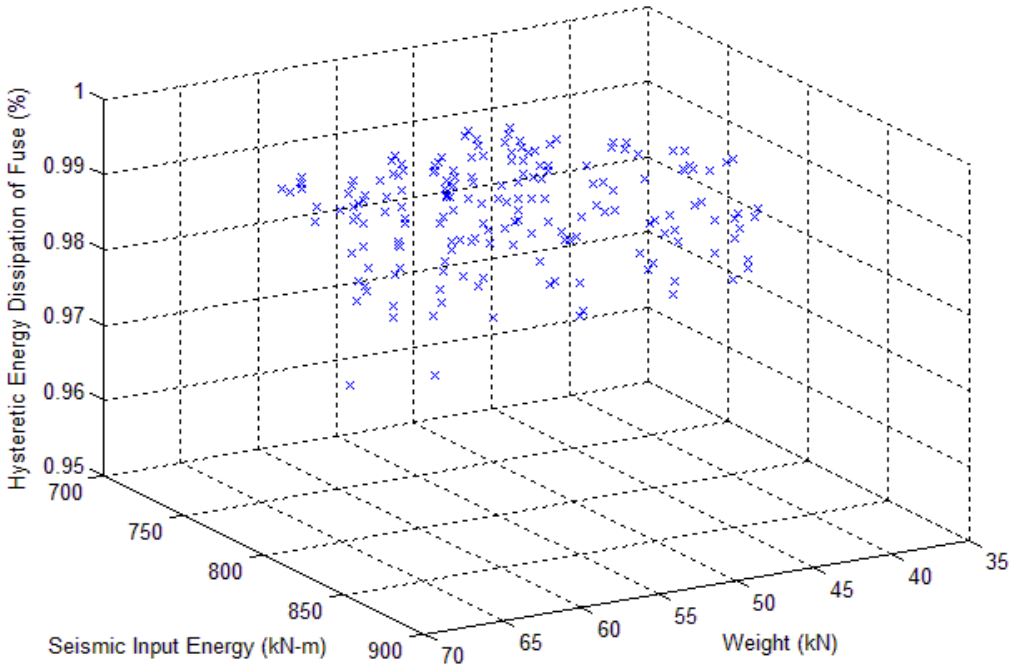

Figure 5-8 Feasible design solutions in objective space

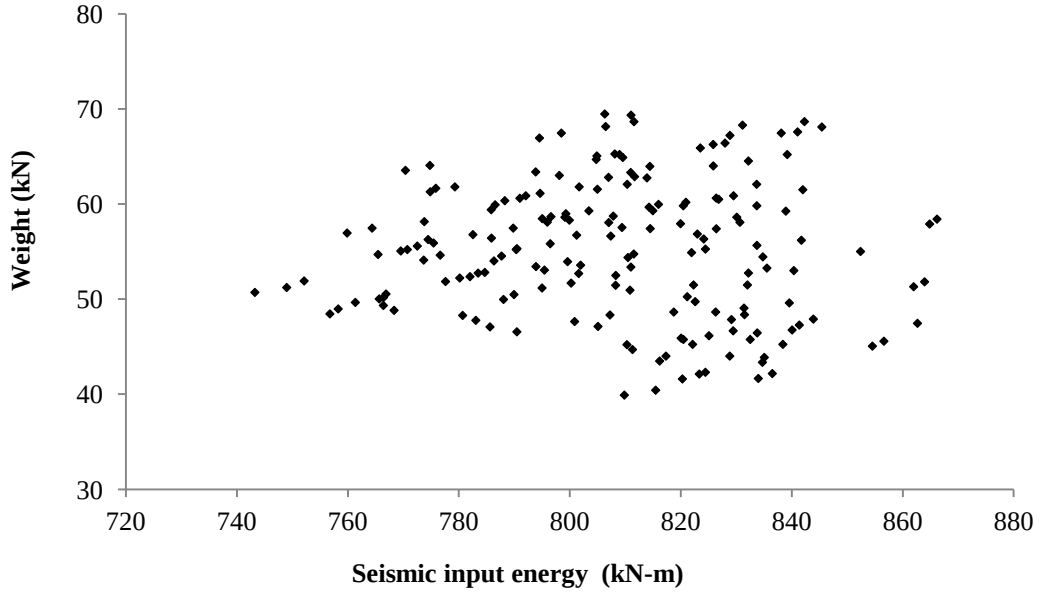

Figure 5-9 Weight (OBJ_1) versus seismic input energy (OBJ_2)

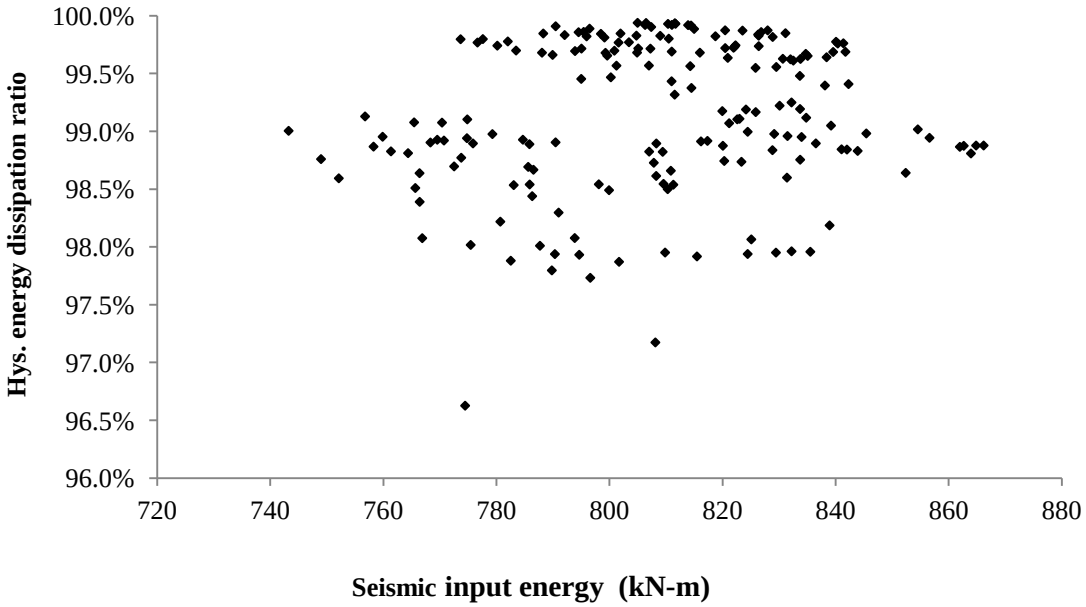

Figure 5-10 Hysteretic energy dissipation ratio (OBJ_3) versus seismic input energy (OBJ_2)

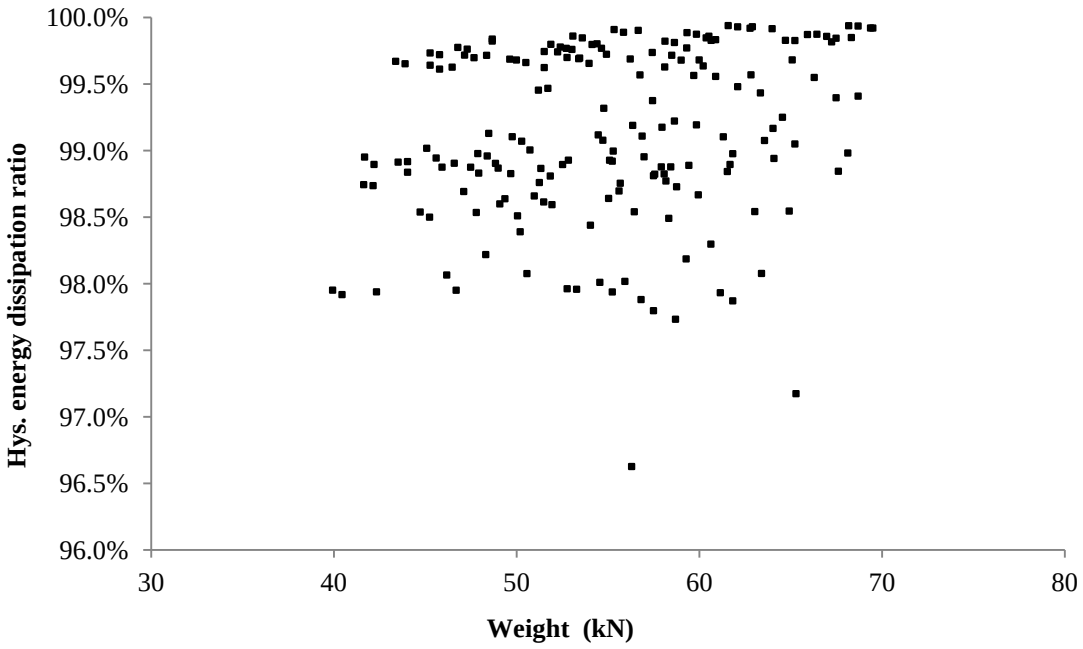

Figure 5-11 Hysteretic energy dissipation ratio (OBJ_3) versus weight (OBJ_1)

As it is shown in Figure 5-7, OBJ_1, structural weight objective, lies between 30 kN and 80 kN; OBJ_2, seismic input energy, ranges from 500 kN-m to 1000 kN-m; OBJ_3, the fuse members' hysteretic energy dissipation ratio, ranges between 0 to 1. Note that those design solutions, which could not survive the ground motion time histories (i.e., the analysis could not converge to a stable deformation state) are not included in the figure. Among them, the feasible solutions are plotted in Figure 5-8.

It is observed (Figure 5-8) that all the feasible design solutions have OBJ_3 values greater than 95%. For easier illustration, the feasible designs in three-dimensional objective space are re-plotted in Figures 5-9 to 5-11 with each figure representing a two-dimensional objective space.

Combining the results of 3 runs gives a set of 18 Pareto-optimal solutions as summarized in Tables 5-4 to 5-6. The following observations can be made from these tables:

1) The fundamental period of the optimal solutions fall in a narrow range from 0.55 sec to 0.70 sec.
2) OBJ_2 value of the Pareto-optimal set ranges from 743 kN-m to 855 kN-m.

3) The optimal solutions show excellent hysteretic energy dissipation performance. Almost 100 per cent hysteretic energy is dissipated by fuse members. Capacity design philosophy is successfully implemented in this example.
4) The value of OBJ_1 displays large dispersion (the difference can be as high as 50%) even among the optimal solutions, let alone among the feasible solutions. This further demonstrates that it is very difficult to obtain even a single-objective (e.g., least-weight) optimal design if traditional trial-and-error method is used.
5) The inter-story drift constraints are far from being active for all optimal solutions. It appears the design of EBFs is more likely governed by the link plastic rotation constraints.
6) For this example, the plastic deformations of non-fuse members are negligible. Though, it may suggest that it is possible to reduce the sectional sizes of columns, braces and beams, the actual implementation will be difficult since the discrete design variables do not allow "fine-tuning" sectional sizes. The fact that the adopted plastic rotation limits for non-fuse members are small also contributes to this phenomenon.

Design results in Table 5-5 shows that it is necessary to introduce some numerical strategies in the GA. For example, design #5 is worse than design #6 in terms of both structural weight and seismic input energy, while it is better in terms of OBJ_3. However, from the practical point of view, the relative hysteretic energy capacities of the two designs are virtually the same. Thus, it is reasonable to say that design #6 is better than design #5. Hence, a rounding-off strategy is conceived in the following

1) Only integer numbers are kept for OBJ_1 and OBJ_2.
2) Only 2 significant digits after decimal point are kept for OBJ_3 by rounding-off.

Following this strategy, a reduced Pareto-optimal set with 8 design solutions are obtained in Table 5-7. Design #18 is the solution with the least weight (OBJ_1 = 40 kN) while design #6 is the design having the minimum seismic input energy (OBJ_2 =743 kN-m). All the Pareto-optimal solutions have a near 100 per cent OBJ_3 values, indicating that the plastic deformations exclusively occur within the links.

Table 5-4 Search results of MGA

Index	Design Number	CL (W)	BE1 (W)	BE2 (W)	BE3 (W)	BR1 (HSS)	BR2 & BR3 (HSS)
1	177	310x107	410x100	410x46	360x33	203x203x13	203x203x9.5
2	369	310x107	410x74	410x60	360x33	203x203x13	203x203x9.5
3	1201	310x79	410x100	410x46	360x33	203x203x13	203x203x9.5
4	1457	310x79	410x74	410x46	360x33	203x203x13	203x203x9.5
5	2225	310x52	410x100	410x46	360x33	203x203x13	203x203x9.5
6	2226	310x52	410x100	410x46	360x33	203x203x13	178x178x8.0
7	2481	310x52	410x74	410x46	360x33	203x203x13	203x203x9.5
8	2482	310x52	410x74	410x46	360x33	203x203x13	178x178x8.0
9	2485	310x52	410x74	410x46	360x33	203x203x9.5	203x203x9.5
10	2486	310x52	410x74	410x46	360x33	203x203x9.5	178x178x8.0
11	2722	310x52	410x60	410x46	360x39	203x203x13	178x178x8.0
12	2738	310x52	410x60	410x46	360x33	203x203x13	178x178x8.0
13	3042	310x52	410x46	360x39	360x39	203x203x13	178x178x8.0
14	3057	310x52	410x46	360x39	360x33	203x203x13	203x203x9.5
15	3058	310x52	410x46	360x39	360x33	203x203x13	178x178x8.0
16	3065	310x52	410x46	360x39	360x33	178x178x8.0	203x203x9.5
17	3066	310x52	410x46	360x39	360x33	178x178x8.0	178x178x8.0
18	3067	310x52	410x46	360x39	360x33	178x178x8.0	178x178x6.4

Table 5-5 Structural response of search results of MGA

Index	OBJ_1 (kN)	OBJ_2 (kN-m)	OBJ_3 (%)	Max. Link Rotation (radians)	Link D/C	Max. Story Drift (radians)	Drift D/C	Fundamental Period (sec)
1	67	795	99.86	6.70%	0.84	0.91%	0.37	0.549
2	66	824	99.87	5.33%	0.67	0.80%	0.32	0.550
3	60	788	99.85	6.70%	0.84	0.93%	0.37	0.556
4	58	796	99.82	6.55%	0.82	0.92%	0.37	0.566
5	54	774	99.80	6.59%	0.82	0.96%	0.38	0.570
6	51	743	99.01	5.82%	0.73	0.96%	0.38	0.597
7	52	778	99.80	6.49%	0.81	0.95%	0.38	0.580
8	48	757	99.13	5.77%	0.72	0.95%	0.38	0.606
9	50	788	99.68	6.59%	0.82	0.95%	0.38	0.597
10	47	790	98.91	5.71%	0.71	0.95%	0.38	0.623
11	48	801	99.70	6.89%	0.86	0.85%	0.34	0.613
12	47	805	99.72	6.54%	0.82	0.82%	0.33	0.616
13	46	820	99.72	6.89%	0.86	0.93%	0.37	0.638
14	49	819	99.82	7.06%	0.88	0.92%	0.37	0.615
15	45	822	99.73	6.56%	0.82	0.90%	0.36	0.641
16	45	855	99.02	6.90%	0.86	0.94%	0.38	0.660
17	42	834	98.95	7.01%	0.88	0.98%	0.39	0.684
18	40	810	97.95	6.95%	0.87	1.04%	0.42	0.703

D/C: Demand/Capacity

Table 5-6 Constraint values of the obtained optimal solutions

Index	Maximum Plastic Rotation					
	Columns (radians)	D/C	Beams (radians)	D/C	Braces (radians)	D/C
1	2.85E-07	0.000	2.19E-04	0.044	1.67E-04	0.017
2	7.69E-09	0.000	1.18E-04	0.024	2.06E-04	0.021
3	4.63E-06	0.001	2.34E-04	0.047	1.74E-04	0.017
4	2.87E-06	0.001	2.46E-04	0.049	1.18E-04	0.012
5	2.78E-04	0.056	2.45E-04	0.049	1.38E-04	0.014
6	2.89E-04	0.058	2.86E-04	0.057	1.86E-03	0.186
7	2.06E-04	0.041	2.36E-04	0.047	1.28E-04	0.013
8	2.22E-04	0.044	2.93E-04	0.059	1.63E-03	0.163
9	1.55E-04	0.031	2.48E-04	0.050	4.28E-04	0.043
10	1.66E-04	0.033	3.11E-04	0.062	1.75E-03	0.175
11	3.44E-05	0.007	1.91E-04	0.038	1.04E-03	0.104
12	1.74E-05	0.003	1.80E-04	0.036	1.16E-03	0.116
13	1.74E-05	0.003	4.01E-04	0.080	4.90E-04	0.049
14	9.04E-06	0.002	3.14E-04	0.063	2.33E-05	0.002
15	1.63E-05	0.003	3.82E-04	0.076	4.87E-04	0.049
16	3.12E-06	0.001	5.65E-04	0.113	2.41E-03	0.241
17	6.53E-06	0.001	4.61E-04	0.092	1.92E-03	0.192
18	1.34E-05	0.003	5.55E-04	0.111	3.65E-03	0.365

D/C: Demand/Capacity

Table 5-7 Reduced Pareto-optimal solutions

Index	OBJ_1 (kN)	OBJ_2 (kN-m)	OBJ_3 (%)	Relative OBJ_1 (f_1)	Relative OBJ_2 (f_2)	Relative OBJ_3 (f_3)	Relative distance (f)	Rank
6	51	743	99	1.00	0.89	0.01	1.339	8
8	48	757	99	0.94	0.91	0.01	1.308	3
10	47	790	98	0.92	0.95	0.02	1.322	4
12	47	805	99	0.92	0.97	0.01	1.335	7
13	46	820	99	0.90	0.98	0.01	1.334	6
15	45	822	99	0.88	0.99	0.01	1.323	5
17	42	834	99	0.82	1.00	0.02	1.296	2
18	40	810	97	0.78	0.97	0.03	1.249	1

In general, it can be said that each Pareto-optimal solution is an equally worthy candidate design for further consideration. For example, design #6 is 27 per cent heavier than design #18, and it absorbs 9 per cent less of seismic input energy. Design #8 is 6 per cent lighter than design #6, but its seismic input energy is only 2 per cent greater than that of design #6. If one considers the difference of OBJ_3 values among the Pareto-optimal set as being negligible, then design #13, #15 and #17 may be regarded as inferior to design #18. In summary, one may choose the final solution based on his/her preference.

A unified decision process may be described in the following. With the values of the three relative objective functions f_1, f_2 and f_3 presented in Table 5-7 (where f_1 and f_2 are obtained by normalizing OBJ_1 and OBJ_2 values by their respective maximum values among the Pareto-optimal set), the reduced Pareto-optimal set is projected into the three-dimensional space shown in Figure 5-12, where each objective is represented by one of the three coordinates of the normalized objective space. It is obvious that, the origin of the coordinate system represents the hypothetical optimum whose objective values are all at their minima, i.e., zeros, simultaneously (though, such a case would never be reached). The overall performance of a Pareto-optimal solution may be evaluated by checking how far the solution is away from the origin. Namely, a measurement f represented by the distance between a design point and the origin is defined as (Alimoradi et al 2007)

$$f = \sqrt{{f_1}^2 + {f_2}^2 + {f_3}^2} \qquad (5\text{-}7)$$

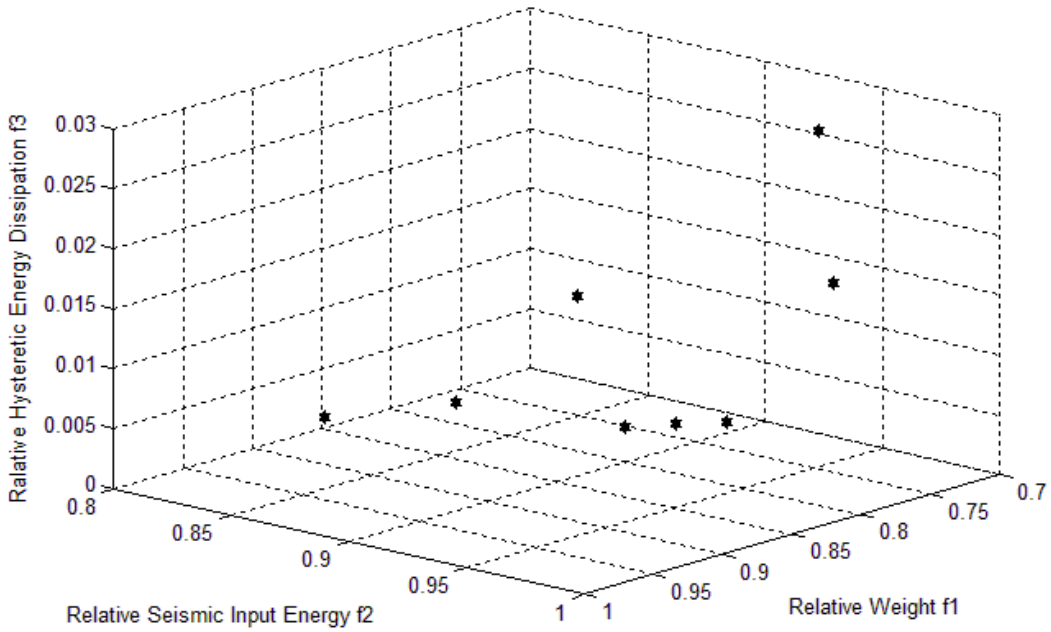

Figure 5-12 Relative objectives of the Pareto-optimal solutions

The obtained Pareto-optimal solutions can then be ranked in regards to the values of *f*. For the minimization problem, the smaller *f* value is, the better the overall performance of the design is. Both the *f* values and the ranks of the Pareto-optimal solutions are included in Table 5-7.

It is observed that other ways in addition to Equation (5-7) are possible in defining *f* value by normalizing OBJ_i (i=1, 2 and 3) values differently. For example, one may include his/her preference through introducing weighting factors in f_i values.

Though it might appear that design objective OBJ_3 plays little role in selecting the final solution among the Pareto-optimal set, OBJ_3 actually played the vital role of driving the MGA to obtain the optimal set (Note that it is possible to have a feasible solution with no yielding of the links).

In the following, detailed results of the nonlinear response history analysis of design #8 are provided to demonstrate the structural behaviours of an obtained optimal design. The ground motion history adopted is "1979 Imperial Valley: El Centro Array #12".

Figures 5-13 and 5-14 show that the maximum roof drift and inter-story drift occur at 10.54 second. Those values are far from limits. Figure 5-15 gives the height-wise distribution of the maximum rotations of the links, where relatively uniform distribution of link rotation is observed. It is the link at floor 3 that experience the maximum rotation of 0.056 radians. Figures 5-16 and 5-17 show that both ends of floor 3 link remain elastic under bending moment during the entire loading history. Figures 5-18 to 5-20 plot the shear versus link rotation angle hysteresis curves. Strain hardening is evident in the hysteresis loops. As expected, the links undergo shear yielding. For the links at floors 2, 3 and roof, the maximum shears 1140 kN, 907 kN and 594 kN correspond to a load level of $1.39V_p$, $1.53V_p$ and $1.39V_p$, respectively [where $V_p = \left(F_{ye}/\sqrt{3}\right)\left(d - 2t_f\right)t_w$]. The load level of the links exceeds the value of $1.3V_p$ specified by CSA-S16 by 7 to 18 per cent, suggesting that the code-specified overstrength factor may be inadequate for this design.

The internal forces of the frame members in the first story are compared with the strength formula of CSA-S16 in Figures 5-21 to 5-23 (Note that the beam-column strength equation shall exclude resistance factor as the load and resistance factors have been already included in the analysis). From the force points of the members, one can observe that the columns and braces are dominated by their compressive forces while the beams are dominated by both axial force and bending moment. All the force points fall within the nominal strength curve, which means the member strengths are satisfactory.

In summary, design #8 has excellent seismic performance under the adopted ground motion.

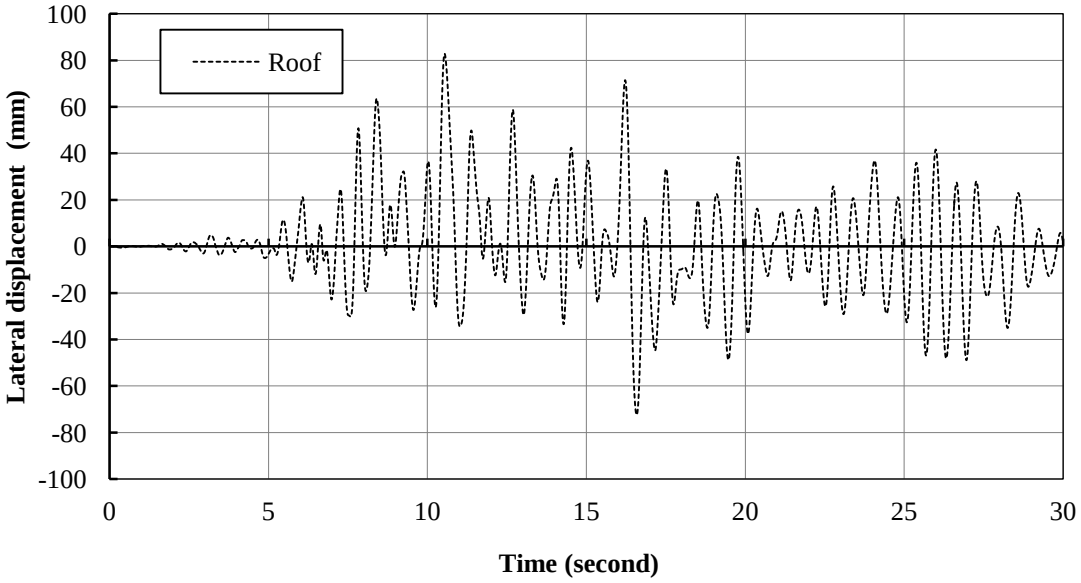

Figure 5-13 Lateral displacement response history

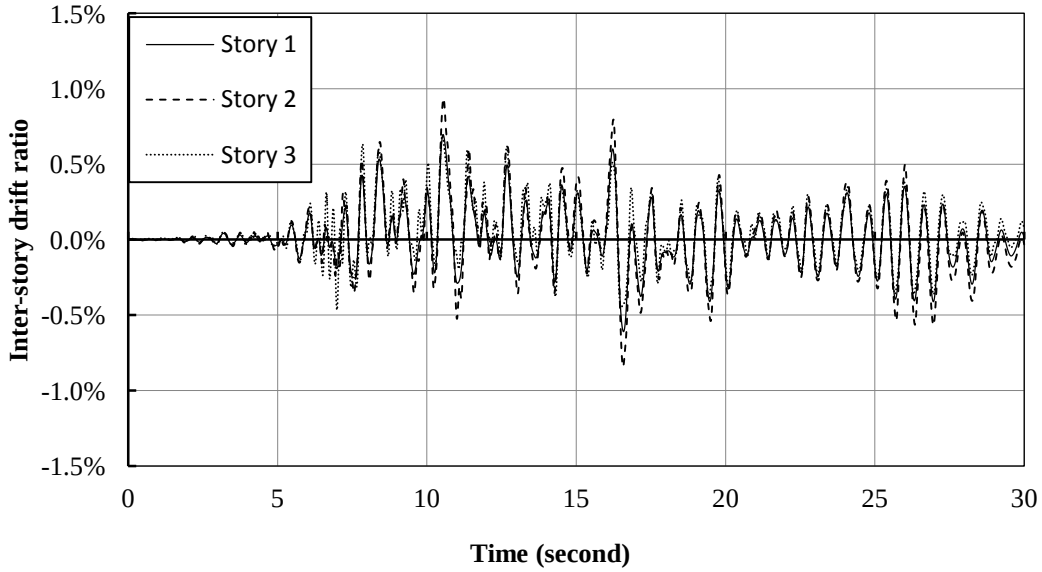

Figure 5-14 Inter-story drift ratio response histories

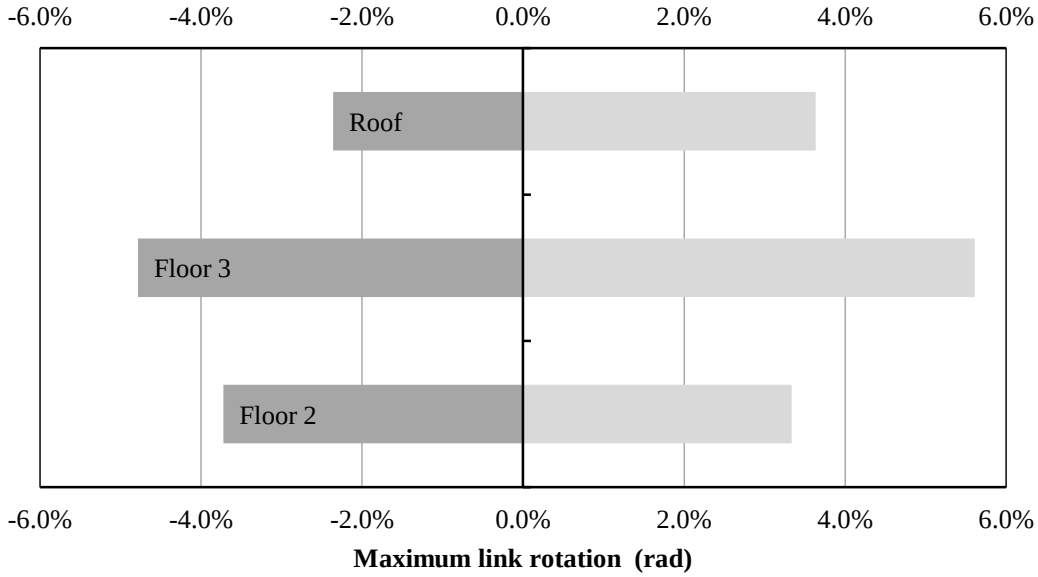

Figure 5-15 Distribution of the maximum link rotation

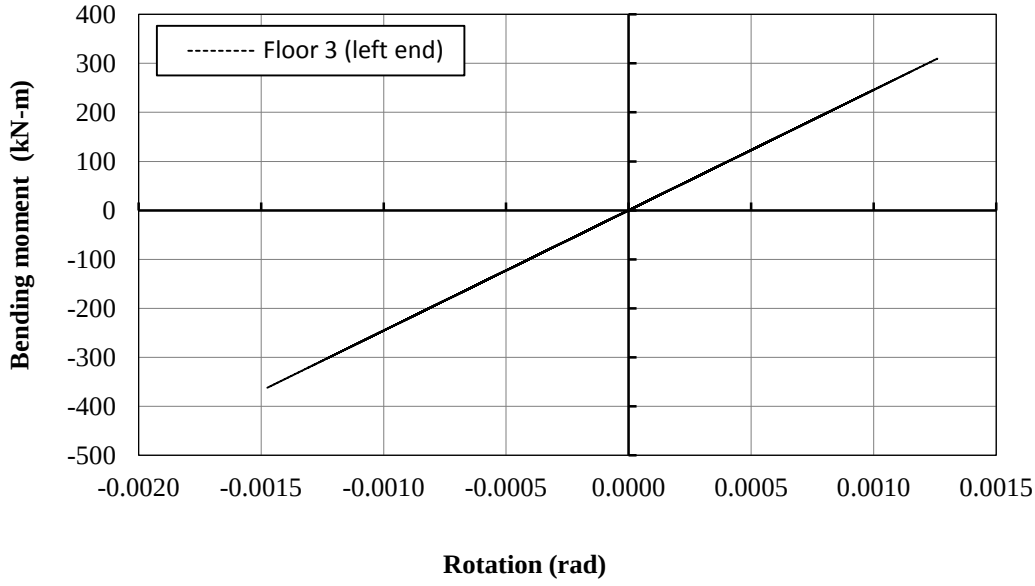

Figure 5-16 Link bending moment versus rotation (Floor 3, left end)

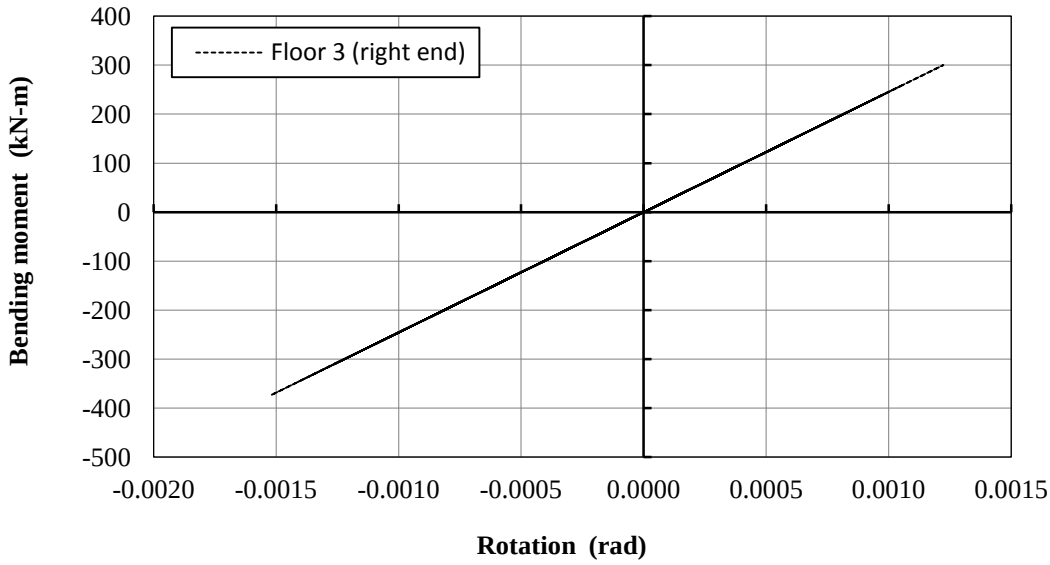

Figure 5-17 Link bending moment versus rotation (Floor 3, right end)

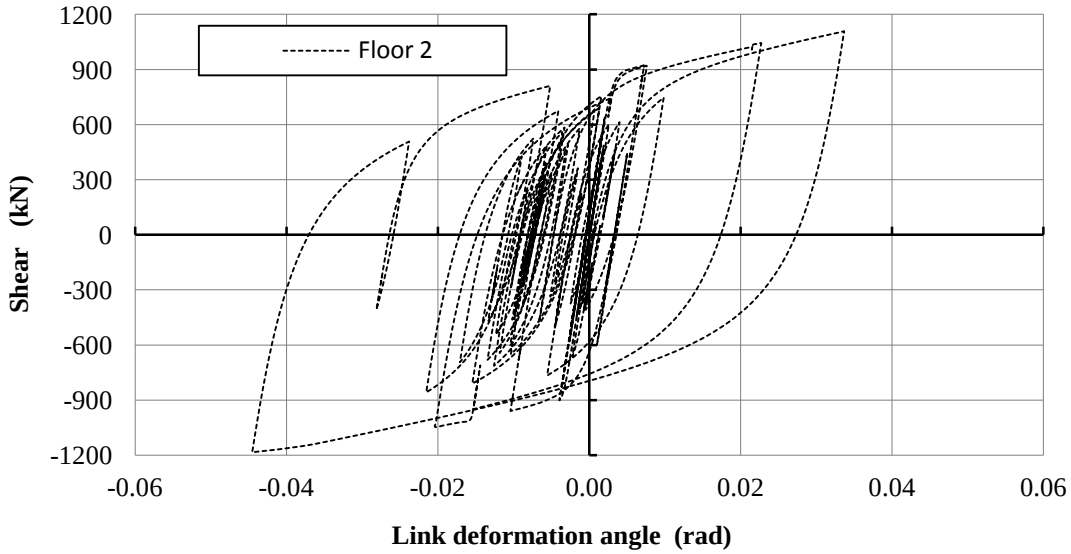

Figure 5-18 Link shear versus rotation hysteresis (Floor 2)

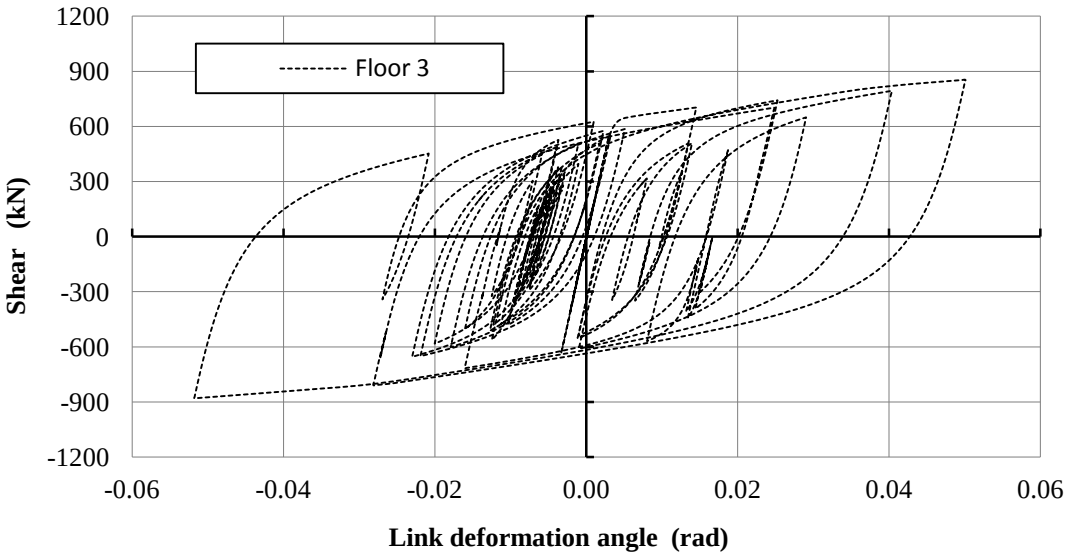

Figure 5-19 Link shear versus rotation hysteresis (Floor 3)

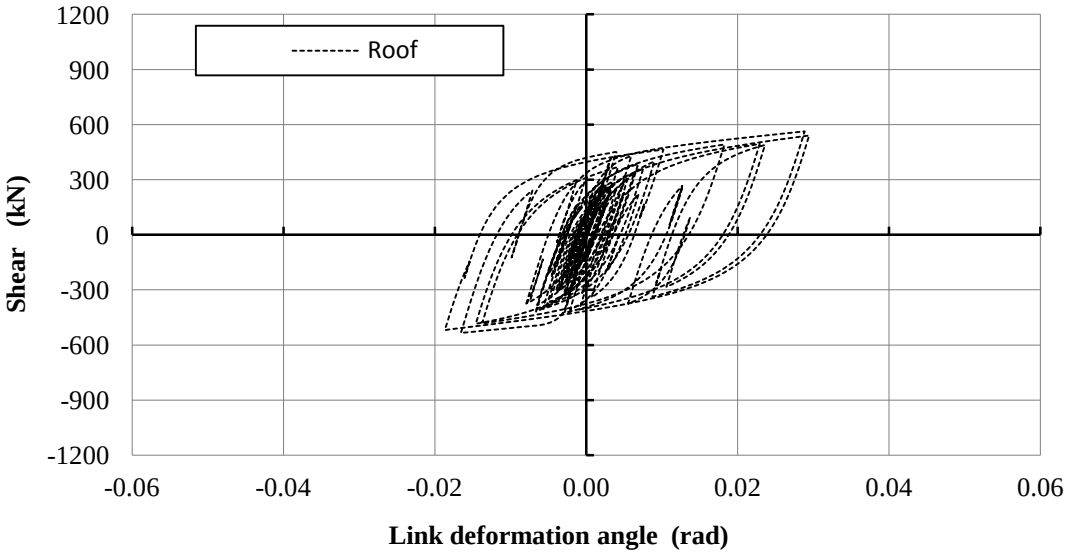

Figure 5-20 Link shear versus rotation hysteresis (Roof)

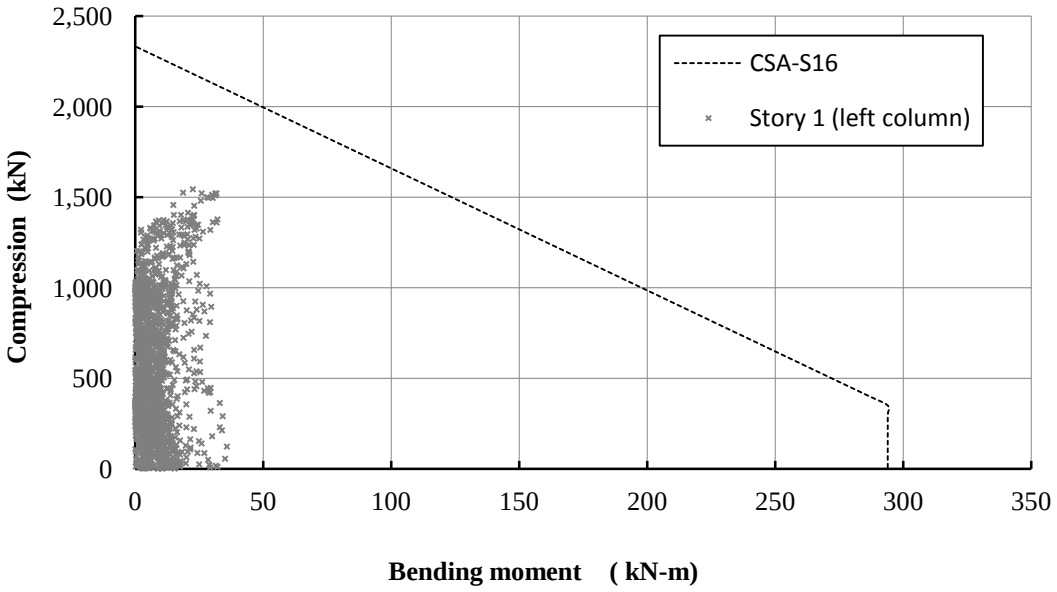

Figure 5-21 Compression versus bending moment (Story 1, left column)

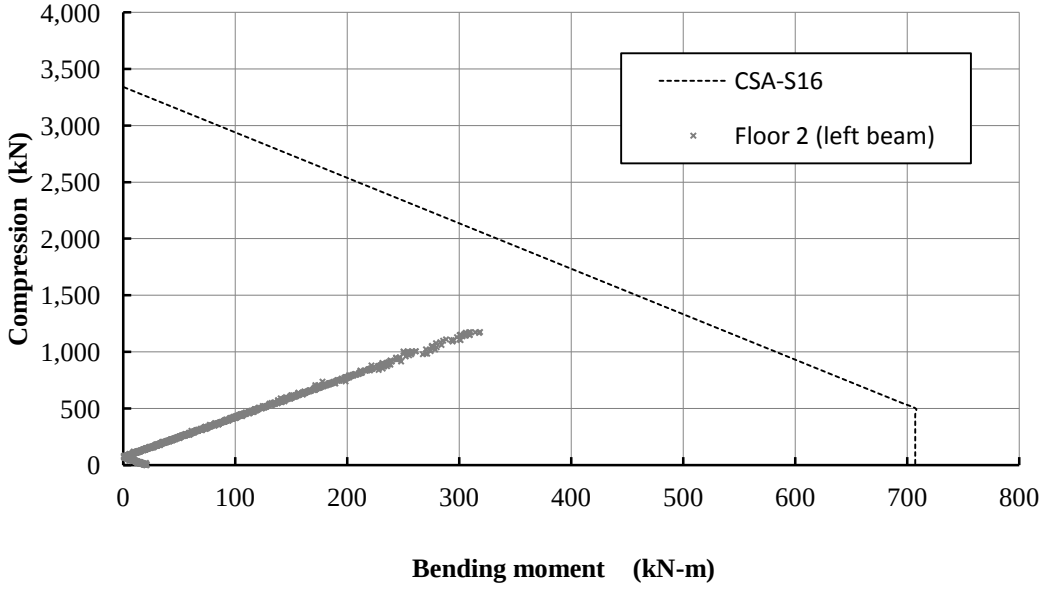

Figure 5-22 Compression versus bending moment (Floor 2, left beam)

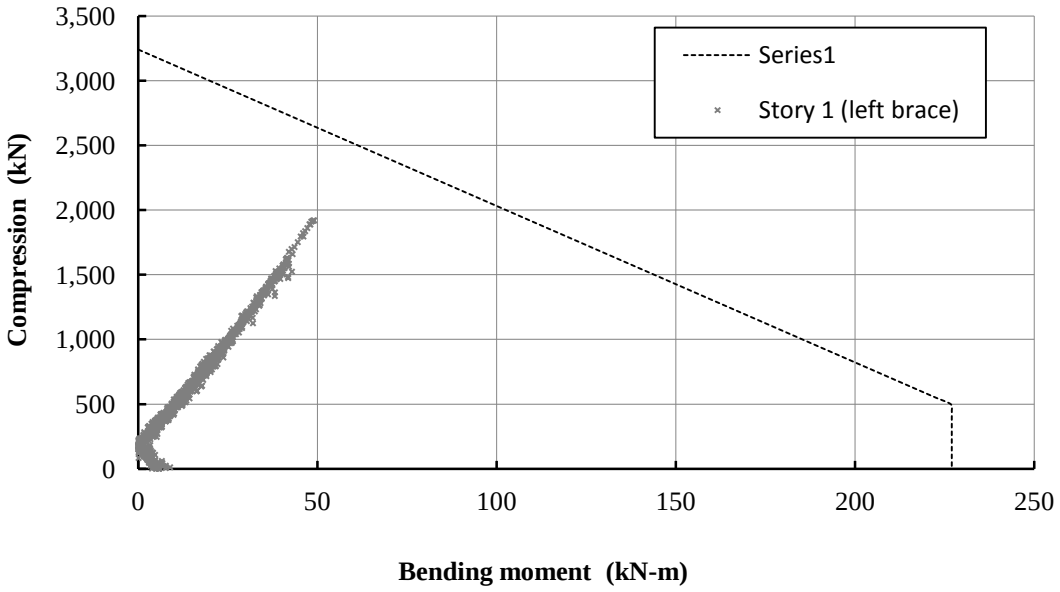

Figure 5-23 Compression versus bending moment (Story 1, left brace)

Chapter 6
Conclusions and Recommendations

6.1 Summary and Conclusions

The major contribution of this research is the development of a design synthesis which is able to automate capacity design of steel building frameworks through the coupling of a nonlinear time history analysis procedure and optimization techniques. Design optimization using dynamic analysis procedures is not a new idea (e.g., Section 1.3). However, to the best knowledge of this author, this research is the first attempt in developing a unified capacity design approach for various steel frameworks.

Specifically, the original contributions of this research are:

1) The development of a numerical technique to compute seismic energies based on the analysis results from an existing nonlinear dynamic analysis procedure (Section 2.1.2). The technique was verified using the educational program NONLIN (Section 2.3).
2) The development of the optimal design formulation, Equations 3-8 to 3-12. In this formulation, the minimum structural cost, the minimum seismic input energy, and the maximum hysteresis energy ratio of fuse members were identified as the design objectives. The cost objective is universal and serves to search for an economical design; the input energy objective aims to reduce the potential earthquake damage to the structure; and the hysteresis objective drives the optimization algorithm to search for design solutions with favorable plastic mechanisms. The choice of using seismic energies as design objectives allows us to capitalize on the adopted analytical tool since only a nonlinear dynamic analysis tool is able to provide both seismic input energy and hysteretic energy. Comparing with displacement or force responses, an energy response has the advantage of not only reflecting the duration of ground motions but also accounting for the cumulative effect of inelastic deformations. The structural design is subjected to strength and deformation constraints. The strength checking is implicitly included in the advanced analysis procedure in which both material and geometrical nonlinearities are considered in the element models. The deformation checking is

explicitly expressed as the imposed plastic deformation limits, in which structural performance levels and member deformation capacities are taken into account. For the design method to be suitable for practical application, the obtained optimal designs are expressed as discrete combinations of steel section shapes.

3) The coupling of a nonlinear dynamic analysis procedure (i.e., OpenSees) with a GA to conduct capacity design automation. A numerical test was conducted to determine the proper population size (Appendix 3.B). Design examples on Moment Resisting Frames and Eccentrically Braced Frames were conducted. The correlation between the hysteretic energy dissipation of fuse members and the strong-column-weak-beam requirement for moment-resisting frames was investigated (Section 4.2). The numerical strategies, such as introducing load and resistance factors in the analysis procedure, grouping of design variables considering a link and the beam outside the link, rounding-off the objective function values, etc., were introduced in the design examples. Also, Equation (5-6) was proposed for the first time by this research as an approximation for computing shear link rotation.

The technical merits of the proposed design synthesis include:

1) The evaluation tool is most sophisticated and accurate, which ensures a better performance of the obtained structure under an earthquake hazard.
2) The design formulation is general. The methodology will greatly simplify the current elastic-analysis-based design practice, in which one-set-of-rules-for-each-type-of-system (CSA 2009) is necessary.
3) The limit state design philosophy is achieved at the structural system level.
4) The design automation tool will help engineers to carry out the capacity design principle without arduous hand calculations. Thus, the design synthesis will greatly assist the application of nonlinear analysis procedures in engineering offices in terms of ease, efficiency and accuracy.

The following specific conclusions can be drawn from this study:

1) The developed optimization model can be used to conduct seismic design of steel frameworks following the capacity design principle. The favorable plastic mechanism is

achieved through forcing the concentration of hysteretic energy dissipation among fuse members.

2) Problem-dependent capacity design requirements, such as strong-column-weak-beam for Moment Resisting Frames, are not included in the design formulation. Therefore, the design method is general and applicable to various types of building frames.
3) The seismic performance factors, such as ductility-related force reduction factor and overstrength-related force reduction factors, which are crucial in elastic-analysis-based design methods, are no longer needed in inelastic-analysis-based design methods. Thus, the approximations in obtaining these factors are completely eliminated in an inelastic-analysis-based design method, which allows us to obtain design solutions with better earthquake resistance behavior.
4) The Multi-objective Genetic Algorithm tool provided in MATLAB works well for the proposed design formulation, though more work needs to be done in future study to improve its computational efficiency
5) For a design problem, the number of feasible design solutions is generally large, and the structural weights of the feasible designs spread over a wide range (this is mainly because a larger structural weight or stiffness also attracts greater earthquake loads). The fact indicates that without a design optimization tool it is not easy to obtain an economical design when a nonlinear dynamic analysis procedure is adopted as the evaluating tool.
6) The distance between a Pareto-optimal solution point and the origin of the design objective space is an overall performance index for trade-off analysing design decisions to come to a final design.
7) It appears it is generally necessary for the beams outside links to be reinforced with flange cover plates in order to satisfy the plastic rotation limits of the beams.

Overall, it can be concluded that the proposed nonlinear-analysis-based design optimization methodology holds much promise as the base for practical and powerful tool for the capacity design of steel building frameworks under strong earthquake ground motions. It extends and improves the current design approaches for seismic design of steel buildings.

6.2 Recommendations for Future Research

It is recommended that the following future research be pursued to extend or enhance the capability of the proposed optimal design.

Panel-Zone and Joint Modeling

The analytical models of the SFRSs in this thesis assumed that steel member connections were either perfectly pinned or fixed. However, plastic deformations of connection panel-zones, if they exist, can significantly impact the overall performance of a steel building framework. It is recommended that advanced panel-zone and joint models be included to account for connection behaviour in the future.

Three-Dimensional Structures

This research employed planar frame models only. To account for potential torsional effects arising from the irregularity of building structures, it is desirable to extend the current work to three-dimensional structural models.

Parallel Computing

The adopted Multi-objective Genetic Algorithm was very computational demanding. Although this research is carried out on a regular personal computer system, the extension to an advanced parallel computing system can be highly expected in the future.

Concrete Buildings

The proposed optimal design method is generally applicable to various types of Seismic Force Resisting Systems. Concrete building structures can be easily included in the framework of the proposed design method.

Parametric Study

A systematic parametric study on how the values of the plastic deformation limits impact design results needs to be conducted. The parametric study might provide insights on how to differentiate the so-called “ductile moment-resisting frames” from “limited-ductility moment resisting frames” for inelastic-analysis-based design methods.

References

AISC (2005a). Seismic provisions for structural steel buildings (ANSI/AISC 341-05) (including supplement no. 1) (ANSI/AISC 341s1-05). Chicago, IL: American Institute of Steel Construction.

AISC (2005b). Specification for structural steel buildings (ANSI/AISC 360-05). Chicago, IL: American Institute of Steel Construction.

ASCE (2007). Seismic Rehabilitation of existing Buildings (ASCE/SEI 41-06). Reston, Virginia: American Society of Civil Engineers

Akbas, B., Shen, J., and Hao, H. (2001). Energy approach in performance-based seismic design of steel moment resisting frames for basic safety objective. Structural Design of Tall Buildings, 10(3), 193-217.

Alimoradi, A., Pezeshk, S., and Foley, C. M. (2007). Probabilistic performance-based optimal design of steel moment-resisting frames II: Applications. Journal of Structural Engineering, 133(6), 767-776.

Arora, J. S. (2007). Optimization of structural and mechanical systems. Hackensack, NJ: World Scientific.

Austin, M. A., Pister, K. S., and Mahin, S. A. (1986). PROBABILISTIC LIMIT STATES DESIGN OF MOMENT-RESISTANT FRAMES UNDER SEISMIC LOADING. Recent Developments in Structural Optimization. Proceedings of a Session at Structures Congress '86. 1-16.

Austin, M. A., Pister, K. S., and Mahin, S. A. (1987). Probabilistic design of moment-resistant frames under seismic loading. Journal of Structural Engineering, 113(8), 1660-1677.

Balling, R. J., Pister, K. S., and Ciampi, V. (1983). Optimal seismic-resistant design of a planar steel frame. Earthquake Engineering & Structural Dynamics, 11(4), 541-556.

Bruneau, M., Uang, C., and Whittaker, A. S. (1998). Ductile design of steel structures. New York: McGraw-Hill.

Chan, C., Grierson, D. E., and Sherbourne, A. N. (1995). Automatic optimal design of tall steel building frameworks. Journal of Structural Engineering, 121(5), 838-847.

Charney, Finley A., and Barngrover, Brian (2004). NONLIN: Software for Earthquake Engineering Education. Structures 2004. ASCE.

Cheng, F. Y., and Juang, D. S. (1989). Recursive optimization for seismic steel frames. Journal of Structural Engineering, 115(2), 445-466.

Chopra, A. K. (2007). Dynamics of structures: Theory and applications to earthquake engineering (3rd edition). Prentice Hall.

Chou, C., and Uang, C. (2003). A procedure for evaluating seismic energy demand of framed structures. Earthquake Engineering and Structural Dynamics, 32(2), 229-244.

CISC (2010). Handbook of steel construction (10th edition). Willowdale, Ontario. Canadian Institute of Steel Construction.

Crisfield, M. A. (1991). Non-linear finite element analysis of solids and structures. John Wiley & Sons, Chichester, U.K.

CSA (2009). Limit States Design of Steel Structures (CAN/CSA-S16-09). Mississauga, ON, Canada. Canadian Standards Association.

Engelhardt, M. D., and Popov, E. P. (1989). On design of eccentrically braced frames. Earthquake Spectra, 5(3), 495-511.

FEMA (2004a). NEHRP recommended provisions for seismic regulations for new buildings and other structures (FEMA 450) part 1 - provisions. Washington, DC, USA: Federal Emergency Management Agency, BSSC.

FEMA (2004b). NEHRP recommended provisions for seismic regulations for new buildings and other structures (FEMA 450) part 2 - commentary. Washington, DC, USA: Federal Emergency Management Agency, BSSC.

FEMA (2009). Quantification of building seismic performance factors (FEMA P695). Washington, DC, USA: Federal Emergency Management Agency, ATC.

Filiatrault, A., Leger, P., and Tinawi, R. (1994). Computation of seismic energy in inelastic structures. Engineering Structures, 16(6), 425-436.

Filippou, Filip C. and Fenves, Gregory L. (2004) Methods of Analysis for Earthquake-Resistant Structures. In book: Earthquake Engineering: From Engineering Seismology to Performance-Based Engineering, Edited by Yousef Bozorgnia and Vitelmo V. Bertero. CRC Press 2004.

Foley, C. M. (2002). Optimized performance-based design for buildings. Recent Advances in Optimal Structural Design, 169-240.

Foley, C. M., and Schinler, D. (2003). Automated design of steel frames using advanced analysis and object-oriented evolutionary computation. J. Structural Engineering, 129(5), 648-660.

Foley, C. M., Pezeshk, S., and Alimoradi, A. (2007). Probabilistic performance-based optimal design of steel moment-resisting frames I: Formulation. Journal of Structural Engineering, 133(6), 757-766.

Gong, Y., Xu, L., and Grierson, D. E. (2005). Performance-based design sensitivity analysis of steel moment frames under earthquake loading. International Journal for Numerical Methods in Engineering, 63(9), 1229-1249.

Gong, Y., Xue, Y., Xu L., and Grierson, D.E. (2012). Energy-based design optimization of steel building frameworks using nonlinear response history analysis. Journal of Constructional Steel Research, 2012, 68(1):43-50.

Grierson, D. E. (1996). Conceptual design optimization of structural systems. Proceedings of the 1996 12th Conference on Analysis and Computation, April 15,1996 - April 18, 99-110.

Grierson, D. E. (2009). Structural Optimization, CIVE 700 Course Notes, Department of Civil Engineering, University of Waterloo, Ontario, Canada, 2009.

Grierson, D. E., and Chiu, T.C.W. (1984). Optimal synthesis of frameworks under multilevel performance constraints. Computers and Structures, 18(5), 889-98.

Haftka, R. T., and Gürdal, Z. (1992). Elements of structural optimization (3rd revised and expanded edition). Dordrecht: Kluwer Academic Publishers.

Housner, George W. (1956). Limit Design of Structures to Resist Earthquakes. Proceedings of World Conference on Earthquake Engineering, 1st, Berkeley, California, 1956.

Kramer, G. J. E., and Grierson, D. E. (1987). OPTIMAL DESIGN OF STRUCTURES UNDER DYNAMIC LOADS. Computer Applications in Structural Engineering, 326-341.

Leger, M., and Dussault, S. (1992). Seismic-energy dissipation in MDOF structures. Journal of Structural Engineering, 118(5), 1251-1269.

Koboevic, S., and Redwood, R. (1997). Design and seismic Response of Shear Critical Eccentrically Braced Frames. Canadian Journal of Civil Engineering, 24: 761-771.

Liu, M., Burns, S. A., and Wen, Y. K. (2003). Optimal seismic design of steel frame buildings based on life cycle cost considerations, Earthquake Engineering and Structural Dynamics, 32(9) 1313-1332.

Liu, M., Burns, S. A., and Wen, Y. K. (2006). Genetic algorithm based construction-conscious minimum weight design of seismic steel moment-resisting frames. Journal of Structural Engineering, 132(1), 50-58.

Malley, J. O., and Popov E. P. (1984). Shear links in Eccentrically Braced Frames. Journal of Structural Engineering. ASCE, 110(9): 2275-2295

Mansour, Nabil, Christopoulos, Constantin, and Tremblay, Robert (2009) Experimental performance of full-scale eccentrically braced frames with replaceable shear links. In book: Behaviour of Steel Structures in Seismic Areas, proceedings STESSA 2009, Edited by Richard Sause, Federico M. Mazzolani and James M. Ricles. CRC Press 2009.

Memari, A. M., and Madhkhan, M. (1999). Optimal design of steel frames subject to gravity and seismic codes' prescribed lateral forces. Structural Optimization, 18(1), 56-66.

Menegotto, M., and Pinto P.E. (1973). Method of analysis for cyclically loaded reinforced concrete plane frames including changes in geometry and non-elastic behaviour of elements under combined normal force and bending. In: Proceedings of IABSE symposium on resistance and ultimate deformability of structures acted on by well defined repeated loads, Lisbon; 1973. p. 15–22.

Neuenhofer, Ansgar, and Filippou, Filip C. (1997). Evaluation of Nonlinear Frame Finite-Element Models. Journal of Structural Engineering. ASCE, 123(7), 958-966.

Neuenhofer, Ansgar, and Filippou, Filip C. (1998). Geometrically Nonlinear Flexibility-Based Frame Element. Journal of Structural Engineering. ASCE, 124(6), 704-711.

NRCC (2010). National building code of Canada 2010. Ottawa: National Research Council of Canada.

NRCC (2006). User's guide - NBC 2005 structural commentaries (part 4 of division B). Ottawa: National Research Council of Canada.

OpenSees (2008). Open System for Earthquake Engineering Simulation, Pacific Earthquake Engineering Research Center, Berkeley, Calif., < http://opensees.berkeley.edu>.

Park, Kwang-Wook, and Grierson Donald E. (1999). Pareto-optimal conceptual design of the structural layout of buildings using a multicriteria genetic algorithm. Computer-Aided Civil and infrastructure Engineering, May 1999, v14, n3, p163-170.

Paulay, T. and Priestley, M. J. N. (1992). Seismic Design of Reinforced Concrete and Masonry Buildings, Wiley Interscience, New York.

Paz, M. (1991). Structural dynamics: Theory and computation (3rd edition). New York: Van Nostrand Reinhold.

Philpot, Timothy A. (2008). Mechanics of Materials: An Integrated Learning System. John Wiley & Sons, Inc.

PEER (2008). Pacific Earthquake Engineering Research Center, < www.peer.berkeley.edu>.

Pires, J. A. (1994). Statistics of cumulative damage parameters based on hysteretic energy dissipated. Nuclear Engineering and Design 147 (1994), 141-155.

Popov, E. P., Amin, Navin R., Louie, Jason J. C., and Stephen, Roy M. (1986). Cyclic Behavior of Large Beam-Column Assembles, Engineering Journal, 23, 9-23.

Popov, E. P., and Engelhardt, Michael D. (1988). Seismic eccentrically braced frame. Journal of Constructional Steel Research, 10, 321-354.

Popov, E. P., Engelhardt, Michael D., and Ricles, James M. (1990). Eccentrically braced frames: US practice. Engineering Journal. 26, 66-80.

Richards, P. W. and Uang, C-M. (2006). Testing protocol for short links in eccentrically-braced frames. Journal of Structural Engineering, ASCE, 132(8): 1183-1191

Ricles, J. M., and Popov, E. P. (1994). Inelastic Link Element for EBF Seismic Analysis. Journal of Structural Engineering, ASCE, 120(2): 441-463

Ramadan, T. and Ghobarah, A. (1995). Analytical model for shear-link behavior. Journal of Structural Engineering, 121(11), 1574-1580.

Saatcioglu, M., and Humar, J. (2003). Dynamic analysis of buildings for earthquake-resistant design. Canadian Journal of Civil Engineering, 30(2), 338-359

SEAOC Seismology Committee (1975). Recommended lateral force requirements and commentary. San Francisco, California: Structural Engineers Association of California.

Spacone, E., Filippou, F. C., and Taucer, F. F. (1996). Fiber beam-column model for non-linear analysis of RC frames: Part I formulation, Earthquake Engineering and Structural Dynamics.25, 711-725

Scott, Michael H., and Fenves, Gregory L. (2006). Plastic Hinge Integration Methods for Force-based Beam-Column Elements. Journal of Structural Engineering, 132(2), 244-252.

Scott, Michael H., Fenves, Gregory L., McKenna, Frank, and Filippou, Filip C. (2008). Software Patterns for Nonlinear Beam-Column Models. Journal of Structural Engineering, 134(4), 562-571.

Takewaki, I., Conte, J. P., Mahin, S. A., and Pister, K. S. (1991). Probabilistic multi-objective optimal design of seismic-resistant braced steel frames using ARMA models. Computers and Structures, 41(4), 687-707.

Tembulkar, J. M., and Nau, J. M. (1987). Inelastic Modeling and Seismic Energy Dissipation. Journal of Structural Engineering, 113(6), 1373-1377.

The MathWorks Inc. (2009). MATLAB the language of technical computing (version 7.8), <www.mathworks.com>.

Tso, W. K., Zhu, T. J., and Heidebrecht, A. C. (1993). Seismic energy demands on reinforced concrete moment-resisting frames. Earthquake Engineering and Structural Dynamics, 22(6), 533-545.

Truman, K. Z., and Cheng, F. Y. (1989). Optimum assessment of irregular three-dimensional seismic buildings. Journal of Structural Engineering, 116(12), 3324-3337.

Uang, C-M, and Bertero, V. V. (1990). Evaluation of seismic energy in structures. Earthquake Engineering and Structural Dynamics (19) 77-90.

Uriz, Patix, Filippou, Filip C., and Mahin, Stephen A. (2008). Model for cyclic inelastic buckling of steel braces, Journal of Structural Engineering. ASCE, 134(4), 619-628.

Wong, K. K. F., and Wang, Y. (2001). Energy-based damage assessment on structures during earthquakes. Structural Design of Tall Buildings, 10(2), 135-154.

Xu, L., and Grierson, D. E. (1993). Computer-automated design of semi-rigid steel frameworks. Journal of Structural Engineering, 119(6), 1740-1760.

Zahrah, T. F., and Hall, W. J. (1984). EARTHQUAKE ENERGY ABSORPTION IN SDOF STRUCTURES. Journal of Structural Engineering, 110(8), 1757-1772.

Zou, X. K., and Chan, C. (2005). Optimal seismic performance-based design of reinforced concrete buildings using nonlinear pushover analysis. Engineering Structures, 27(8), 1289-1302.

Appendices

Appendix 2.A

Iterative Algorithm for Element State Determination

An iterative algorithm at the element level (Spacone et al 1996) is employed to approach the element force state with respect to the updated deformation state (i.e., the displacement corresponding to $\Delta\{u\}^{(i)}$ during the Newton-Raphson iterations) by checking the convergency criteria for the residual element deformations. The first iteration step j=1 (which is within the i^{th} Newton-Raphson iteration) begins with the element deformation increment $\Delta \boldsymbol{V}^{i}$(which is related to the displacement state $\Delta\{u\}^{(i)}$ of the MDOF system)**,** the initial element stiffness matrix $\left[\boldsymbol{F}^{j=0}\right]^{-1} = \left[\boldsymbol{F}^{i-1}\right]^{-1}$, and the initial section stiffness matrix $\left[\boldsymbol{f}_s{}^{j=0}\right]^{-1} = \left[\boldsymbol{f}_s{}^{i-1}\right]^{-1}$ (which is evaluated based on the element state of the (i-1)$^{\text{th}}$ Newton-Raphson iteration), the corresponding element force increment vector $\Delta \boldsymbol{W}^{j=1}$, the section force increment vector $\Delta \boldsymbol{S}^{j=1}$, and the first approximation of the section deformation increment $\Delta \boldsymbol{D}^{\boldsymbol{j=1}}$ are computed from Equation (2 - 71), Equation (2 - 67), and Equation (2 - 70), respectively,

$$\Delta \boldsymbol{W}^{j=1} = \left[\boldsymbol{F}^{j=0}\right]^{-1} \Delta \boldsymbol{V}^{i} \qquad \text{(2.A - 1)}$$

$$\Delta \boldsymbol{S}^{j=1} = \boldsymbol{a}(x)\, \Delta \boldsymbol{W}^{j=1} \qquad \text{(2.A - 2)}$$

$$\Delta \boldsymbol{D}^{j=1} = \boldsymbol{f}_s{}^{j=0}\, \Delta \boldsymbol{S}^{j=1} \qquad \text{(2.A - 3)}$$

The first approximation of section deformation and force are updated by $\boldsymbol{D}^{j=1} = \boldsymbol{D}^{i-1} + \Delta \boldsymbol{D}^{j=1}$and $\boldsymbol{S}^{j=1} = \boldsymbol{S}^{i-1} + \Delta \boldsymbol{S}^{j=1}$, respectively. On the other hand, the section resisting force vector $\boldsymbol{S}_R{}^{j=1}$and flexibility matrix $\boldsymbol{f}_s{}^{j=1}$ are evaluated with respect to $\boldsymbol{D}^{j=1}$ according to the general numerical integration methods. Then the unbalanced section force $\boldsymbol{S}_U{}^{j=1}$ and the residual section deformation $\boldsymbol{r}^{j=1}$ are computed as follows,

$$\boldsymbol{S}_U{}^{j=1} = \boldsymbol{S}^{j=1} - \boldsymbol{S}_R{}^{j=1} \tag{2.A - 4}$$

$$\boldsymbol{r}^{j=1} = \boldsymbol{f}_s{}^{j=1}\, \boldsymbol{S}_U{}^{j=1} \tag{2.A - 5}$$

According to Equation (2 - 69), the residual element deformation vector can be expressed as

$$\boldsymbol{V}_r{}^{\boldsymbol{j=1}} = \int_0^l \boldsymbol{a}^T\, \boldsymbol{r}^{j=1}\, dx \tag{2.A - 6}$$

To this end, the first iteration j=1 is completed with the residual deformation $\boldsymbol{V}_r{}^{\boldsymbol{j=1}}$ and $\boldsymbol{r}^{j=1}$ existing within the element. To satisfy the compatibility at the element end nodes, a force vector $\Delta\boldsymbol{W}^{j=2} = -\left[\boldsymbol{F}^{j=1}\right]^{-1} \boldsymbol{V}_r{}^{j=1}$ should be applied at the element ends (where$\left[\boldsymbol{F}^{j=1}\right]^{-1}$is the element stiffness matrix obtained from the first iteration j=1 deformation state). The iteration process from Equation (2.A – 2) to Equation (2.A – 6) continues until the selected element convergence criterion is satisfied. The element force state (which accounts for the nonlinear property through the stress integration over cross sections) with respect to the element deformation increment $\Delta\boldsymbol{V}^i$ is determined at the end of the iteration.

According to the iterative procedure of the force-based element state determination, the element equilibrium is always satisfied (even in the range of nonlinear material response) while the force-deformation relation is only satisfied with a specific tolerance (i.e., the residual deformation $\boldsymbol{V}_r{}^j$ and $\boldsymbol{r}^j$) when convergency is achieved.

Appendix 3.A

Acceptance Criteria of Steel Frame Members

The axial force of a frame member has a large impact on its plastic rotation capacity. In accordance with ASCE/SEI 41-06 (ASCE 2007), the specified allowable plastic rotations $\varphi_{k,0}$for a steel frame member under bending moment is

For zero axial force, i.e., $P/P_n = 0$

$$\frac{b_f}{2t_f} \leq \frac{52}{\sqrt{F_{ye}}} \; and \; \frac{h}{t_w} \leq \frac{418}{\sqrt{F_{ye}}} : \quad \varphi_{k,0} = 8\,\theta_y \tag{3.A - 1}$$

$$\frac{b_f}{2t_f} \geq \frac{65}{\sqrt{F_{ye}}} \; or \; \frac{h}{t_w} \geq \frac{640}{\sqrt{F_{ye}}} : \quad \varphi_{k,0} = 3\,\theta_y \tag{3.A - 2}$$

For $0 < P/P_n < 0.2$

$$\frac{b_f}{2t_f} \leq \frac{52}{\sqrt{F_{ye}}} \; and \; \frac{h}{t_w} \leq \frac{300}{\sqrt{F_{ye}}} : \quad \varphi_{k,0} = 8\,\theta_y \tag{3.A - 3}$$

$$\frac{b_f}{2t_f} \geq \frac{65}{\sqrt{F_{ye}}} \; or \; \frac{h}{t_w} \geq \frac{460}{\sqrt{F_{ye}}} : \quad \varphi_{k,0} = 3\,\theta_y \tag{3.A - 4}$$

For $0.2 \leq P/P_n \leq 0.5$

$$\frac{b_f}{2t_f} \leq \frac{52}{\sqrt{F_{ye}}} \; and \; \frac{h}{t_w} \leq \frac{260}{\sqrt{F_{ye}}} : \quad \varphi_{k,0} = 11\left(1 - \frac{5}{3}\frac{P}{P_n}\right)\theta_y \tag{3.A - 5}$$

$$\frac{b_f}{2t_f} \geq \frac{65}{\sqrt{F_{ye}}} \; or \; \frac{h}{t_w} \geq \frac{400}{\sqrt{F_{ye}}} : \quad \varphi_{k,0} = 0.8\,\theta_y \tag{3.A - 6}$$

For $0.5 < P/P_n \leq 1.0$, the expected ductile behaviour of the column under a bending moment cannot be guaranteed. Thus, its plastic rotation capacity is taken as zero (or a small value determined using interpolation).

In the above equations, b_f, t_f are the flange width and thickness, respectively; and h, t_w are the web height and thickness, respectively; F_{ye} is the expected steel yield stress (in customary unit ksi); P, P_n are the calculated axial compressive force and the corresponding nominal axial compressive strength, respectively; θ_y (as shown in Figure 3-1) is the yield rotation of the corresponding structural members and is computed as

$$\theta_y = \frac{ZF_{ye}L}{6\,EI}\,(1 - \frac{P}{P_{ye}}) \qquad \text{(3.A - 7)}$$

where L and I are the length and cross-sectional moment of inertia of the frame member, respectively; P_{ye} is the expected axial yield force of the member, and $P_{ye} = A_g\,F_{ye}$.

The expected material strength is obtained by multiplying its specified strength by an appropriate factor. For example, CSA-S16-09 adopts $F_{ye} = 1.10\,F_y$.

With the assumption that out-of-plane buckling failure is prevented, the in-plane nominal compressive strength P_n can be determined using the equation from either AISC 360-05 (AISC 2005b) or CSA-S16-09 (CSA 2009). Herein, CSA-S16-09 equation is adopted due to its simplicity,

$$P_n = AF_y\,(1 + 2\,\lambda^{2n})^{-1/n} \qquad \text{(3.A - 8)}$$

$$\lambda = \sqrt{F_y/F_e} \qquad \text{(3.A - 9)}$$

$$F_e = \pi^2 E/(KL/r)^2 \qquad \text{(3.A - 10)}$$

where n = 1.34 for hot-rolled, fabricated structural sections manufactured in accordance with CSA G40.20, Class C (cold-formed non-stress-relieved).

Appendix 3.B

Minimum Weight Seismic Design of a Steel Portal Frame

A minimum weight seismic design problem of a steel portal frame is employed to test the proposed optimization design methodology. The capability of using nonlinear time-history analysis in practical design procedure is illustrated. The single objective optimal design problem is solved by using a Genetic Algorithm.

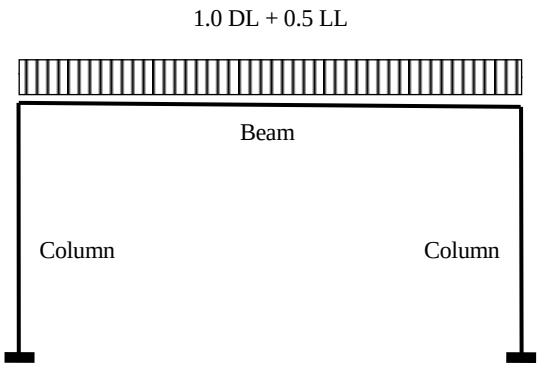

Figure 3.B -1 Side view of the steel portal frame

The portal frame shown in Figure 3.B -1 is 30 ft (9.14 m) wide (centerline dimensions) and 13 ft (3.96 m) high. The frame has rigid beam-to-column connections, with all column bases fixed at the ground level. Only two design variables, x_1 (column size) and x_2 (beam size) are considered in this design problem. The columns use a 50 ksi (345 MPa) steel wide-flange section, while the beams use a 36 ksi (248 MPa) steel wide-flange section. The linear dead and live loads for the roof beam are taken as 2.6 kip/ft (37.2 kN/m) and 0.6 kip/ft (8.8kN/m), respectively. The mass used to compute the seismic load is

$$mass = (1.0\ DL + 0.5\ LL)/g \qquad (3.B - 1)$$

where *DL* and *LL* are the dead and live loads, respectively; and g = 386 in/sec^2 (9.8 m/sec^2).

The earthquake ground motion, Northridge 01/17/94 1231, Santa Monica 090, available from the Pacific Earthquake Engineering Research strong motion database (PEER 2008), is adopted as the earthquake hazard for nonlinear time-history analysis. The portal frame is assumed to be constructed at a location in Vancouver, British Columbia, Canada. To be compatible with the design spectrum specified by NBCC 2010 for Vancouver, a scale factor of 3.2 is used to adjust the ground motion.

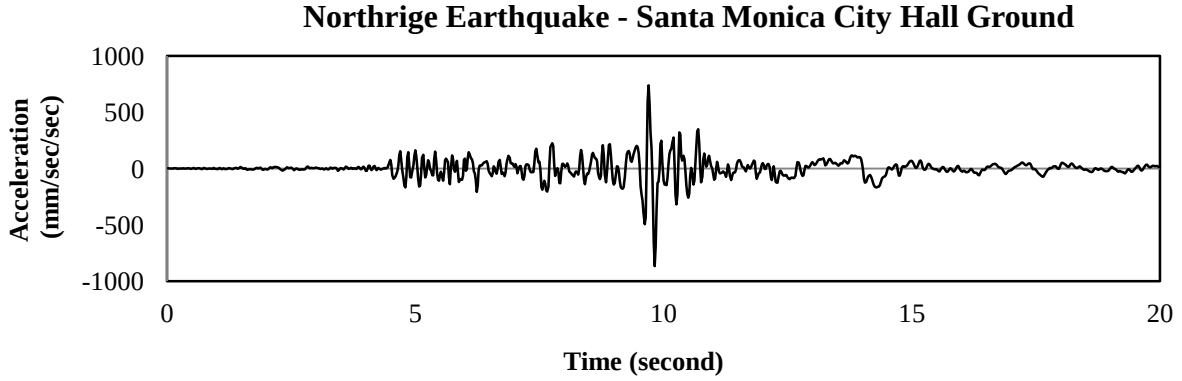

Figure 3.B -2 Earthquake ground motion record

For deformation constraints, it is assumed that the allowable plastic rotation of steel members is 0.015 radians, and the allowable inter-storey drift is 2.5% of story height (i.e., lateral deflection of the portal frame should not be greater than 3.9 in (99mm). Each of the two sectional variables is selected from among a given group of compact sections (Table 3.B-1). The design optimization problem is written as

$$\text{Minimize:} \quad \text{Weight} = \sum_{i=1}^{3} \rho \cdot A_i \cdot L_i \tag{3.B - 2}$$

$$\text{Subject to:} \quad \varphi_{max,i} \leq 0.015 \quad (i = 1,2,3) \tag{3.B - 3}$$

$$\delta \leq 99 \text{ mm} \tag{3.B - 4}$$

where: A_i is the cross sectional area for member i; L_i is the length of member i; and ρ is the material mass density of structural steel.

Table 3.B-1 Candidate sections for sizing variables x_1, x_2

Index	Bitstring	x_1(column)	x_2(beam)
1	0000	W14x68	W18x106
2	0001	W14x61	W18x97
3	0010	W14x53	W18x86
4	0011	W14x48	W18x76
5	0100	W14x43	W18x71
6	0101	W14x38	W18x65
7	0110	W14x34	W18x60
8	0111	W14x30	W18x55
9	1000	W12x72	W16x100
10	1001	W12x58	W16x89
11	1010	W12x53	W16x77
12	1011	W12x50	W16x67
13	1100	W12x45	W16x57
14	1101	W12x40	W16x50
15	1110	W12x35	W16x45
16	1111	W12x30	W16x40

Bitstring: decode value of the size variables

Nonlinear time history analysis programmed in the OpenSees software (OpenSees 2008) is employed to evaluate every candidate design. The steel material is modelled by a bilinear elastoplastic stress-strain relationship with a 5% strain hardening. Frame members are modelled using the force-based beam-column element with five Gauss-Labatto numerical integration points. The lumped mass points are located at the beam-column joints of the frame. The mass value at each joint is equal to half of the total mass. Newmark method of direct integration with the assumption of constant average acceleration within a time interval is employed to construct the system equations during iterations. The nonlinear equations during each time interval are solved through Newton-Raphson numerical method. The Rayleigh damping matrix is determined using the proportionality constants computed using the frequencies of modes 1 and 2 with damping ratios of 0.05.

A Genetic Algorithm (implemented with the software of MATLAB) is applied to find the optimal design. Since each design has 16 candidate sections, it is encoded with 4 bits (i.e., 2^4=16 sections). Each candidate design solution (i.e., a random combination of a column section and a beam section) is represented by an 8-bit digit of chromosome. The first generation with a specific

population size is randomly generated. The violation of a constraint will cause the design objective (i.e., 'weight' in this design problem) to be penalized. The population is improved through the operations of crossover and mutation until the convergence criterion is reached. The major parameters to control the GA are selected as follows,

- **Population Size:** The parameter controls how many individual designs there are in each generation. To investigate the effect of 'Population Size', a parameter study on various values of 'Population Size' has been carried out from 10 to 35.
- **Crossover Rate:** Crossover is an operation in which the genetic algorithm combines two individuals, or parents, to produce an offspring. The crossover rate is taken to be 1 in this problem.
- **Mutation Rate:** To provide genetic diversity, a mutation rate is set to make small random changes in individuals to create mutation children. The mutation rate is set to be 0.05 in this problem.

Design Results

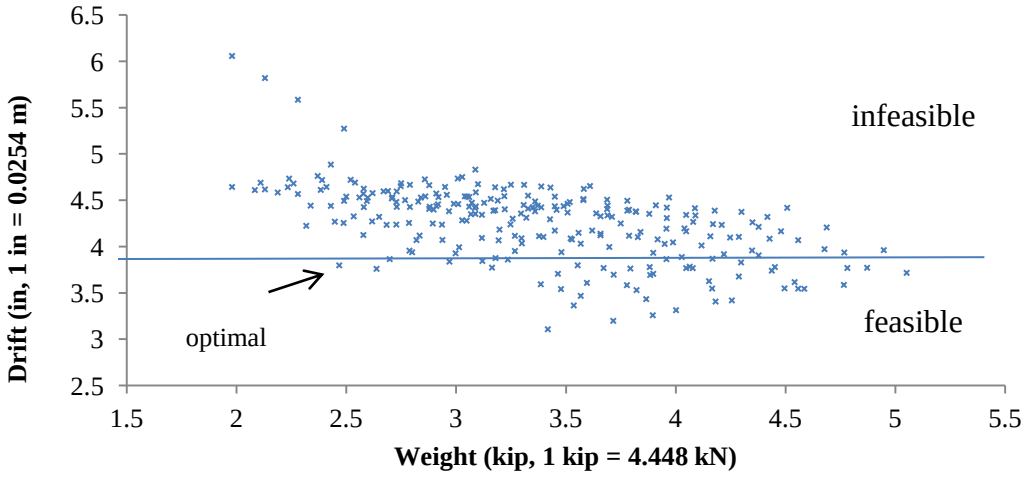

Figure 3.B -3 Distribution of designs in objective - constraint space

It is found that all the candidate solutions satisfy the plastic rotation constraints on the columns and the beam. The 256 design solutions are represented in the structural weight versus inter-storey drift space, as shown in Figure 3.B-3. The drift constraint divides the design space into

feasible and infeasible subspaces. The optimal solution (i.e., the design with W14x43 beam and W16x45 columns) is identified to be located at the far left of the feasible region (the weight is 2.468 kips (10.978 kN)) .

The results of 5 runs for each ‘population size’, total 30 runs, are shown in Table 3.B-2. It is observed that the Genetic Algorithm is not guaranteed to obtain the minimum weight design when only one run is implemented. Although each population size option leads to the optimal design within 5 runs, it appears that the population size 30 (wherein 4 out of 5 runs obtain the optimal design) is more effective for this design problem.

As illustrated in Figure 3.B-3, a specific inter-story drift can correspond to a large number of design solutions. Generally, it is not easy to find the optimal solution through a trial-and-error procedure.

Table 3.B-2 Results of GA runs

pop=10	bitstring	x_1	x_2	Weight (kip)	δ (in)	φ (rad.)
Run1	01001110	W14x43	W16x45	2.468	3.80	0.0128
Run2	01101001	W14x34	W16x89	3.554	3.80	0.0141
Run3	00000101	W14x68	W18x65	3.718	3.70	0.0126
Run4	11000110	W12x45	W18x60	2.970	3.84	0.0129
Run5	11000110	W12x45	W18x60	2.970	3.84	0.0129

pop=15	bitstring	x_1	x_2	Weight (kip)	δ (in)	φ (rad.)
Run1	00010111	W14x61	W18x55	3.236	3.86	0.0131
Run2	01010111	W14x38	W18x55	2.638	3.76	0.0137
Run3	11001011	W12x45	W16x67	3.180	3.88	0.0130
Run4	01001110	W14x43	W16x45	2.468	3.80	0.0128
Run5	01011100	W14x38	W16x57	2.698	3.87	0.0141

pop=20	bitstring	x_1	x_2	Weight (kip)	δ (in)	φ (rad.)
Run1	01001110	W14x43	W16x45	2.468	3.80	0.0128
Run2	01100011	W14x34	W18x76	3.164	3.77	0.0140
Run3	01100011	W14x34	W18x76	3.164	3.77	0.0140
Run4	11001011	W12x45	W16x67	3.180	3.88	0.0130
Run5	01010111	W14x38	W18x55	2.638	3.76	0.0137

pop=25	bitstring	x_1	x_2	Weight (kip)	δ (in)	φ (rad.)
Run1	01001110	W14x43	W16x45	2.468	3.80	0.0128
Run2	01010111	W14x38	W18x55	2.638	3.76	0.0137
Run3	01001110	W14x43	W16x45	2.468	3.80	0.0128
Run4	01010111	W14x38	W18x55	2.638	3.76	0.0137
Run5	00010111	W14x61	W18x55	3.236	3.86	0.0131

pop=30	bitstring	x_1	x_2	Weight (kip)	δ (in)	φ (rad.)
Run1	01010111	W14x38	W18x55	2.638	3.76	0.0137
Run2	01001110	W14x43	W16x45	2.468	3.80	0.0128
Run3	01001110	W14x43	W16x45	2.468	3.80	0.0128
Run4	01001110	W14x43	W16x45	2.468	3.80	0.0128
Run5	01001110	W14x43	W16x45	2.468	3.80	0.0128

pop=35	bitstring	x_1	x_2	Weight (kip)	δ (in)	φ (rad.)
Run1	01001110	W14x43	W16x45	2.468	3.80	0.0128
Run2	11000101	W12x45	W18x65	3.120	3.84	0.0129
Run3	01010111	W14x38	W18x55	2.638	3.76	0.0137
Run4	01010111	W14x38	W18x55	2.638	3.76	0.0137
Run5	01001110	W14x43	W16x45	2.468	3.80	0.0128

1 kip = 4.448 kN, 1 in = 0.0254 m

Appendix 4.A

Selected Ground Motion Time-Histories

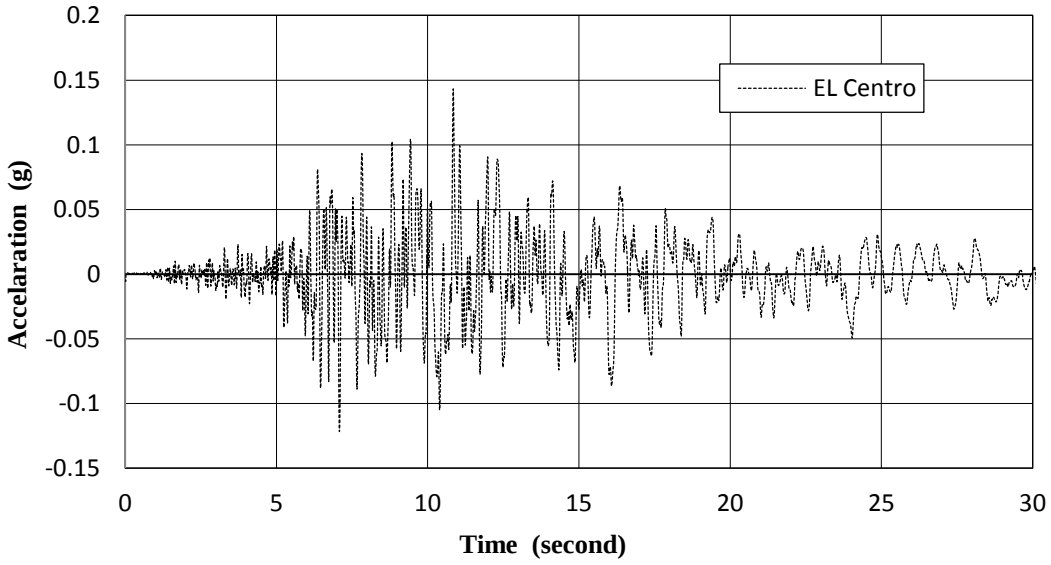

Figure 4.A-1 Ground motion record (1979 Imperial Valley: El Centro Array #12)

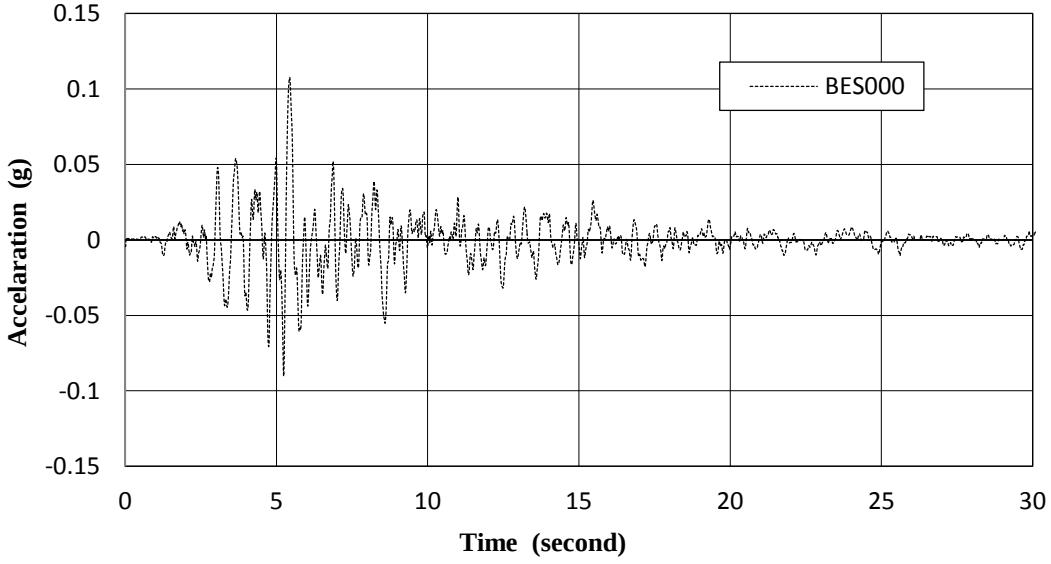

Figure 4.A-2 Ground motion record (1989 Loma Prieta: Belmont Envirotech)

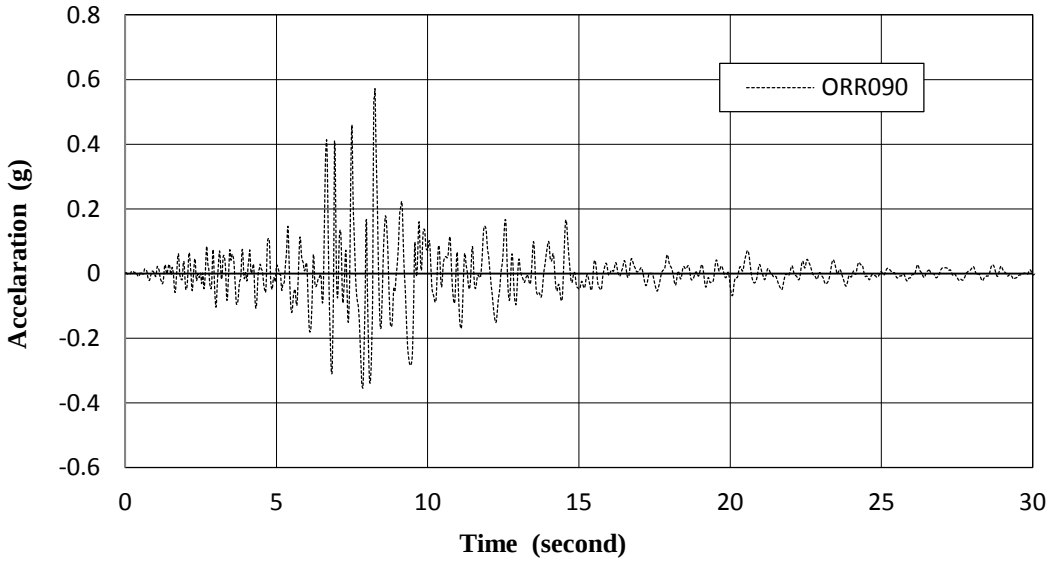

Figure 4.A-3 Ground motion record (1994 Northridge: Old Ridge RT 090)

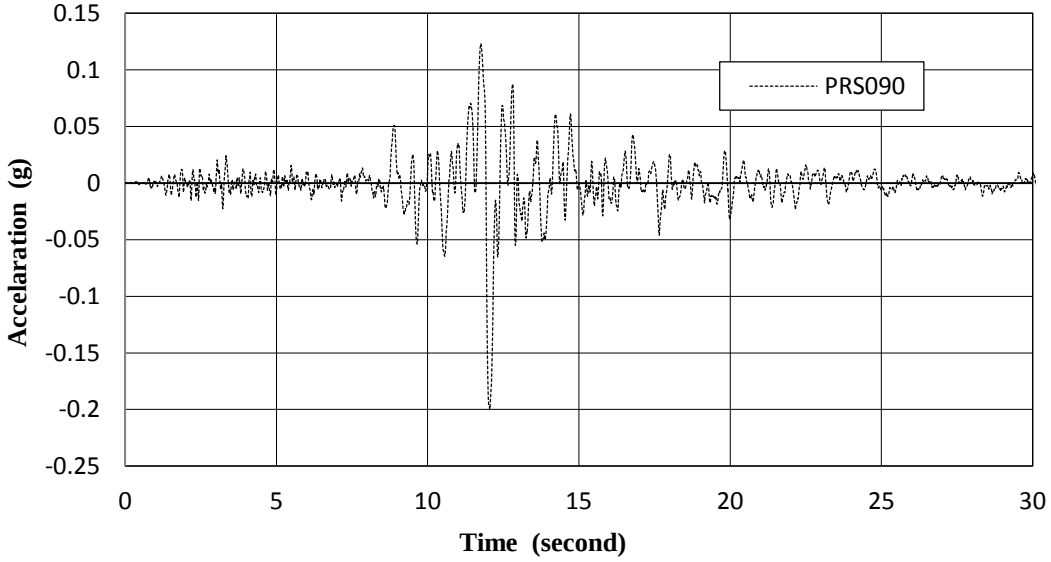

Figure 4.A-4 Ground motion record (1989 Loma Prieta: Presidio)